Direct profiling of III/V semiconductor nanostructures at the atomic level by cross-sectional scanning tunneling microscopy

Please check the document version of this publication:

• A submitted manuscript is the version of the article upon submission and before peer-review. There can be important differences between the submitted version and the official published version of record. People interested in the research are advised to contact the author for the final version of the publication, or visit the DOI to the publisher's website.
• The final author version and the galley proof are versions of the publication after peer review.
• The final published version features the final layout of the paper including the volume, issue and page numbers.

[Link to publication](#)

Direct profiling of III/V semiconductor nanostructures at
the atomic level
by cross-sectional Scanning Tunneling Microscopy

PROEFSCHRIFT

ter verkrijging van de graad van doctor aan de
Technische Universiteit Eindhoven, op gezag van de
Rector Magnificus, prof.dr. R.A. van Santen, voor een
commissie aangewezen door het College voor
Promoties in het openbaar te verdedigen
op donderdag 27 februari 2003 om 16.00 uur

door

Dominique Maria Bruls

Geboren te Sittard

Dit proefschrift is goedgekeurd door de promotoren:

prof.dr. J.H. Wolter
en
prof.dr. M.S. Skolnick

Copromotor:
dr. P.M. Koenraad

voor Karin

Contents

Chapter 1

Introduction

1.1   Beyond the human eye

Although "vision" is considered by many people to be the most important sense, even the human eye has its physical limits as objects smaller than 70 micron [1] cannot be distinguished. Man developed aids like microscopes and telescopes to enhance this sense. As human curiosity went further and further it eventually ran into the physical limitations of optical imaging, like the diffraction limit of light. The resolution could only be pushed further by reducing the wavelength of the photons or by using other "probing" particles like electrons. Although electrons instead of light can be used in Scanning Electron Microscopy (SEM) to "see" atoms at extremely high resolution [2], still certain limitations remained as, for instance, it is still very difficult to make a clear distinction between different elements.
In 1981 Binnig and Rohrer from the IBM research-laboratory Zürich, Switzerland, invented the Scanning Tunneling Microscope (STM). This technique uses a completely different principle to image a surface as it is based on vacuum tunneling of electrons. By using this quantum phenomenon it is possible to make a scan of the topography of the surface, rather than making an "image" or "photo". In the STM "images" (the word "image" is used for convenience, although we discuss computer generated topography maps in which the height differences are represented by different colors or intensity) not only individual atoms can be distinguished, but one also can discriminate their chemical nature. In the last 20 years this technique has evolved from a curiosity to a standard research-lab technique.

1.2   Semiconductor growth: Reduced dimensionality

In traditional semiconductor devices, like lasers and transistors, bulk materials have been used. However, modern semiconductor heterostructure devices, used in contemporary and future micro- and opto-electronics, consist of stacks of layers of different semiconductor materials, each with specific electronic and optic properties. These layered structures are grown by epitaxial techniques such as Molecular Beam Epitaxy (MBE), Chemical Beam Epitaxy (CBE) or Metal Organic Chemical Vapor Deposition (MOCVD). In the Semiconductor Physics Research group at the University of Technology Eindhoven, MBE and CBE are used to grow III-V semiconductor nanostructures. These growth facilities are used to fabricate structures and devices needed not only for novel opto-electronic devices, but also for nanostructures in which the fundamental properties of solid state matter, like transport of charge (electrons, holes), excitons, photons or lattice vibrations (phonons) can be investigated.

Most semiconductor devices, like a quantum well diode laser, consist of well-defined epitaxial layers with atomically flat interfaces that spatially confine charge carriers in one direction. This confinement causes unique properties for these charge carriers. Quantum dots are heterostructures in which charge carriers are spatially confined in all three dimensions, see Fig.1.1. The "atomic-like" (discrete) electronic spectrum of such a quantum dot makes it possible to eliminate several problems of contemporary electronics and photonics, such as the high injection current of semiconductor lasers and the degradation of device properties with increase of working temperature. The latter is caused by the "smearing" of charge carriers over an energy window in the order of k_BT. Furthermore novel device applications are possible.

| bulk | quantum well | quantum wire | quantum dot |
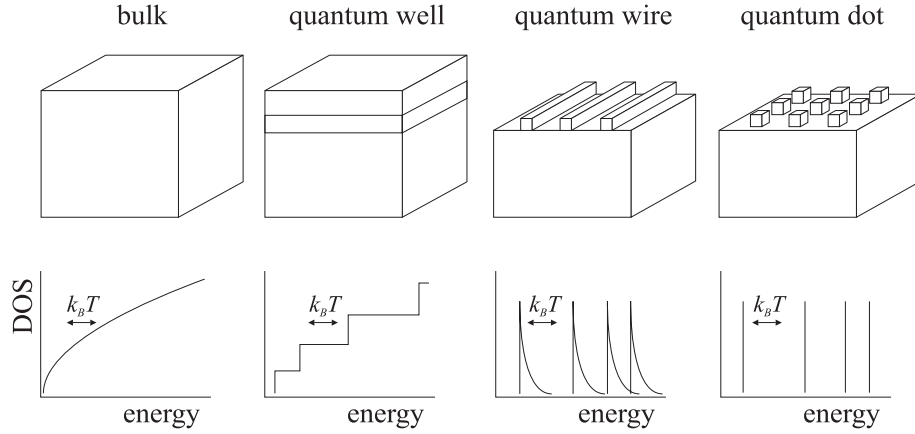
Fig. 1.1: *Density of states (DOS) of semiconductor structures in which charge carriers are not confined (bulk), or are confined in one (quantum well), two (quantum wire) and three dimensions (quantum dot). The arrow in the DOS graph indicates the width of the energy window over which the charge carriers will be smeared at a certain temperature.*

When charge carriers are confined in only one direction, like in a 2-D system, they can occupy a continuous range of electronic states due to their kinetic energy. Consequently there is a range of possible transitions. If charge carriers are confined in all 3 directions, we obtain an electronically 0-D system, although the physical shape of this quantum dot is of course a 3-D object. In quantum dots, only discrete electron energy states are allowed. Provided that the dots are small enough and that the level separation is larger than k_BT, there can be no broadening of an optical transition. For the quantum dot diode laser, this would mean: a lower threshold current, a narrower emission line width and a higher temperature tolerance. Fig.1.2 shows the performance of different diode lasers, including quantum dot lasers. It is the goal to obtain structures with high dot densities and high dot uniformity, leading to even lower threshold currents, a higher power output and improved emission-wavelength stability.

In the last decade several growth techniques have been used to fabricate quantum dots. It is possible to fabricate quantum dots by, for instance, annealing of strained semiconductor heterostructures, but the most preferred method uses the self-organizing effect of semiconductor nanostructures in hetero-epitaxial semiconductor systems. In the so-called

Stranski-Krastanov growth mode, the lattice mismatch between the used semiconducting materials causes nano-scale islands to be formed. In such structures the unique physical properties of quantum dots, which had already been predicted for many years, were demonstrated for the first time.
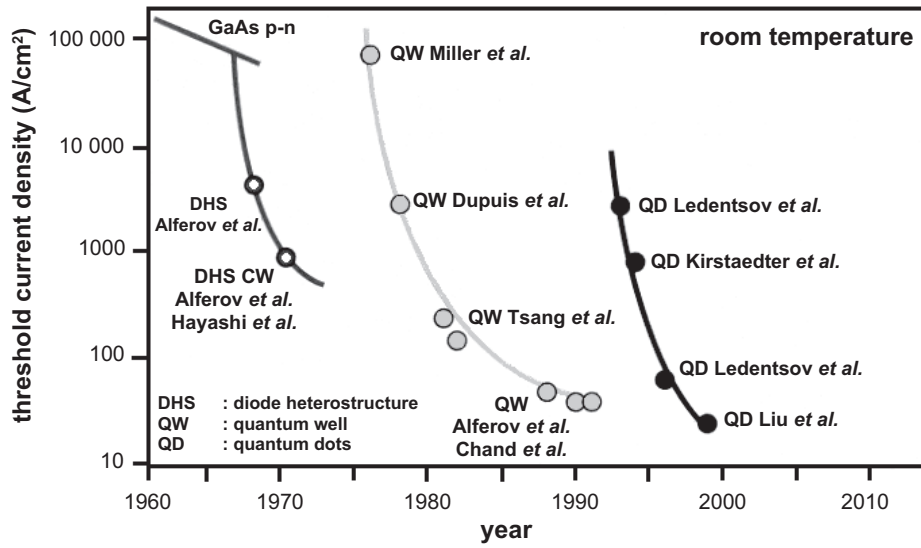
Fig.1.2: *The narrow gain profile in quantum dot devices results in a lower threshold current density [3]*

1.3 Why STM?

Although some commercial quantum dot lasers are already available, still little is known about the fundamental properties of individual dots. Numerous calculations on the electronic structure of quantum dots have been performed [4-7], but in the absence of good structural information of real dots, idealized shapes (usually pyramidal) have been used. Fry *et al*. [8] recently derived indirectly from photocurrent experiments the shape and composition of InAs quantum dots in a GaAs matrix. These experiments unexpectedly showed that the quantum dots posses a permanent inverted dipole, because the holes are localized towards the top of the dot, above the electrons. Modeling of this result suggested that the quantum dots have the shape of a truncated pyramid and also that they contain significant concentrations of gallium rather than consisting of pure InAs. Moreover they found that it is essential to have a graded composition profile with indium aggregation at the top surface of the dot. However, the fits used in these experiments are not unique [9]. By using different (perhaps unphysical) indium concentration profiles and shapes, good fits might be achieved as well, so more direct proof would be needed to unambiguously verify the findings of [8].

By using STM, a more direct proof of the shape and composition of quantum dots and knowledge of their structural and electronic properties in general are obtained for the first time. By STM, atomically resolved images of a surface can be obtained, while making a distinction between the dot material and the surrounding matrix. First, however, several other questions have to be answered, like what do we really see in STM images, how can chemical contrast in STM images be understood and concentration profiles in heterostructures be determined.

In our group we use STM to investigate cleaved semiconducting structures. The samples under investigation have to be cleaved in order to expose cross-sectional planes through the semiconducting structures of interest, such as quantum wells, quantum dots and doped layers. This mode of STM is called cross-sectional Scanning Tunneling Microscopy (X-STM).

1.4   Scope of this thesis

It is the goal of this thesis to contribute to a better insight in the shape, size, electronic properties and composition of quantum dots or stacks of quantum dots. Therefore, first the tunnel process itself and the way epitaxial grown strained heterostructures behave upon cleavage have to be discussed. In chapter 2 we first discuss the sample growth, engineering of semiconducting structures and the electronic properties of strained structures. In chapter 3 we treat the tunnel process, which is the principle upon which STM is based. Also the possibility of imaging the wavefunction in for instance a quantum dot is discussed, as well as the influence of tip-induced band bending. Furthermore, the buckling of III/V semiconductor surfaces and the properties of cleaved surfaces are discussed.

In chapter 4 the experimental procedures are explained. A brief description of the STM scanner itself, the ultrahigh vacuum setup and the procedures involved in tip and sample preparation will be given.

In order to understand the relaxation of 3D structures, like quantum dots, we first investigate the 2D quantum well, which has a simpler relaxation behavior. In chapter 5, the relaxation of strained 2D structures (quantum wells) is discussed. In STM images, two contributions to the measured topography of a surface are present, namely the real topography and topography due to electronic contrast between different semiconducting layers/materials. We show that by choosing the proper tunnel conditions, it is possible to suppress the electronic contrast, thus obtaining the real topography of the sample surface. It is then possible to determine the real outward relaxation of strained layers upon cleavage, enabling us to determine the concentration profiles in these strained layers. We apply this analysis to various III/V semiconductor structures.

Because of their application as 1.3-1.55 μm laser diodes, nitrogen diluted InGaAsN alloys lattice matched to standard semiconductor substrates, received considerable attention recently [10]. In chapter 6, InP/InGaAsN/InP quantum well structures are discussed. We show the nitrogen incorporation profile and that lateral diffusion during annealing leads to the formation of nitrogen rich quantum dots. The latter was already predicted from previous optical measurements on similar structures.

In chapter 7, which can be considered to be the main topic of this thesis, we discuss the determination of shape, size, and composition of self–assembled InAs quantum dots within a GaAs matrix. We employ the knowledge obtained from the measurements and analysis of

the quantum wells to suppress the electronic contrast in the quantum dot measurements. Numerical calculations are used to proof unambiguously that the models used by Fry *et al*. [8] and Barker and O'Reilly [11] are correct. We also show that we can image confined electronic states. These results are compared with theoretical calculations. Furthermore, the influence of the deposition speed during the growth of quantum dots on the final shape, size and composition of the quantum dots and the influence of the amount of dot-material deposited are discussed. Finally the formation of the wetting layer during dot growth is investigated. In chapter 8 stacking of dots, strain induced dot formation and growth rate changes during the formation of quantum dot stacks are discussed.

References

[1]   http://www.madsci.org/posts/archives/may97/864446241.Ph.r.html

[2]   P.E. Batson, N. Dellby and O.L. Krivanek, Nature **418,** 617 (August 2002)

[3]   M. Hatcher, Opto and Lasers Europe, p.33 (2000)

[4]   M. Grundmann, O. Stier, D. Bimberg, Phys. Rev. B **52** (16), 11969 (1995)

[5]   M. Cusack, P.R. Briddon, M. Jaros, Phys. Rev. B **54** (14), 2300 (1996)

[6]   C. Pryor, Phys. Rev. B **57** (12), 7190 (1998)

[7]   J. Kim, L.-W. Wang, A. Zunger, Phys. Rev. B **57** (16), 9408 (1998)

[8]   P.W. Fry *et al.*, Phys. Rev. Lett. **84** (4), 733 (2000)

[9]   W. Sheng and J.P. Leburton, Phys. Rev. B **63**, 161301(R) (2001)

[10]   M. Kondow *et al.*, Jpn. J. Appl. Phys. Part 1, **35**, 1273 (1996)
           W. Li *et al.*, Appl . Phys. Lett. **78** (19) (2001)
           Y. Arakawa, T. Someya and K. Tachibana, Phys. Stat. Sol. (b) **244**,
           No. 1,1-11 (2001)
           A.M. Mintairov *et al.*, Phys. Rev. Lett. **87** (27) (2001)

[11]   J.A. Barker and E.P. O'Reilly, Phys. Rev. B **61** (20), 13840 (2000)

Chapter 2

Growth of Semiconductor Structures

2.1   Introduction

The importance of and demand for opto-electronic semiconductor devices, as used in for instance telecommunication networks, computer processors, mobile phones and other consumer products still grows. Therefore, also the demands that are put on the semiconductor materials and their complexity still increase. The materials needed for novel applications are in general of higher purity, consist of multiple layers of which some may contain nanostructures and have a carefully engineered band structure, thus increasing the importance of high-tech state-of-the-art fabrication methods.

2.2   Growth techniques

2.2.1   Introduction

During semiconductor growth, one ordered mono-crystalline material, the epitaxial layer, is grown on top of another, the substrate. In this way a structure containing layers of different materials can be grown layer by layer. These layers can have a different lattice constant, but if the differences in lattice constants are small enough, the layers will adapt their lattice constants in such a way that their crystallographic structure will fit to each other. This will introduce strain, which alters the electro-optical properties of these layers, or may lead to the spontaneous formation of nanostructures if the strain inside the layers exceeds a certain level. It is also possible to apply lateral structuring to epitaxial grown structures and selective area epitaxy, resulting in an even higher functionality of the structures and devices [1].

2.2.2 Molecular Beam Epitaxy

Molecular Beam Epitaxy (MBE) [2] is a common technique for growing epitaxial semiconductor structures. In MBE a substrate surface is maintained at an elevated temperature in ultrahigh vacuum. On top of this substrate, thin films that originate from thermal-energy reactions between atomic or molecular beams and the substrate surface, crystallize. In MBE the reactants for the epitaxial layers are generated by thermal evaporation from solid sources inside an ultrahigh vacuum (UHV) growth chamber. By

selecting the proper temperature of the effusion cell, the vapor pressure and thus the material flux towards the heated substrate is controlled. Due to the low pressure during growth, collision free transport in molecular or atomic beams from effusion cell to the substrate is possible. This allows for very fast switching of the beam, by means of shutters, which enables the growth of heterostructures with atomically sharp interfaces. In comparison to most other epitaxial techniques, the main advantage of MBE is that the growth is performed under ultrahigh vacuum conditions. Therefore *in situ* surface diagnostic methods such as Reflection High Energy Electron Diffraction (RHEED), Auger Electron Spectroscopy (AES), ellipsometry and many other techniques can be employed [2, Chapter 4]. By using these analysis and control methods the fabrication of sophisticated structures is possible, as the growth of these structures can be controlled down to the atomic level.

2.2.3 Chemical Beam Epitaxy

Chemical Beam Epitaxy (CBE) is a relatively new development in epitaxial technology. It can be considered as a modified MBE machine where all the solid sources are replaced by a gas delivery system, as used in Metal Organic Vapour Phase Epitaxy (MOVPE) [3,4]. The advantage of CBE is that the beam nature of CBE ensures that all reactions are heterogeneous. This means that they only occur in the high temperature cracker and on the sample surface. Together with the very fast gas flow response, this makes it possible to grow atomically abrupt interfaces and use *in situ* analysis techniques, like in MBE. In CBE the substrate temperatures can be rather low, which is beneficial for the growth of highly strained structures and the quality of multiple step epitaxy. Also the uniformity of the grown samples is very good. CBE has distinct advantages compared to MBE and MOVPE with respect to monolithic integration of devices and the planar selective growth of waveguide ridges or low-dimensional structures like quantum wires. In conclusion, CBE has some very attractive features regarding efficiency, environmental issues, versatility, reproducibility, uniformity and selective area epitaxy [1,5].

2.3   Semiconductor engineering

The specific electronic properties of quantum dots make them interesting and promising nanostructures, both from a fundamental and from a device point of view. Due to the difference in bandgap between the quantum dot material and the surrounding material and the band line-up, charge carriers are confined. Confinement of charge carriers in all three dimensions, as is the case in quantum dots, causes a δ-function-like energy dependence of the density of states. In order to have confinement in all three dimensions, the dimensions of the quantum box have to be in the order of the *de Broglie* wavelength of electrons (50 nm in GaAs). One of the most promising ways of obtaining 3D structures with such small dimensions is the Stranski-Krastanov (SK) growth mode [6-8]. Compound semiconductors that are made from group III and V elements from the periodic table, the so-called III-V semiconductors, are very useful for the fabrication of these structures, as a wide range of bandgaps is available, see Fig. 2.1.
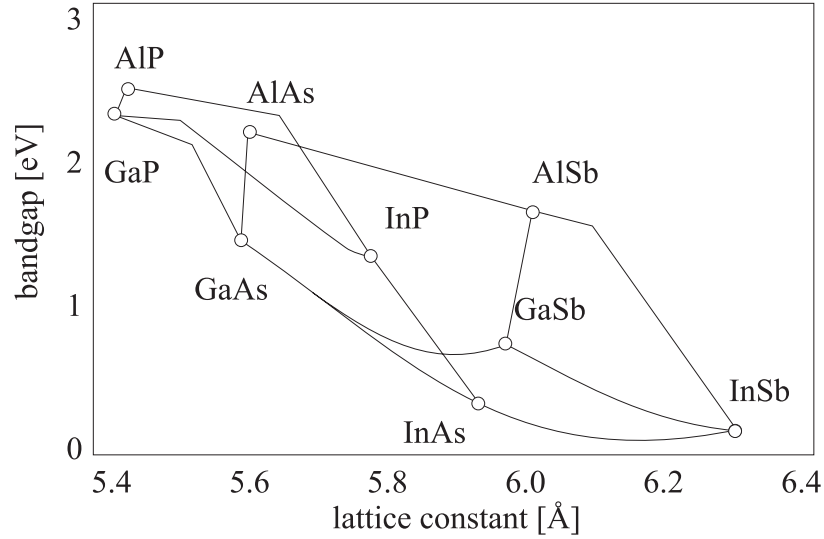
Fig. 2.1: *Bandgap and lattice constant of frequently used III-V semiconductors*
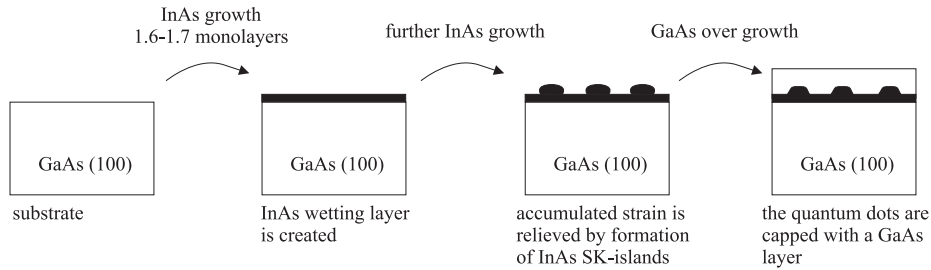
Fig. 2.2: *Stranski-Krastanov growth of quantum dots*

Quantum wells and superlattices are examples of one-dimensional heterostructures that are made by normal, lattice matched, epitaxial growth. Materials with different bandgap (E_g) are combined to give the desired band structure. This is easiest with materials with a similar lattice constant like GaAs and AlAs, see Fig. 2.1. When heterostructures are made of materials with different lattice constants, these are called lattice-mismatched or so-called pseudo-morphic structures. Growth of lattice-mismatched layers is only possible up to a critical thickness after which a transition from 2D to 3D growth mode occurs. An example of such growth mode occurs for InAs grown on GaAs (001), which has a large lattice-mismatch of 7%. The critical mean thickness for such a strained layer is 1.6-1.7 monolayers. After epitaxial growth of an InAs layer of this thickness, the so-called wetting layer, the strain that accumulates after further growth is relieved by the formation of nanometer-scale InAs islands on top of this wetting layer, see Fig. 2.2. This 3D growth mode is called Stranski-Krastanov growth. These InAs islands can be overgrown with GaAs to create InAs quantum dots embedded in a GaAs matrix. The structures are of high crystalline perfection and have a high size homogeneity (10%) [6,9]. Fig. 2.3 shows a top

view Atomic Force Microscopy (AFM) image of an ensemble of SK-grown islands, before burying under the capping layer.
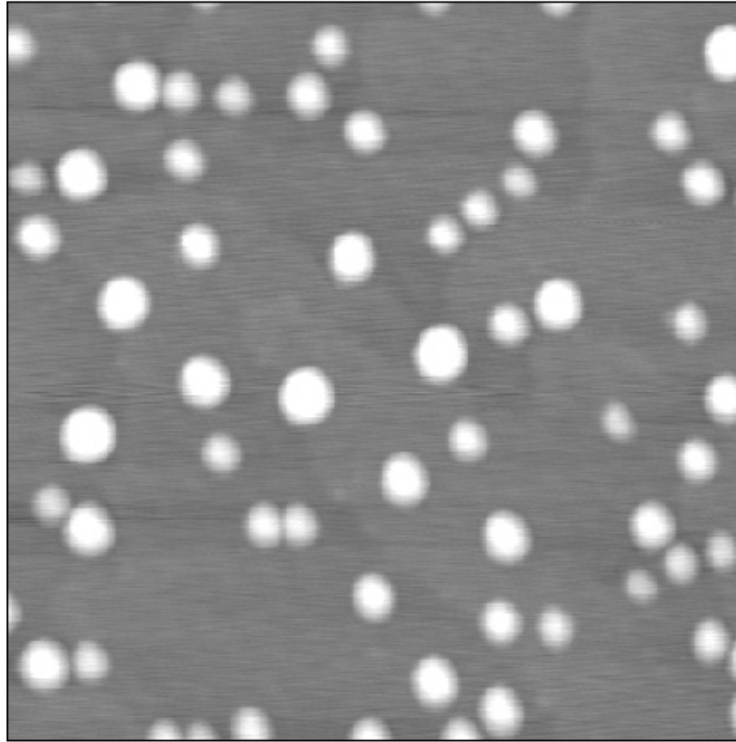
Fig. 2.3: *AFM image of InAs SK-grown islands on GaAs grown by MBE at 480°C. The amount of InAs deposited was 2.1 monolayers at a deposition rate of 0.014 monolayer/s. Image size 500x500 nm², z-scale = 10 nm [10]*

2.4   Electronic properties of strained structures

Quantum mechanics describe the confinement of electrons and holes in a potential well. In a semiconductor structure, this potential is determined by its band structure. Electrons are confined in the conduction band potential and holes in the valence band potential. The confinement energies inside quantum dots depend, besides on the shape and dimensions of the dot, on the height of the potential barriers. The barrier height for electrons and holes in the dot is determined by the difference in bandgap between the dot- and matrix material and the band line-up. The bandgap and band offset depend on the composition of the dot material.
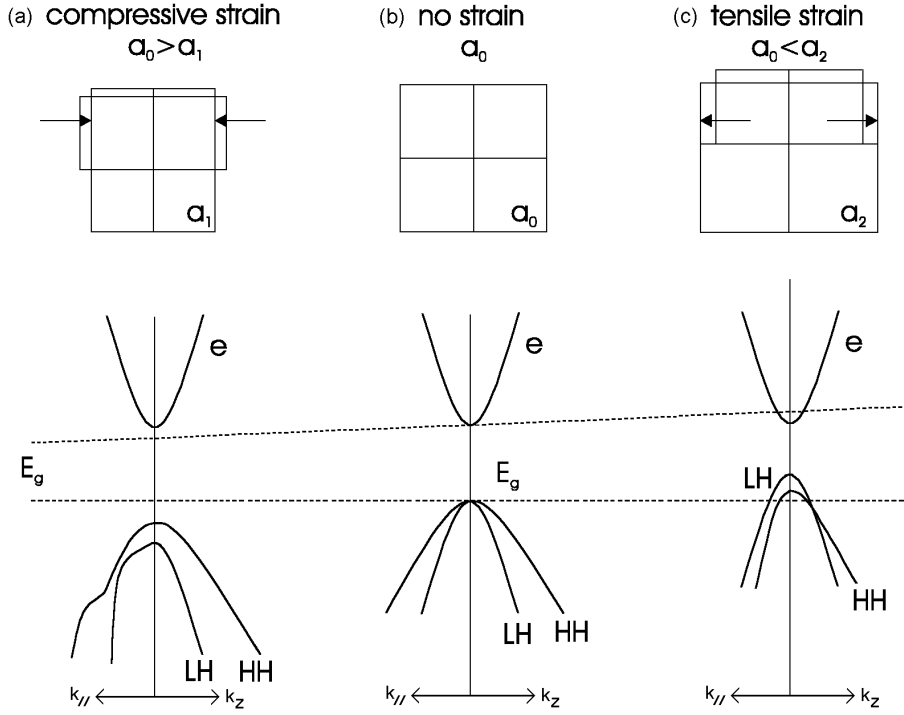
Fig. 2.4: *The energy-band structure in momentum space of typical III/V materials under (a) biaxial compression, (b) lattice matched conditions, and (c) biaxial tension for different heterostructures. The dashed lines indicate the bandgap change with composition for the unstrained material. Due to the strain, however, the spectral positions of the conduction and valence bands shift, thus changing the bandgap additionally. Compressive strain increases and tensile decreases the bandgap of the heterostructure material [11]. The relative positions of the heavy-hole and light-hole bands with respect to each other are influenced by strain as well.*

The band structure is influenced by the internal strain distribution in the material, see Fig. 2.4. Due to the large lattice-mismatch, necessary for SK-growth, there will be a significant change in the band structure of the quantum dots. Strain can be separated in hydrostatic and shear components. The hydrostatic strain ε_h is linked to volume changes in the material and influences the bandgap. Compressive strain enlarges the bandgap and tensile strain decreases the bandgap, with respect to the value that would be expected from the composition of the material (Fig. 2.1).

References

[1]   C. Verschuren, *Selective Area Chemical Beam Epitaxy of (Ga,In)(As,P) structures*, Thesis, University of Technology Eindhoven, The Netherlands (1999), ISBN 90-386-0917-5

[2]   M.A. Hermanand H. Sitter, *Molecular Beam Epitaxy, Fundamentals and Current Status*, 2nd Edition Springer-Verlag Berlin Heidelberg (1996)

[3]   W.T. Tsang and .H. Chiu, in: *CBE and related techniques*, Ed. J.S. Foord, G.J.Davies and W.T. Tsang (John Wiley, New York, 1997) 135

[4]   F. Alexandre and J.L. Benchimol in: *CBE and related techniques*, Ed. J.S. Foord, G.J.Davies and W.T. Tsang (John Wiley, New York,1997) 31

[5]   E. Veuhoff, J. Cryst. Growth **195** (1998) 444

[6]   D. Leonard *et al*., Appl. Phys Lett. **63** (23), 3203 (1993)

[7]   N. Kirstaedter *et al*., Appl. Phys. Lett. **69** (9), 1226 (1996)

[8]   D. Bimberg *et al*., Phys. Status Solidi B **194**, 159 (1996)

[9]   M. Colocci *et al*., Appl. Phys. Lett. **70** (23), 3140 (1997)

[10]   AFM image provided by T.M. Mano, University of Technology Eindhoven, The Netherlands

[11]   S.L. Chuang, Phys. Rev. B **43** (12), 9649 (1991)

Chapter 3

Theory

3.1 Introduction

A Scanning Tunneling Microscope is able of making atomically resolved images of surfaces of electrically (semi-) conducting samples. For that purpose, a sharp metal tip is brought within 1 nm of the surface. When a voltage is applied between tip and sample, electrons can tunnel between the tip and the sample and an electric current will flow. This current depends exponentially on the distance between tip and sample. If this current is kept constant, by regulating the distance between the tip and the sample while the tip is scanned laterally, adjacent profiles of the surface topography can be assembled into an image via a computer, thus showing the topography of the scanned surface. However, except from the width of the tunnel barrier, this tunnel current also depends on the electronic properties of the sample. Thus the resultant image contains also electronic contrast besides topographic information. This means that for a correct interpretation of STM images a good understanding of the tunnel process is essential. In order to get a better understanding of what is actually imaged during STM, the tunnel process and the influence of tip-states are discussed. We demonstrate that the local density of states (LDOS) of the sample can be imaged and that the influence of the tip-state can be neglected in most of the cases. For a complete and elaborate description of the tunnel processes involved in STM, see [1].

When tunneling on semiconductor surfaces, the conduction and valance band can bend up and down as function of applied tunnel voltage. This electrostatic tip-induced band bending may influence the appearance of atomically resolved lattices and can cause an erratic determination of the semiconductor bandgap during spectroscopic measurements. Therefore, band bending has to be discussed as well.

When heterostructures like quantum wells or quantum dots are "grown" the materials involved often have different lattice constants, leading to strain. When strained samples are cleaved the surface will relax. We discuss how we analyze the surface relaxation and how we obtain concentration profiles.

3.2 Principles of Scanning Tunneling Microscopy (STM)

3.2.1 The tunnel process

Electrons tunnel from occupied states in the tip (sample) to unoccupied states of the same energy in the sample (tip), see Fig. 3.1. Tunneling to unoccupied states in the semiconductor is called empty state tunneling and tunneling from occupied states in the sample is called filled state tunneling. The tunnel current depends on the overlap between

the tip and sample state. According to Fermi's Golden Rule [2], the tunnel probability of an electron in state χ in the tip to state Ψ in the sample is:

$$w = \frac{2\pi}{\hbar}\left|M\right|^2 \delta\left(E_\Psi - E\chi\right) \tag{3.1}$$

in which δ is the delta-function that accounts for the fact that only transitions can occur between states of the same energy. M is the tunnel matrix, indicating the overlap between the two electron wavefunctions of the sample χ and the tip Ψ at a separation surface in the gap, see Fig. 3.1a.

$$M = \frac{\hbar}{2m} \int\limits_{z=z_0} \left(\chi^* \frac{\partial \Psi}{\partial z} - \Psi^* \frac{\partial \chi}{\partial z} \right) dS \tag{3.2}$$

The matrix elements M are associated with different possible tip-states (see table 3.1)

Tip state	Matrix element
s	$\dfrac{2\pi C\hbar^2}{\kappa m_e} \Psi_s(r_0)$
p_x	$\dfrac{2\pi C\hbar^2}{\kappa m_e} \dfrac{\partial}{\partial x} \Psi_s(r_0)$
p_y	$\dfrac{2\pi C\hbar^2}{\kappa m_e} \dfrac{\partial}{\partial y} \Psi_s(r_0)$
p_z	$\dfrac{2\pi C\hbar^2}{\kappa m_e} \dfrac{\partial}{\partial z} \Psi_s(r_0)$
d_{zx}	$\dfrac{2\pi C\hbar^2}{\kappa m_e} \dfrac{\partial^2}{\partial z \partial x} \Psi_s(r_0)$
$d_{z^2-\frac{1}{3}r^2}$	$\dfrac{2\pi C\hbar^2}{\kappa m_e} \left(\dfrac{\partial^2}{\partial z^2} - \dfrac{\kappa^2}{3} \right) \Psi_s(r_0)$

Table 3.1: *All matrix elements are determined by the tip state. m_e is the electron mass, C a normalization constant, φ the work function and $\kappa=(2m_e\varphi)^{1/2}/\hbar$. Only for the last $d_{z^2-1/3r^2}$ – state the tunnel matrix element is dependent on the work function of the tip*
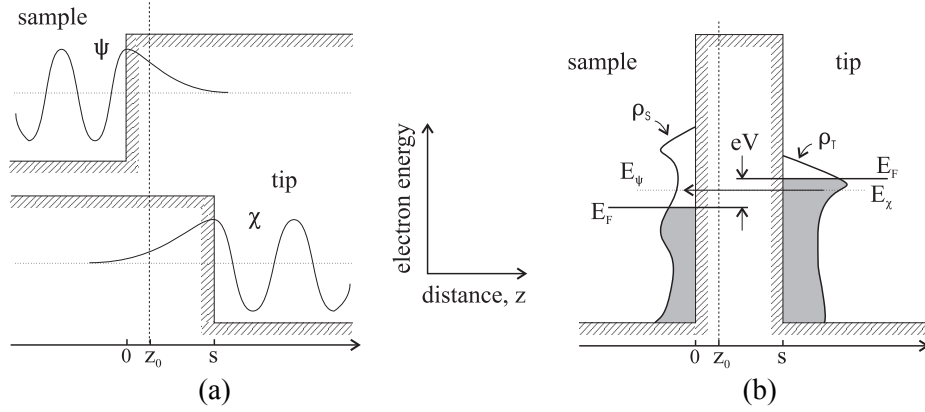
Fig. 3.1: *(a) Tip and sample wavefunctions penetrate the vacuum barrier. The overlap in the tunnel matrix M is calculated at surface z=z₀ in the vacuum barrier. (b) Schematic view of a tunnel junction with tip and sample density of states ρ_T , ρ_S. The relevant states are within an energy window of eV between the tip and sample Fermi energy (E_F)*

The tunnel current can be calculated by summing over all the relevant states. At finite temperatures, the electrons in both tip and sample follow the Fermi distribution. With a bias voltage *V*, the total tunnel current is

$$I = \frac{4\pi e}{\hbar} \int_{-\infty}^{\infty} \left[f(E_F - eV + \varepsilon) - f(E_F + \varepsilon) \right] \rho_S(E_F - eV + \varepsilon)\rho_T(E_F + \varepsilon)|M|^2 \, d\varepsilon \qquad (3.3)$$

where $f(E) = \{1 + \exp[(E-E_F)/k_BT]\}^{-1}$ is the Fermi distribution function describing the occupation of the electronic states around the Fermi energy E_F. $\rho_S(E)$ and $\rho_T(E)$ are the density of states (DOS) at the sample and tip respectively.

If k_BT is smaller than the energy resolution required in the measurement, then the Fermi energy distribution function can be approximated by a step function and the relevant states are within an energy window of *eV*, see Fig. 3.1b. The magnitude of the matrix element $|M|$ depends on the two wavefunctions involved and their overlap, as determined by the tip-sample distance and barrier height. In the constant current image mode, the tip-sample distance is kept approximately constant and $|M|$ does not change considerably in the interval of interest. Then the tunnel current is determined by the convolution of the DOS of the tip and sample according to the Bardeen Formula:

$$I \propto \int_{0}^{eV} \rho_S(E_F - eV + \varepsilon)\rho_T(E_F + \varepsilon)d\varepsilon \qquad (3.4)$$

When a very sharp tip is produced, there is only one atom protruding from the tip apex. From experimentally observed corrugation amplitudes it is deduced [2, p32-36] that the

tunnel current is predominantly determined by a *d*-type localized state on this atom, see Fig. 3.2b. Because the tip is a free-electron metal tip, it has a constant DOS energy dependence. Therefore, according to Eq. 3.4, a constant current STM image can be interpreted as an image of the density of states of the sample. The density of states of the semiconductor sample consists of bulk and localized states, see Fig. 3.2a. Localized states arise at the surface due to the broken symmetry.
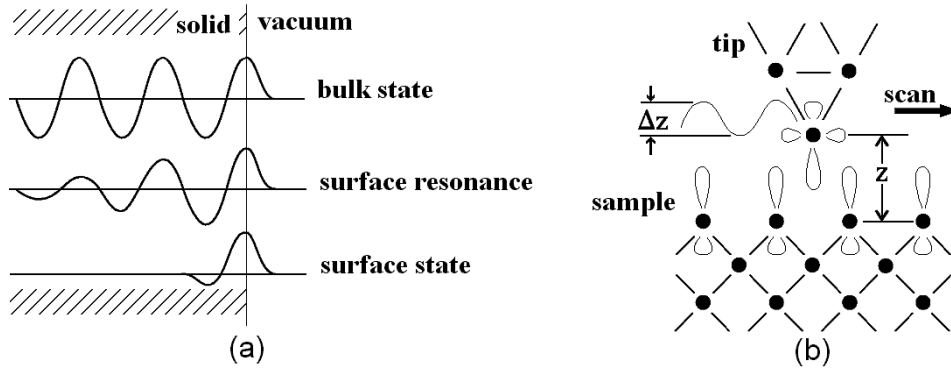
Fig. 3.2: *(a) Bulk state, surface resonance and surface state at the surface of a solid. (b) A d-type electronic state at the tip end, protruding from the apex of a tungsten tip, interacts with a two-dimensional array of atomic states. Note that the tip- and surface-state are interchangeable and will result in the same Δz*

A constant current STM measurement images thus a constant local electronic density of states (LDOS) at a certain energy with DOS contributions from both bulk states and localized states. The STM image therefore contains topography information due to step edges and surface strain relaxation, chemical information (doping, electron affinity and effective mass) and information about the spatial extension of the wavefunction. For a better understanding of the tunnel process and justification of the assumptions made, we will have a closer look at the theory involved in spectroscopic techniques that are equally important for the imaging mechanism.

3.2.2   Scanning Tunneling Spectroscopy and CITS

In a Scanning Tunneling Spectroscopy (STS) measurement, the tip is positioned above the sample. The feedback loop is turned off in order to keep the tip-sample distance constant. A voltage sweep is applied to the tip to measure the tunnel current as function of voltage I(V). After the I(V) curve has been measured the voltage and current setpoint are restored to their original values, the feedback loop is switched on again and the tip is scanned further until the next point is reached where a I(V) curve needs to be taken. From these I(V) measurements, the normalized conductance $(\mathrm{d}I/\mathrm{d}V)/(I/V)$ can be derived and compared with the expected (surface) DOS [3,4]. As the measurement is performed at a certain set-point (tunnel current and tunnel voltage), all I(V) curves will go through this set-point. If one is interested in the empty state behavior of the sample, the set-point has to be chosen in the

filled state branch and *vice versa*, to avoid that the measurement is influenced by the chosen set-point.

If the tip-wavefunction in the vacuum is approximated by an *s*-state, than the tunnel matrix element *M* is proportional to the wavefunction of the sample at the position of the outermost tip atom at the tip apex, with its center located at position r_0.

When *M* (Table 3.1) assuming an s-type tip-state is inserted in formula 3.4, and we assume that the density of states (DOS) of the tip are without any structure with respect to the DOS of the sample (ρ_T=constant), we find for the tunnel current:

$$I(r_0, V) = \frac{16\pi^3 C^2 \hbar^3 e}{\kappa^2 m_e^2} \rho_T \int_0^{eV} d\varepsilon \rho_S^{local}(r_0, E_F^S + \varepsilon) \qquad (3.5)$$

and for the differential conductance at an applied voltage (V):

$$\frac{dI}{dV} = \frac{16\pi^3 C^2 \hbar^3 e^2}{\kappa^2 m_e^2} \rho_T \rho_S^{local}(r_0, E_F^S - eV) \qquad (3.6)$$

An STM measurement thus images the local density of states. From Eq. 3.4 it is then possible to obtain the sample DOS assuming that the tip has a constant density of states.

The derivative of the tunnel current with the tunnel voltage is proportional to the local DOS of the sample at the position of the tip (r_0) at energy E_F –eV. Formula 3.5 is the basis equation to interpret STM images of realistic systems, like semiconductors containing quantum wells or quantum dots. As the information about the tip orbital, which is hidden inside *C*, is unknown, an absolute tunnel current cannot be indicated.

When the sample topography is imaged in the constant current mode (I=constant), at low voltages (eV<<workfunction of the sample), the constant current images represent planes with constant local density of states (LDOS) at the Fermi-energy:

$$I \propto V \rho_S(r_0, E_F^S) \Rightarrow \rho_S(r_0, E_F^S) = constant \qquad (3.7)$$

In this formula the exponential dependence of the tunnel current upon the tip-sample distance can be recognized, if one takes into account that a sample wavefunction decays exponentially into the vacuum:

$$\Psi_S(r_0) \propto \exp(-\kappa z) \qquad (3.8)$$

Furthermore is becomes clear that the LDOS of the sample

$$\rho_s(r_0, E) = \sum_\mu \left|\Psi_\mu^S(r_0)\right|^2 \delta(E - E_\mu) \qquad (3.9)$$

are proportional to the squared wavefunction. Differentiating this to *V* yields for a structureless tip:

$$\frac{dI}{dV} \propto \rho_S(E_F - eV) \qquad\qquad (3.10)$$

By changing the tunnel voltage *eV*, it is thus possible to probe the LDOS of the sample. By doing so, in theory, it is possible to image the specific electronic structure by observing local maxima while scanning laterally over the surface. Chemical contrast in the STM images can be thus achieved. These formulas are of course only true if no tip changes occur due to atomic rearrangements of the atoms at the tip apex. This may alter the tip states e.g. from an *s*- to a *p*- or *d*-state and will alter the tunnel matrix element *M*.

Following the model of the *s*-type tip, important sample properties can be investigated by STM, without knowing the exact structure of the tip. Although this is widely used, this theory has some deficiencies. While comparing corrugation amplitudes qualitatively, it was demonstrated that *p*- and *d*-states are also very likely [2]. Also during spectroscopy it is often very difficult to get agreement between the experiments and the theory. Tsukada *et al*. [5] showed that the influence of the tip in dI/dV measurements can be estimated by:

$$\frac{dI}{dV} \propto \rho_T(E_F - eV)\rho_S^{local}(r(V), E_F - eV) \qquad (3.11)$$

This shows that the tunnel current is proportional to an effective DOS of the tip and the LDOS of the sample, however not at the position of the center of the outermost tip atom, but at a voltage dependent slightly shifted position r(V).

When taking I(V) spectra in every point of the STM image or in a grid, it is possible to obtain an image of the spatial current distribution at a certain image voltage. The thus obtained images are called Current Imaging Tunneling Spectroscopy Images (CITS). It is generally assumed that CITS images represent a map of the local wavefunction in the sample, which can be seen in formula 3.7 and 3.9. However when imaging at room temperature generally the separation between hole-states in a quantum well or quantum dot is not large enough to be resolved in the CITS measurements. In some cases (small dots), however, the separation between the electron states is even at room temperature sufficiently large to be resolved.

3.2.3 Tip-induced band bending (TIBB)

The tunnel current at a certain gap voltage *V* can be interpreted as a probe of the sample LDOS at an energy *eV* above the semiconductor Fermi energy level E_F. But, unfortunately, this is not true in general, because of tip-induced band bending (TIBB).

Typical values	
Electron affinity χ (GaAs)	4.07 eV
Bandgap E_g (GaAs)	1.41 eV
Band bending Φ	0.04 eV
Gap width d	0.9 nm
Workfunction tip Φ_m (W)	4.5 eV
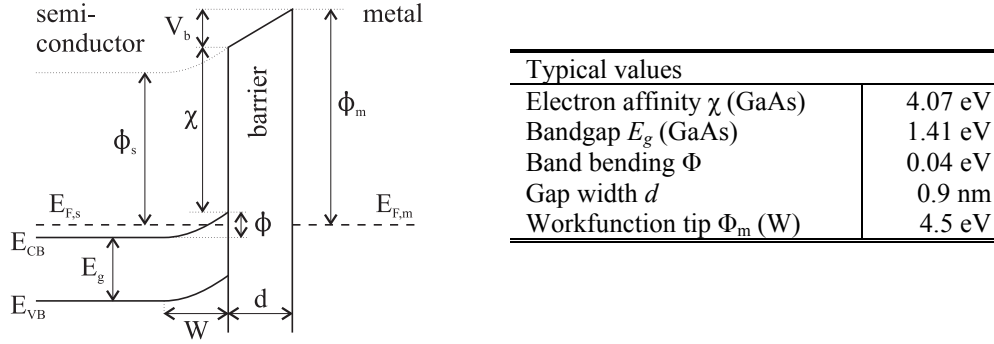
Fig. 3.3: *Parameters determining the tunneling process between a metal tip and semiconducting surface, and their typical values*

If two materials with different work functions (χ and Φ_m in Fig. 3.3) are brought close together (~1 nm), electrons will tunnel from the material with the highest work function to the material with the lowest work function. Charges at both surfaces will build up an electric field between the two surfaces. This process will continue until the Fermi levels of both materials have aligned and equilibrium exists. In case of physical contact between a metal and a semiconductor, this is called a "Schottky" contact.

This electric field between the two materials is shielded by space charges near both surfaces. In a metal, the high free electron density effectively shields the electric field and the width of the space charge region is of the order of only 0.05 nm. In a semiconductor material the electric field is shielded by charge carriers and ionized donors or acceptors. Therefore the width W of the space charge region depends on the doping concentration. The depletion length W is described by

$$W = \sqrt{\frac{2\varepsilon_0\varepsilon_r\Phi}{e^2 N_A}} \qquad (3.12)$$

where N_A is the doping concentration and Φ is the band bending at the surface of the semiconductor, see Fig. 3.3. For GaAs with a doping concentration of 10^{18}cm^{-3}, this screening length W is approximately 7 nm [6]. In an energy diagram this screening is related to the bending Φ of the conduction and valence band, see Fig. 3.3.

Applying a voltage between the tip and sample increases or decreases the existing electric field and creates additional surface charges in the semiconductor sample, which itself induces bending of the conduction and valence bands near the surface. The conduction and valence band edges at the sample surface shift in energy as a reaction on a change in the applied voltage. Depending on the doping concentration, the field penetrates the semiconductor sample, depleting it of free charge carriers leaving a space charge due to ionized donors or acceptors.
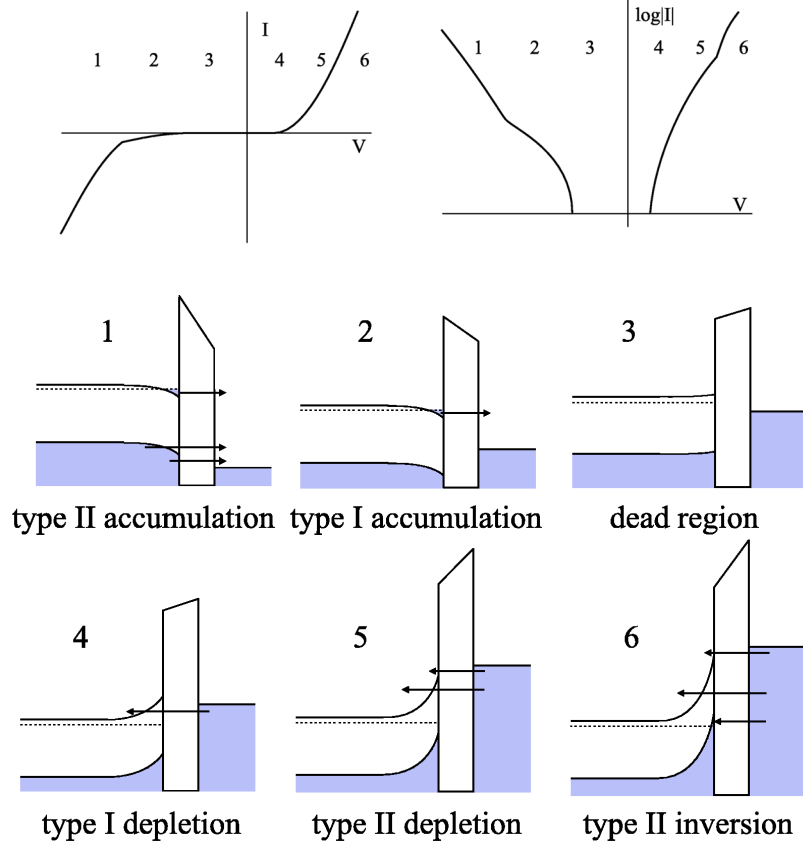
Fig. 3.4: *Tunnel current vs. tip-sample voltage for n-type doped samples (e.g. silicon doped GaAs). The tip induced band bending and the states contributing at different tunnel voltages are shown [7, Chapter 1 and 6]*

For a highly doped sample, the electric field is screened immediately by the space charge and the depletion layer is thin. TIBB then plays a minor role. But in low or undoped samples, the depletion length cannot be disregarded. For intermediately doped samples, still electrons can tunnel from and to bulk states at bulk conduction and valence band offsets. However, an additional tunnel barrier in the semiconductor, with a width of the depletion layer *W*, has to be taken into account (type I depletion), see Fig. 3.4. For very low-doped samples, this tunnel barrier is too wide for a current to occur. A shift of the conduction band and valence band edges at the surface will continue until either the conduction or valence band edge crosses the bulk Fermi level at the surface (type I accumulation or type II inversion). Population of the conduction band or depopulation of the valence band will then prevent further band bending. See [7] for a more extended description of tip-induced band bending and the contributing bulk and surface states.

3.3 Buckling behavior and electronic structure of cleaved III/V semiconductor surfaces

The (110) surface of III/V zincblende-type semiconductors, like GaAs, InP and InAs has in many respects become a model system for studies of semiconductor surfaces. Since the (110) surfaces of these compound semiconductors are natural cleavage planes, they can be produced by cleaving in ultrahigh vacuum (UHV) without the need of additional treatment. As in general atomically flat and absolutely clean surfaces can be obtained, this surface is extremely well suited for investigation by X-STM.

In the bulk of these semiconductors, {110} layers consist of planar zigzag chains of alternating group III and group V atoms along the [-110] direction (Fig. 3.5a), indicating that the (110) cleavage plane is a non-polar surface. Each surface atom of such cleaved surfaces possesses three nearest neighbors and has one dangling bond.

Upon cleavage, the surface of the bulk (Fig. 3.5b) will relax but in general the 1x1 surface unit cells will be retained. The group III element will move inward whereas the group V element will move outward. The bond lengths stay almost the same and only the atoms in the surface layer are displaced over a considerable distance. The relaxation or so-called buckling can be specified by a single parameter, the tilt angle ω (Fig. 3.5c), resulting in the values as indicated in table 3.2. The relaxation of the (110) surface can be understood by looking at the orbitals at the surface. On III/V semiconductor surfaces the dangling bonds of sp^3-type for the group III element surface atom are unstable. Therefore these bonds dehybridyze to form three planar sp^2-type bonds with the nearest group V atoms plus an empty p-like dangling bond on the group III surface atoms. On the group V surface atoms a double occupied (filled) p-type dangling orbital is formed, separated by about 90° from the three p-like bonds to the nearest element III atoms, extending into the vacuum.

Most III/V compounds are quite similar: they have the zincblende structure, are iso-electronic and most of them are direct semiconductors (with AlAs and GaP as important exceptions). For un-relaxed structures, theory predicts these surfaces to have surface states in the fundamental bandgap [8], due to the dangling bonds on the cleaved (110) surface. The buckling behavior, however, removes the surface states from the bandgap. A detailed description of zincblende semiconductors and their electronic properties can be found in [9,10].

Due to the opening of the surface bandgap of most III/V semiconductor surfaces there are differences in the observed surface topography when operating the STM in the filled (negative sample voltage) or empty state (positive sample voltage) imaging mode [11]. By tunneling at negative sample voltages, in the so-called filled state imaging mode, it is possible to extract electrons out of the filled dangling bonds below the valence band maximum. At this polarity the group V elements are imaged, as the filled state dangling bonds are located above these atoms. It is also possible to tunnel at positive sample voltage, in the so-called empty state imaging mode. In the empty state imaging mode electrons are injected into the empty states dangling bonds, which are energetically located above the conduction band minimum. The group III elements are imaged, as the empty state dangling bonds are located above these atoms. It is thus possible to selectively image the group III and group V elements.

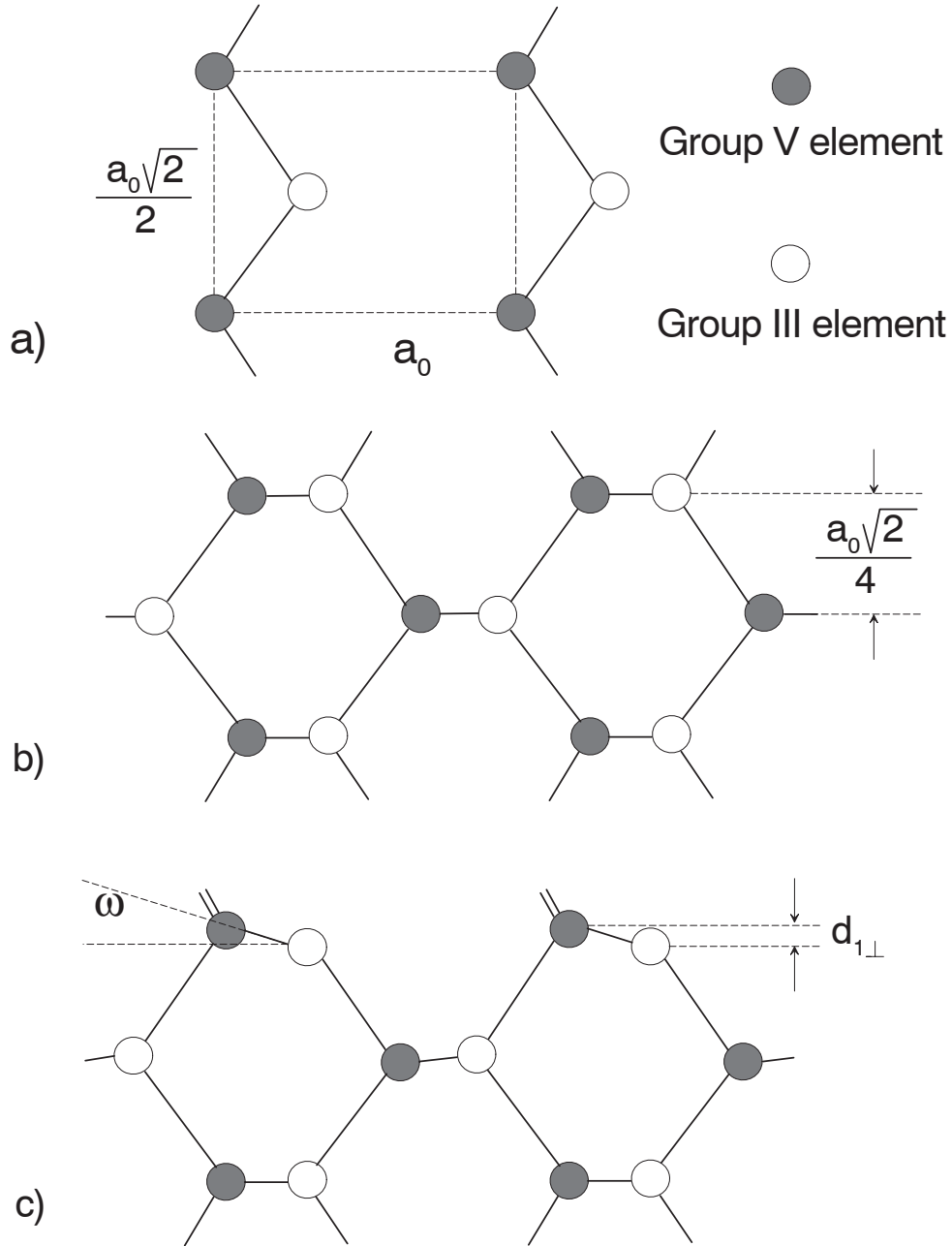**Fig. 3.5:** *Arrangement of atoms at bulk truncated and relaxed {110} surfaces of zincblende-structure compound III/V semiconductors. (a) top view, (b) un-relaxed side view (c) relaxed side view. Note that the filled states dangling bond (indicated by the double bond) is located at the anion (group V element) and that the empty dangling bond (no bond at all present) is located at the cation (group III element)*

Compound	a_0 (nm)	$d_{1\perp}$ (nm)
GaAs	0.5654	0.069 (0.065 - 0.071)
InP	0.5869	0.073 (0.057 - 0.076)
InAs	0.6036	0.078 (0.078 - 0.088)

Table 3.2: *Structural parameters of {110} surfaces of compound semiconductors. Values obtained from [9,12]*

3.4 Relaxation of cleaved surfaces

When two materials with different lattice constant are used in a heterostructure, this heterostructure is called a strained heterostructure because of the built-in strain. SK-grown quantum dots are the ultimate example of such strained heterostructures, but also lattice-mismatched quantum wells have built-in strain. When such a structure is cleaved, it reduces its built-in tensile or compressive strain by deforming the cleavage surface. Regions under compressive strain bulge outward while tensile strain depresses the cleavage surface.

For homogeneously strained mismatched layers of constant thickness, the strain relaxation at the cleavage surface can be calculated analytically. This theory cannot predict the relaxation of the highly inhomogeneous strain in quantum dots, but the results can be a guide to the relaxation of a partly exposed quantum dot, provided that its depth under the cleavage surface is much larger than its thickness. For the 2D problem, i.e. the strained quantum well problem, there exists an analytical solution to calculate the outward relaxation of the strained well upon cleavage, which was determined by J.H. Davies [13].
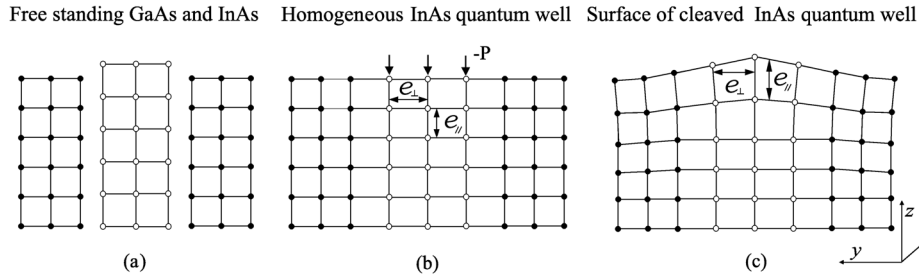
Fig. 3.6: *Strain relaxation at the cleaved surface of a strained heterostructure*

It is assumed that the elastic response is linear and isotropic, and that the elastic constants are the same everywhere. The structure containing the strained slab is assembled as shown in Fig. 3.6, following the "strain suppression" method of thermo-elasticity [14,15]. The slab and its two claddings are brought nearby without stress (Fig. 3.6a). A uniform stress of $\sigma_{xx}^{slab} = \sigma_{zz}^{slab} = -P$ is applied to the slab to reduce the lateral lattice constant. The slab can then be joined to the cladding layers without further stress (Fig. 3.6b). The fictitious stress applied in the previous step must be removed by applying an outward pressure of P to the exposed cleaved edge of the slab. The region near the surface of both well and cladding layers relaxes under this stress (Fig. 3.6c). In case of a quantum well in a semi-infinite

medium, with a uniform mismatch with an applied stress $\sigma_{zz}(y,z=0)=P$ for $|z|<w$, the stress obeys $\sigma_{yy}(y,0)=\sigma_{zz}(y,0)$ at all points on the surface. Then it follows that the surface of the cladding layers is unstrained (but not undistorted) and the surface of the well is uniformly strained, see Fig. 3.7. The total strains at the surface of the slab are

$$\varepsilon_{yy}=\varepsilon_0(1+2\nu), \quad \varepsilon_{xx}=-\varepsilon_0, \quad \varepsilon_{zz}=\frac{-2\nu^2\varepsilon_0}{1-\nu}, \quad \varepsilon_h=\frac{2\nu(1-2\nu)\varepsilon_0}{1-\nu} \quad (3.13)$$

in which ν is Poisson's ratio and ε_0 is the lattice mismatch. For an $In_xGa_{1-x}As$ quantum well lattice matched on GaAs, ε_0 is given by:

$$\varepsilon_0=\frac{a_{InGaAs}}{a_{GaAs}}-1 \qquad (3.14)$$

In which a_{InGaAs} is a linear interpolation of the lattice constant between GaAs and InAs: $a_{InGaAs}(x)=xa_{InAs}+(1-x)a_{GaAs}$. The surface lattice constant at the strain-relaxed surface a_s follows directly from the strain ε_{yy} in Eq. 3.13:

$$a_s=\varepsilon_{yy}\,a_{InGaAs} \qquad (3.15)$$

The normal component of the displacement of the surface follows immediately from the strain ε_{yy} and the normal component is given by [16]:

$$u_z(y)=C-\frac{2(1+\nu)\varepsilon_0}{\pi}\left\{(y-p+w)\log\left|\frac{y-p+w}{w}\right|-(y-p-w)\log\left|\frac{y-p-w}{w}\right|\right\} \qquad (3.16)$$

in which w is half the well width and p the y-position of the center of the well, see Fig. 2.11. An arbitrary constant C is present because for two-dimensional elasticity the displacement does not decay at infinity. For multiple quantum wells at different positions, the single quantum well solutions can be added.
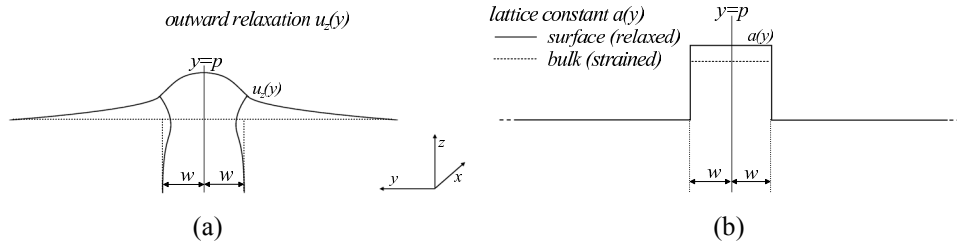
Fig. 3.7: *(a) Outward strain relaxation at the cleavage surface of a homogeneously strained quantum well and (b) the lattice constant at the surface and deeper in the sample*

The calculation can be extended for a non-uniform composition, where $\varepsilon_0(y)$ acquires an arbitrary variation during growth. The strain given by Eq. 3.13 is now proportional to the local value of $\varepsilon_0(y)$. The outward relaxation can be derived from the slope of the surface that is given by [16]:

$$\frac{du_z}{dy} = -2(1+\nu).\frac{1}{\pi}\int_{-\infty}^{\infty}\frac{\varepsilon_0(s)}{y-s}\,ds \qquad (3.17)$$

This equation can be solved analytically for a linear mismatch profile as well. If the mismatch is zero outside the well and changes linearly from $-\varepsilon_1$ at one side of the well to ε_1 at the other side of the well, the outward relaxation $u_z(y)$ is given by

$$u_z(y) = C - \frac{(1+\nu)\varepsilon_1}{\pi}\left\{\frac{(y-p)^2-w^2}{w^2}\log\left|\frac{y-p-w}{y-p+w}\right| + 2\frac{y-p}{w}\right\} \qquad (3.18)$$

If the mismatch profile can be split in a uniform (symmetric) mismatch and a linear (anti-symmetric) part the outward relaxation profile can be obtained by adding the symmetric (Eq. 3.16) and anti-symmetric (Eq. 3.18) relaxation profiles.

References

[1]   S. Blügel, Lecture Notes, *Theorie der Rastertunnelmikroskopie*, http://www.fz-juelich.de/iff/personen/S.Bluegel/Lectures/stm.ps

[2]   C.J. Chen, *Introduction to Scanning Tunneling Microscopy*, Oxford University Press, New York (1993)

[3]   R.M. Feenstra, Phys. Rev. B **50** (7), 4561 (1994)

[4]   R.M. Feenstra, J.A. Stroscio, J. Vac. Sci. Technol. B **5** (4), 923 (1987)

[5]   M. Tsukada and N. Shima, Jour. Phys. Soc. Jap. **56**, 2875 (1987)

[6]   M.C.M.M. van der Wielen, *Study of imperfections near the cleaved GaAs(110) surface by low-temperature scanning tunneling microscopy*, Thesis, Katholieke Universiteit Nijmegen, The Netherlands (1998), p29-35, p49-67, p114

[7]   G.J. de Raad, *Voltage-dependent Scanning Tunneling Microscopy on the {110}-surfaces of GaAs, AlGaAs and their heterostructures*, Thesis, Eindhoven University of Technology, The Netherlands (2001), ISBN 90-386-1709-7

[8]   I. Ivanov, A. Mazur and J.Pollmann, Surf. Sci. **92**, 365 (1980)

[9]   W. Mönch, *Semiconductor Surfaces and Interfaces*, 3rd ed. (Springer, Heidelberg, 2001), Chapter 7.

[10]   O. Albrektsen, *Scanning Tunneling Microscopy and Spectroscopy on III-V Semiconductor Compounds and their Interfaces*, Thesis, Chapter 2, Zürich (1990)

[11]   Ph. Ebert *et al.*, Phys. Rev. Lett. **77** (14), 2997 (1996)

[12]   Ph. Ebert, Surf. Scien. Rep. **33**, p. 131 (1999)

[13]   J.H. Davies *et al*. Journ. of Appl. Phys. **91** (7), 4171 (2002)

[14]   M.Y. He *et al*. Acta Matter **44**, p. 2353 (1996)

[15]   S.P. Timoshenko, J.N. Goodier, *Theory of Elasticity*, (McGraw-Hill, New York, 1970), Sec. 148

[16]   K.L. Johnson, *Contact Mechanics*, (Cambridge UP, Cambridge, 1985), Sec. 2.5

Chapter 4

Experimental setup and procedures

4.1   Introduction

This chapter gives a description of the STM and the ultrahigh vacuum (UHV) setup in which all experiments have been performed. Also the procedures that have to be passed through in preparation for a measurement, such as tip and sample preparation are discussed. Furthermore, the measuring procedure itself is explained briefly. An elaborate description of the tip fabrication can be found in [1,2].

4.2   The STM unit

The heart of an STM setup consists of a conductive sample and tip. The sample and tip are part of an electronic circuit. The tip is brought close to the sample. If the tip-sample distance is within the range of a few Ångstrom a tunnel current will occur when a voltage is applied. As mentioned previously, this tunnel current (~0.1 nA) depends exponentially on the tip-sample distance, which offers an accurate method to regulate the tip-sample distance by means of a feedback loop. The electronic circuit regulates the tunnel current by moving the tip up and down with respect to the sample surface by using a z-piezo tube, as is shown in Fig. 4.1. Perpendicular to this direction, two other piezo tubes move the tip over the surface, see Fig. 4.1. In all the measurements the scanner is operated in the "constant current mode", which means that the tip is scanned over the sample surface while keeping the tunnel current constant. The tunnel current is amplified in the electronic circuit by an I-V-converter (Fig. 4.2 D) and compared with the set image current. The tip z-movement is monitored and fed into a computer that composes a topography image of these scan profiles.
The STM setup is very sensitive to external vibrations, as the tip-sample distance is only a few Ångstrom and the small tunnel current is very sensitive to this parameter. Therefore, the setup is vibration isolated with different damping systems. The components of the scanner are made as rigid as possible especially the parts connecting the tip and sample holder, see Fig. 4.2 (AB). The scanner unit is suspended on a set of springs. Because this spring system is very sensitive to vibrations at the resonant frequency (0.7-1 Hz) of the springs, external damping is added. Copper plates connected to the scanner base plate are suspended between permanent magnets. Relative motion of the copper fins with respect to this magnetic field generates so-called Eddy currents that inhibit this motion, see Fig. 4.2 (C).
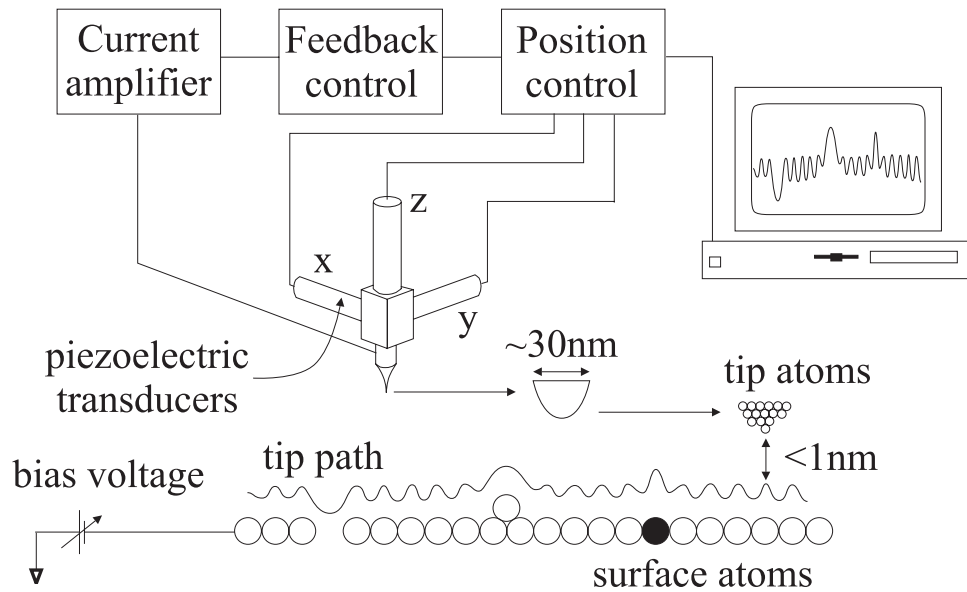
Fig. 4.1: *Schematic principle of STM*

This unit, together with the rest of the setup, is mounted on a heavy metal tabletop, see Fig. 4.3. Rubber dampers between this tabletop and the supporting frame filter out high frequency vibrations. Low frequency vibrations are suppressed by four active damping elements that are mounted between the floor and the frame. In this active damping system several motion detectors are present and several actuator-coils that counteract the detected motion of the system. One big advantage of this active damping system is that, next to the low resonance frequency of the system at which still some attenuation of vibrations can be obtained and the excellent overall attenuation of floor vibrations, external vibrations caused by *acoustic* noise are attenuated very fast. In this way, fluctuations in the tip-sample distance due to external vibrations are less than ~3 pm.
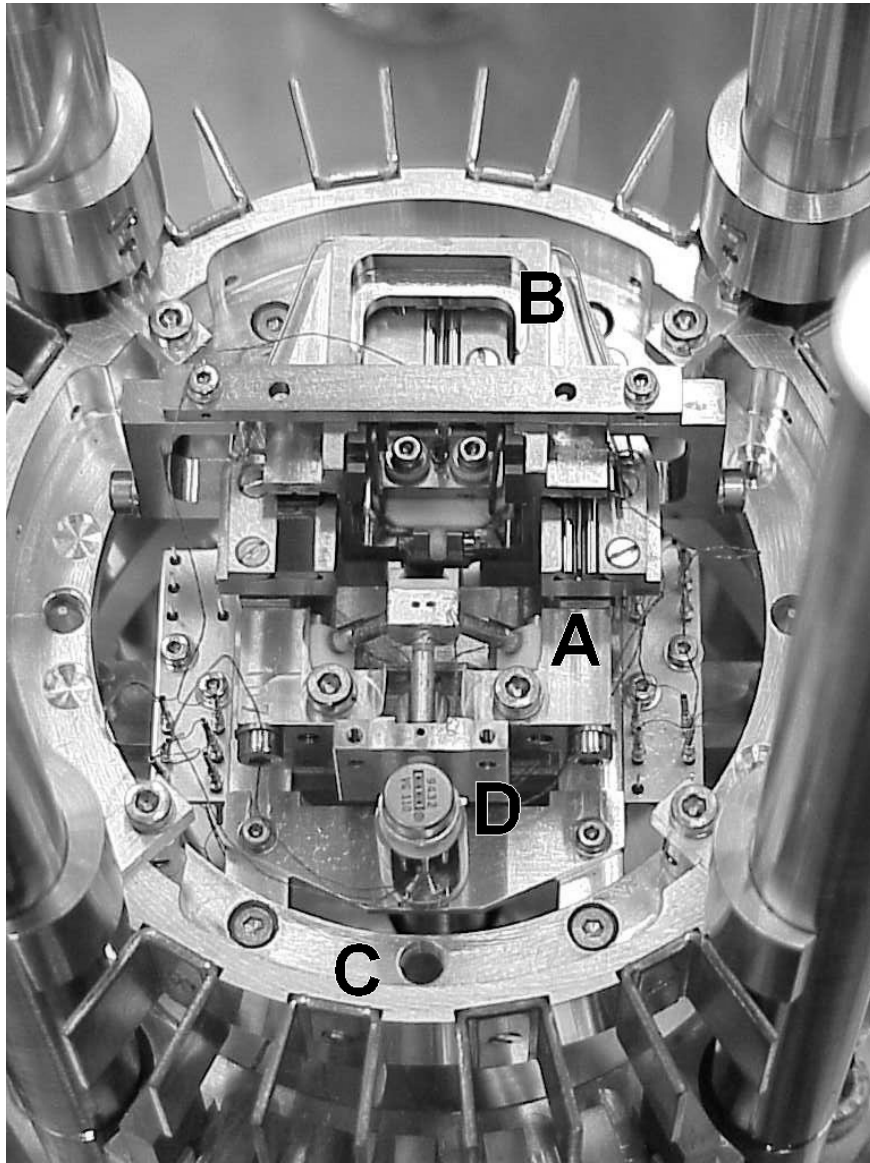
Fig. 4.2: *Omicron STM-1, TS2-scanner in the upper locked position. A: Tripod scanner, showing the 3 piezos, which are attached to the tip holder. B: Coarse-approach stage. The sample is placed in here, making it possible to move the sample in two dimensions towards the tip and towards the epi-layer. C: Eddy current damping stage. The copper fins are located outside the ring. In the lowered position these fins are positioned between the magnets. D: Current amplifier (I-V-converter). For noise reasons this amplifier is placed as close as possible to the tip, inside the UHV*

4.3   The UHV system

When the investigated samples are exposed to air, the surface is polluted and will be oxidized immediately, making accurate measurements of the surface impossible. Therefore, the measurements have to be performed in an ultrahigh vacuum setup, see Fig. 4.3.

The central vacuum chamber (STM), in which the STM unit is positioned, is pumped down by an ion-getter pump (Varian VacIon Plus, 300 liter/sec) with a titanium sublimation element (IGP/TSE) to a pressure lower than 5.10^{-11} torr. During X-STM measurements the inner panel of this IGP/TSE can be cooled down with liquid nitrogen, turning this pump in a kind of cryo-pump, enhancing the pump speed by a factor of 2. A valve separates this chamber from the preparation chamber (PREP). In this chamber the tips and samples can be prepared for the measurement. In this chamber an ion-gun, a self-sputter setup and a baking unit are installed for this purpose. Two oil-free turbo-molecular pumps (Varian V-250 and V-70), installed in cascade, keep the preparation chamber at a pressure of approximately 4.10^{-10} torr. This preparation chamber is connected to a load lock, which makes it possible to load and unload tips and samples within 20 minutes into and out of the system without seriously affecting the pressure in the preparation and STM chamber. The load lock is pumped with one of the turbo-molecular pumps (V-70) to a pressure of about 10^{-6} torr. A "dry" membrane pump (MP) provides the necessary pre-vacuum of about 10^{-1} torr. During the X-STM measurements all pumps are switched off to prevent vibrations, except the IGP/TSE as this pump contains no moving parts. Two wobble sticks in the STM and preparation chamber are used for manipulation and transportation of the tips and samples.
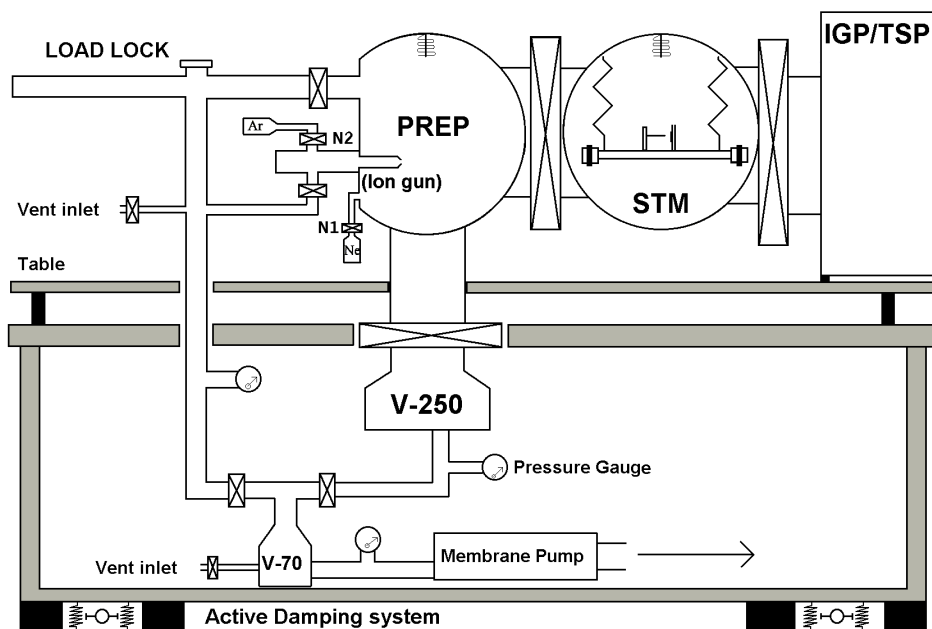

Fig. 4.3: *Schematic drawing of the UHV system containing the STM and damping system*

In order to maintain a good vacuum, some precautions have to be taken. All tips, samples and other objects entering the system have to be cleaned very thoroughly, by several cleaning steps in an ultrasonic bath using detergent, distilled water and ethanol.

4.4   Sample preparation

Small rectangular pieces ($\sim$3.5x10 mm^2) are cleaved from a wafer containing the semiconductor heterostructure of interest. These wafers are normally 350-450 μm thick. From such thick wafers it is impossible to obtain an atomically flat cleavage surface, which is absolutely necessary for the measurements. Therefore the samples are grinded down to a thickness of less that 150 μm. Samples thinner than 100 μm are hardly manageable.

For an STM measurement it is essential to have good electric contact with the sample. Although the samples themselves are (semi-) conductive, a simple mechanical contact between sample and holder is not sufficient because of an insulating oxide layer on the sample surface. Therefore, contacts are deposited on the sample, at the side of the epi-layer. This is done in a thermal evaporator. The samples are placed on a holder covering most of the sample. Only two small strips on both ends are uncovered. After the samples are placed in the thermal evaporator, the evaporation chamber is pumped down. A H_2 plasma treatment is applied for a few minutes to remove the oxide layer at the uncovered strips at both ends of the sample. During the plasma process, also the atomic structure of the top 10 nm of the sample surface is destroyed, resulting in an ohmic contact behavior at the sample surface. As the structures of interest are commonly located at more than 100 nm from the sample surface and laterally separated, this does not cause any problems concerning structural damage. After the plasma treatment, the contacts can be deposited on the samples. Depending on the sample, an n- or p-type contact is deposited by melting small pieces of metal in tungsten holders, which are heated by putting a high current through them. The evaporated metals will reach the uncovered parts of the sample and will stick to the sample surface, see Fig. 4.4. To obtain a good adhesion between the sample and the contact, a sequence of different metallic layers has to be deposited. For an n-type contact these are germanium, nickel and finally gold. The total thickness of the metallic contact layer is less that 0.5 μm. When the sample is taken out of the thermal evaporator, measuring the resistance across the sample between the two metal strip contacts can check the quality of the contact. After depositing the metal strips, the sample can be annealed to defuse the contacts deeper into the sample and enhance the electric contact between the metal strips and the underlying semiconductor material. This is, however, in general not necessary.
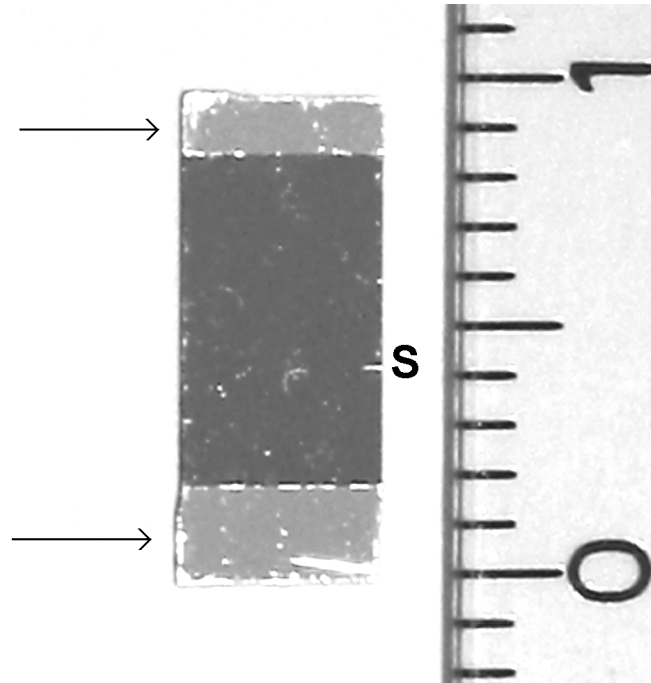
Fig. 4.4: *Picture of an STM sample prior to being clamped into the holder. The arrows indicate the metal contact strips. The scratch/notch is indicated by "S". The length of the sample is 10 mm*

Before the sample is clamped into the holder, a small scratch of about 0.5 mm, which extends to a small notch at the side of the sample, is applied to the epi-layer side of the sample, by using a diamond pen. The position of this scratch is chosen in such a way that after the sample is clamped into the holder, it will be located just above the clamping bars, see Fig. 4.5. This scratch will facilitate the cleavage of the sample later on in the UHV chamber and will provide a fixed starting point for the propagation of the cleavage plane. This greatly enhances the flatness of the cleavage plane.

Now, the sample is ready to be clamped in the holder. The sample holder consists of two metal bars that can be screwed together, thus clamping the sample. Part of these bars is removed, leaving a notch so that only one corner of the sample is clamped, see Fig. 4.5. One of these bars is connected to a support plate that fits in the STM unit. Before clamping, the holders are cleaned for use in UHV and the sample is cleaned with alcohol. A thin slice of indium (In) is placed on both sides of the sample holder before the sample is clamped. The sample holder is then heated and when the indium is melted, the screws are tightened. The indium provides for an even pressure distribution on the sample, preventing it from breaking and slipping out of the holder. The sample is now ready for loading in the UHV system. As there will be some water present on the sample surface and the holder, which can pollute the ultrahigh vacuum in the STM chamber, the samples are baked in the preparation chamber (PREP) of the setup. This is done by placing the sample holder close

to a heating coil, where it is baked out for about an hour at a temperature of approximately 150°C. In this way, water and other pollution will evaporate from the sample and its holder and are pumped away.
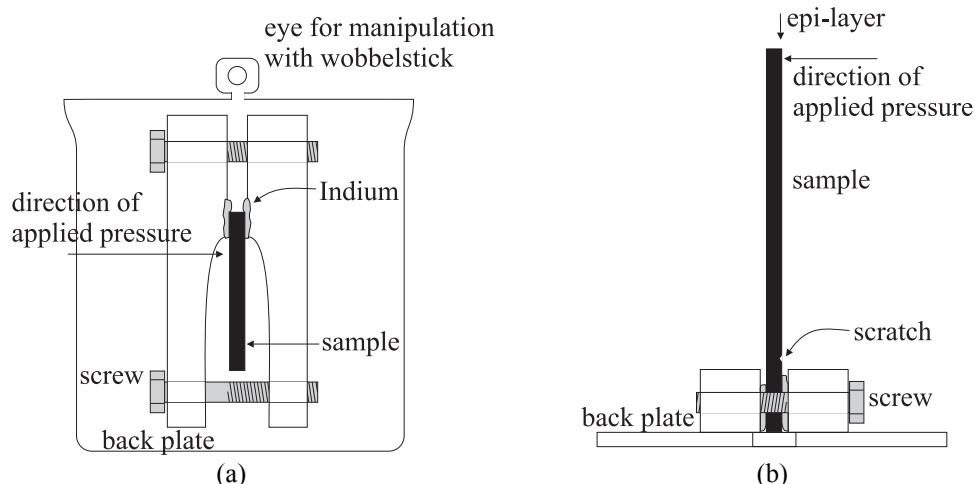
Fig: 4.5: *Schematic drawing of the sample in the sample holder. (a) top view and (b) side view*

The sample is cleaved *in situ* so that the surface stays clean and an atomically flat surface is revealed. If in the vacuum chamber, pressure is applied to the top of the sample, it will cleave starting from the previously applied scratch. Because the sample is only clamped at one corner, the cleavage plane can freely propagate through the sample. In order to obtain an atomically flat cleavage plane, the pressure point is located at about 1/4 of the clamping point of the sample, see Fig. 4.5, thus introducing a small amount of lateral torque in the sample. This torque facilitates the start of the cleavage at the scratch/notch, resulting in less force needed to accomplish cleavage. (This can be compared to ripping a piece of paper apart, where also the introduction of torque facilitates the start of the rupture). The cleavage plane will tend to follow a crystal plane, resulting in a nice atomically flat cleavage surface. The amount of force applied while cleaving the sample has to be kept as small as possible. Applying too large a force will always lead to stepedge formation, as the energy put into the cleavage plane has to be dissipated and the formation of stepedges is the easiest way of accomplishing this. However, even if the greatest care is taken while cleaving the sample, sometimes the cleavage plane will be rough due to clamping mistakes, simply bad luck, inaccuracy in the moves of the wobble stick during cleavage, or due to highly strained layers inside the sample. In the latter case, from our experience, the only solution is to make the sample as thin as possible (< 80 μm), making manipulation of the sample very difficult. Although we obtain generally flat cleavage surfaces (80%) the fabrication of atomically flat cleavage planes still is a topic of ongoing research [1,3,4]. Furthermore it is still very difficult to give an accurate explanation why this specific procedure, involving this precise selected point of applied pressure while cleaving, yields this extremely high success rate.

4.5   Tip preparation

Making STM tips that behave in a reproducible way is very important for obtaining high quality STM measurements. According to Equation 3.4, the tunnel current depends, in addition to the sample, also on the tip properties. This theoretical analysis assumes that there is only one atom at the top of the tip that contributes to the tunnel current. This means that the tip has to be very sharp and mechanically stable.

The tips are made of 99.97% pure poly-crystalline tungsten (W) wire with a diameter of 0.25 mm. A short piece of this wire (~5 mm) is spot welded to a tip holder and cleaned for use in UHV. The tips are then etched in a 2.0 molar KOH solution. The top 1-1.5 mm of the tip is put into the solution and a positive voltage (4-5 Volt) is applied to the tip-wire, as is shown in Fig. 4.6a. A Pt-Rh (90/10) spiral serves as counter electrode. In the etching process, the tungsten dissolves:

$$W_{(s)} + 2OH^-_{(aq)} + 2H_2O_{(l)} \rightarrow WO^{2-}_{4(aq)} + 3H_{2(g)} \qquad (4.1)$$
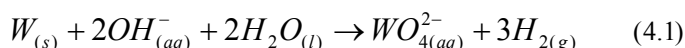
The beaker-glass in which the etching is performed, has a glass plate in the middle which ensures that the flow around the W wire is not disturbed by the H_2 bubbles that are produced at the Pt-Rh anode. Because of this geometry, the reaction velocity is the highest at point where the W wire penetrates the surface of the solution. This causes a constriction ("neck") of the wire at the surface of the etching solution, as the reaction products flowing down the tip shield the rest of the wire, resulting in a lower etching rate. Eventually, the wire will break at the "neck", leaving a very sharp tip. A current delimiter will immediately (<1 μs) interrupt the current at this point before the sharp point of the tip, which is still in the solution, is etched blunt. The tips are now ready for loading in the UHV setup.
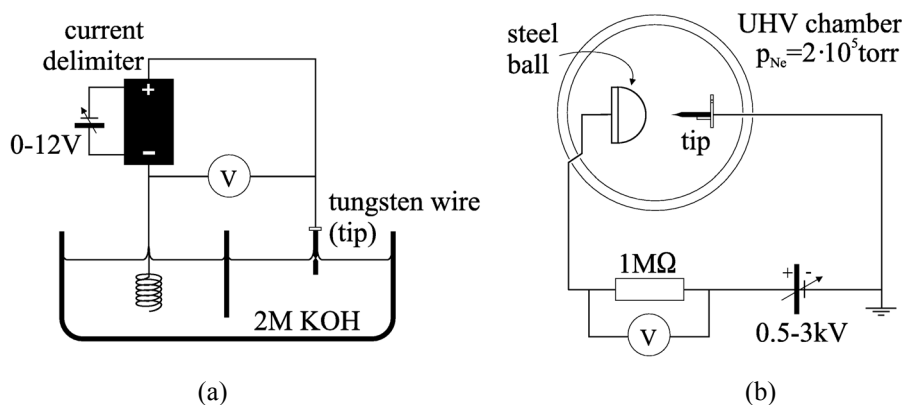

Fig. 4.6: *Schematic of the setup used for (a) etching the tips and (b) the self-sputtering*

After loading in the UHV setup, the tip and its holder are baked. Similar to the samples, they are put in front of a glow spiral and are heated until most of the water is evaporated. After that, the oxide layer on the tip is removed by heating the tip separately. For this, the

tip is brought in physical contact with a tungsten filament that is heated by putting a current (4-5 A) through it. The tip will glow orange, indicating that the temperature is about 900-1100°C. At this temperature, the oxide layer will be removed.

The tip is further sharpened by a self-sputter process. For this the tip is placed at a distance of about 3 mm from a steel ball, see Fig. 4.6b. Neon gas is admitted in the preparation chamber to a pressure of 2.10^{-5} torr. The tip is electrically grounded for safety reasons. On the steel ball, a positive voltage is applied (1000-2000V). This will create a strong electric field around the apex of the tip. Electrons are emitted from the tip, creating a current. The voltage necessary for creating this current (1 nA) is a measure of the radius of the tip apex and thereby a good indication of the tip quality. This is the so-called field emission voltage, and is described in detail in [1].

During the actual self sputtering process, a sputter current of 10 μA is maintained. Measuring the voltage across a 1 MΩ resistor monitors the sputter current, see Fig. 4.6b. The electrons, coming from the tip, ionize the Ne atoms. These Ne^+ ions are accelerated in the electric field and bombard the tip apex. The geometry of the electric field around the tip apex causes most of the ions to hit the tip just behind the apex. Furthermore, the ions that hit the side of the tip apex (so not perpendicular) will have a larger sputter yield. The ions will sputter away tungsten atoms, creating a constriction that finally breaks. In this way, very sharp tips can be obtained routinely. A more extended description of this sputtering process can be found in [1,2].

The final step in the tip preparation process is the ion bombardment. An ion source, installed in the preparation chamber, produces and accelerates argon (Ar) ions to about 1 keV, creating a parallel bundle. The tip is put in front of this bundle. The bombardment mechanically stabilizes the tip, without changing the actual tip radius too much. The tip is now ready for use in a measurement, as it is clean, sharp and stable.

4.6   The measurement

For a measurement, several tips and samples are prepared in case anything goes wrong. They are placed in the STM chamber of the UHV setup. The ion-getter pump is cooled down to liquid nitrogen temperature, to provide extra pumping capacity (about a factor of 2 can be achieved). The other pumps, two turbo molecular and one membrane pump, are switched off because they are a source of vibrations. One of the tips is placed in the scanner and one of the samples is cleaved *in situ* with the wobble stick. If the sample nicely cleaves along the scratch, a clean and atomically flat surface is created, exposing a cross-section of the epi-structure. The sample is placed in the scanner as well, see Fig.(4.2B). The tip is positioned in front of the sample. This is done by moving the sample with the coarse-approach table towards the tip (fig 4.2B), while observing with a CCD camera equipped with a tele-lens. When the tip is brought close to the cleaved surface, the reflection of the tip in the mirror-like cleaved surface is visible, indicating that the tip is indeed aligned above the cleaved sample surface. After the tip is properly aligned the sample will approach (automatically) the tip until tunnel contact is achieved. Once there is tunnel contact, the tip is moved to the edge of the cleavage surface of the sample where the epi-layers are located. The exact position of the tip with respect to the epi-layer structure is now known and the layers of interest can then be traced by moving the sample sidewards with the coarse-approach table (Fig 4.2B), which is calibrated within 165 nm. The scan parameters like

image voltage and image current are set and scans of the surface are made. A computer does all data acquisition and the processing of the data into images.

4.7   Scanning Tunneling Spectroscopy

Section 3.2.2 shortly introduced a Scanning Tunneling Spectroscopy (STS) measurement. An area is imaged at a certain image current and voltage. These parameters determine the tip-sample distance. A grid with a predefined density determines the points at which the spectroscopy data is obtained. The grid can consist of several hundred to several thousands of data points (e.g. a 10x10 or 400x400 grid). At these points, the feedback loop is turned off to keep a constant tip-sample distance during the spectroscopy measurement. A voltage ramp is applied on the sample and the current is measured. The data obtained at different points on the surface can be averaged to obtain an accurate $I(V)$ curve, from which the voltage dependent behavior can be analyzed. Spatial contrast can be derived from images showing the tunnel current at a specified voltage, the so-called Current Imaging Tunneling Spectroscopy (CITS) images.

References

[1]   G.J. de Raad, *Voltage-dependent Scanning Tunneling Microscopy on the {110}-surfaces of GaAs, AlGaAs and their heterostructures*, Thesis, Eindhoven University of Technology, The Netherlands (2001), ISBN 90-386-1709-7

[2]   G.J. de Raad, P.M. Koenraad, J.H. Wolter, Journ. of Vac. Sci. and Tech. B **17** (5), 1946 (1999)

[3]   M.A. Rosentreter *et al*., Phys. Rev. B **56** (16), 10538 (1997)

[4]   K. Sauthoff *et al*., Phys. Rev. B **60** (7), 4789 (1999)

Chapter 5

Real relaxation of strained structures:
Suppression of electronic contrast in STM measurements

5.1 Introduction

When a semiconductor structure containing strained layers such as quantum wells or quantum dot layers is cleaved, the surface will relax outward in order to release the build-in strain. This outward relaxation is directly linked to the composition of the strained layers, and can thus provide accurate information about the local composition of these layers. By using cross-sectional Scanning Tunneling Microscopy (X-STM) it is possible to measure this outward relaxation.

The measured height profiles, however, are also dependent on the chemical composition of the measured surface, as the bandgap of different materials is different, which results in a different tunnel current when scanning across these different materials. As the tunnel current is kept constant in our STM measurement this change in local bandgap will cause the STM tip to move down- or upwards in order to keep the tunnel current constant. This movement of the tip results in an extra (electrical induced) height contrast in the images, although the scanned surface might be atomically flat [1].

In order to analyze only the outward relaxation, it is necessary to suppress this chemical (or electrical) component in the STM measurements. In this chapter the relaxation of strained quantum wells is discussed, as samples containing these structures can be produced with high quality and can be easily investigated with various techniques. Furthermore, the relaxation upon cleavage of these systems provides a 2D problem. The calculation of the outward relaxation upon cleavage can be solved analytical, as we will show in this chapter.

5.2 Height contrast in STM

In Scanning Tunneling Microscopy measurements the local density of states (LDOS) of a (semi-) conducting surface is imaged. In the constant current imaging mode, the apparent topography consists of contributions from the "real" topography (e.g. stepedges) and changes in the LDOS due to e.g. chemical differences. If a sample, containing strained layers such as a strained quantum well, is cleaved, the surface will relax outward in order to

release strain [2]. This outward relaxation can be directly linked to the local composition of such strained layers. In order to be able to determine this local composition, the "real" topography has to be separated from the topography originating from differences in the DOS, due to chemical differences between the materials of the strained layers and the surrounding matrix [2-4].

The apparent height of the relaxation profiles of cleaved strained structures, measured with X-STM, is dependent upon the tunnel voltage at which the profiles are taken. This voltage dependent behavior of the apparent measured height in STM measurements can be explained by examining the tunnel process in more detail [2,5]. The relevant electron states involved in the tunnel process lie within the energy window between the sample and tip Fermi energy state and do not equally contribute to the tunnel current [6]. The decay length of the wavefunctions at the relevant electron states depends on the height of the vacuum barrier of the specific state under consideration. The higher the vacuum barrier, the shorter the penetration depth of the wavefunction in the vacuum barrier is, see Fig. 5.1a. This results in a decrease of the tunnel probability, as the overlap between the tip and the sample wavefunctions decreases.

The vacuum barrier between the tip and the sample is classically a forbidden region for the electrons. In this region the wavefunction can be expressed as:

$$\psi(z) = \psi(0)\, e^{-\kappa z} = \psi(0)\, e^{-\frac{\sqrt{2m\varphi}}{\hbar} z} \qquad (5.1)$$

where φ is the vacuum barrier height, z the tip-sample distance and m the electron effective mass. The tunnel probability w of this state is:

$$w \propto |\psi(0)|^2\, e^{-\frac{2\sqrt{2m\varphi}}{\hbar} z} \qquad (5.2)$$

The tunnel probability shows an exponential dependence on the vacuum barrier height, which is different for different states that contribute in the electron tunnel process. Electron states observing the lowest vacuum barrier will thus dominate the tunnel process, see Fig. 5.1b.

For tip Fermi energies aligned with the GaAs conduction band minimum (CBM) (empty state imaging), the increase in current can be huge when moving from the GaAs to the InGaAs, see Fig. 5.1c. Due to this increase in current, the feedback system of the STM will retract the tip, in order to maintain a constant current. This results in an "*apparent*" height profile of the investigated structure. However, at energies high above the CBM, the electronic contrast is much lower as the tunnel current is dominated by electron states high above the conduction bands, see Fig 5.1c. Thus high tunnel voltages are needed in order to suppress the apparent or chemical contrast.

For tip electronic states near the valence band maximum (VBM) of the semiconductor surface (filled state imaging), a similar effect occurs. However, the vacuum barrier heights

are in this case much larger, which results in a shorter penetration depth of the wavefunctions. Furthermore, the differences in barrier height above the GaAs and InGaAs are much smaller with respect to the total barrier height and thus are the differences in the tunnel probability when tunneling above the two materials smaller.
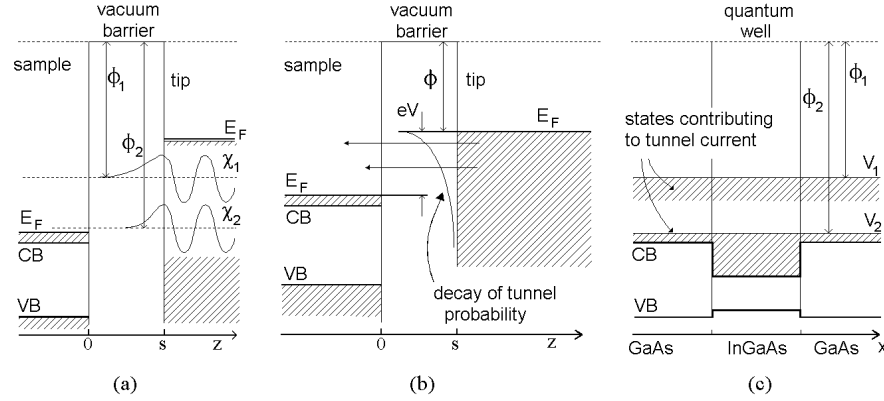

Fig. 5.1: *(a) Electron state wavefunctions at a different energy show a different penetration behavior in the vacuum barrier. (b) The tunnel current is dominated by contributions from electron states having the lowest barrier height. This is due to the decay of the tunnel probability as function of vacuum barrier height. (c) Tunneling at different tip voltages above different materials results in different relative contributions of the electronic states involved in the tunnel process*

These two effects cause a much smaller voltage dependence of the apparent relaxation profile. By putting a negative voltage on the sample, these states can contribute to the tunnel process. Furthermore, for several III/V semiconductor compound heterostructures (e.g. GaAs/AlGaAs/GaAs and GaAs/In$_x$GaAs$_{1-x}$/GaAs with certain x) the difference in valence band energy (i.e. the bandoffset) is smaller than the difference in conduction band energy [7], which again leads to a smaller voltage dependence in the filled state imaging mode. In order to obtain STM images that only show the "real" topography, the measurements should be performed at high (preferable negative) voltages [8].

5.3   Calculation of the electronic contrast using *IVCHAR*

In order to verify the previously presented imaging mechanism causing electronic contrast in STM images, calculations have been performed using the *IVCHAR* program, which is based on the theory described in [5]. The *IVCHAR* program uses only a 1D model whereas the real situation is of course 3D. This program constructs, for a given bias voltage and tip-sample distance, the potential profile as a function of the spatial coordinate z by solving the Poisson equation, under the condition that the electric field in the region of interest remains continuous. In the calculation, the effect of image charge is taken into account by subtracting the potential barrier, that is "sensed" by an electron between two metal plates, from the calculated vacuum level. The amount of tip-induced-band-bending (TIBB) and the

tunnel probability as function of energy is taken into account. Using the *IVCHAR* program, it is also possible to calculate the tip-sample distance at different tunnel voltages at a set tunnel current for different material systems, see Fig. 5.2a. By calculating the tip-sample distances for tunneling on GaAs and $In_{0.144}Ga_{0.856}As$ it is thus possible to determine the difference in tip height while tunneling on the GaAs and the InGaAs. The electronic contrast as function of tunnel voltage can thus be determined. In Fig 5.2 an example of a calculation is shown. The *IVCHAR* program had to be modified, because the band offsets of freestanding InGaAs shift with respect to the vacuum level due to pseudo-morphic strain, when the InGaAs layer is incorporated between GaAs layers. These offsets have been calculated by using the model solid theory of van de Walle [9] and have been fed into the *IVCHAR* program in order to be able to calculate the electronic height contrast of the InGaAs quantum well within the GaAs matrix.

As shown in Fig. 5.2b the electronic contrast indeed decreases with increasing tunnel voltage. At low voltages this does not always have to be the case, but in the voltage range were the STM is generally operated (above 1 Volt, both in filled and empty states), this is generally true, so it will always be possible to suppress the electronic contrast by using high tunnel voltages. For the empty state imaging mode the effect is indeed larger than for the filled state imaging mode, as was already predicted in the previous paragraph, showing that for suppression of electronic contrast indeed the filled state imaging mode is best suited. As was already mentioned, the usage of rather high voltages (> 2.8V) is preferred. It needs to be noted that even at high tunnel voltages a small electronic height difference (< 10 pm) between the filled and empty state imaging mode remains. The absolute value of the electronic contrast does not go entirely to zero for high tunnel voltages (even in the filled state imaging mode) and some electronic contrast between the GaAs and InGaAs remains. This is due to the differences in the bulk DOS of the different materials. The DOS are determined by the effective electron mass (m^*), which differs for InGaAs and GaAs and thus results in a different tunnel current (and measured apparent height) above the two materials. This difference is dependent on the doping concentration used in the calculation and whether the doping is n- or p-type. This is due to the fact that the position of the Fermi-Energy and thus the magnitude of the tunnel components originating from the valence and conduction band are influenced by this.
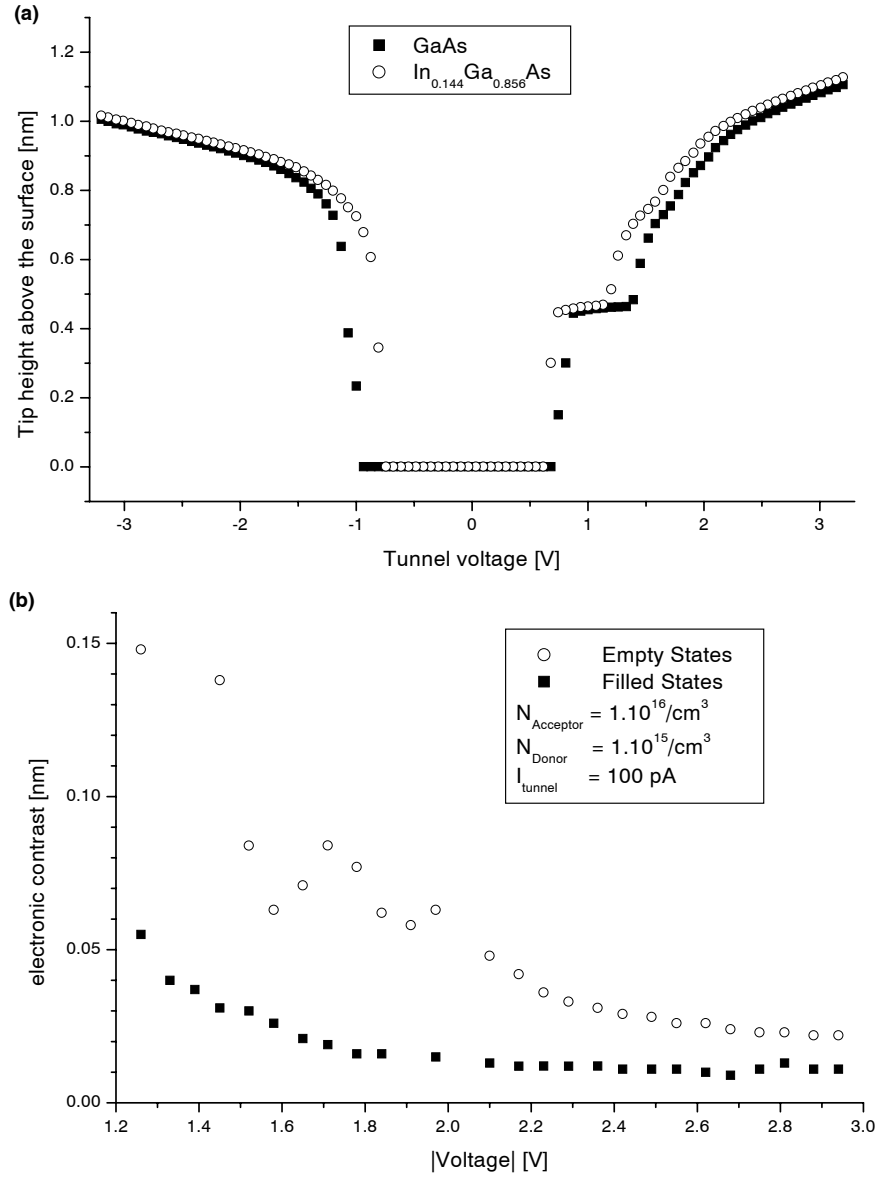
Fig. 5.2: *Calculated voltage dependence of the height contrast due to electronic contrast, between an In$_{0.144}$Ga$_{0.856}$As quantum well and a surrounding GaAs matrix. The calculation has been performed for a fixed tunnel current of 100 pA, a donor concentration of 1.10^{15}/cm^3 and an acceptor concentration of 1.10^{16}/cm^3. (a) Absolute distance between the tip and a GaAs and InGaAs surface as function of applied tunnel voltage. (b) Height difference between GaAs and InGaAs due to electronic contrast. The height contrast due to bulging out of the surface caused by strain is not included*

5.4   The sample

We investigated a sample consisting of a double InGaAs quantum well (QW) within a GaAs matrix. The sample was grown by Molecular Beam Epitaxy (MBE), see Table 5.1. The actual indium content of the wells turned out to be quite different than intended due to a problem during MBE growth (see Fig. 5.3), so the actual indium content of the wells had to be determined by using several techniques.

Thickness	Al	Ga	In	As	Doping	Temp. (^{o}C)	#
0.10μm		-			p 1.20*10^{19}	500	
1.35μm	22	78		-	p 5.05*10^{17}	730	
0.40μm	16	84		-	p 2.45*10^{16}	730	
800.0 Å	8 →16	92→84		-		730	
100.0 Å		-		-		730	
55.0Å		80	20	-		730	
100.0Å		-		-		560	
55.0Å		80	20	-		560	
100.0Å		-		-		560	
400.0Å	8	92		-		560	
400.0Å	10	90		-		730	
0.37μm	16	84		-	n 2.45*10^{16}	730	
5.7 Å	23	-		-	n 6.12*10^{17}	730	x45
3321.1Å		77		-	n 4.74*10^{17}	730	x45
1000.0Å		-		-	n 6.48*10^{17}	725	
1000.0Å		-		-	n 6.48*10^{17}	700	
1000.0Å		-		-	n 6.48*10^{17}	610	
Substrate			n^{+} GaAs				

Table 5.1: *Growth menu of the double quantum well structure*

The sample was cleaved *in situ* and the (110) cleavage plane was investigated by X-STM in the constant current mode. By measuring at positive or negative sample voltage, with respect to the tip which is grounded, it is possible to tunnel into the empty conduction band surface states, which are located at the group III elements for a cleaved (110) surface of III/V semiconductor crystals, or out of the filled valence band surface states, which are located at the group V elements [10]. By measuring at the proper polarity of the tunnel voltage, it is thus possible to be sensitive for either the group III (positive voltages) or group V (negative voltages) elements in the top layer of the cleaved surface.

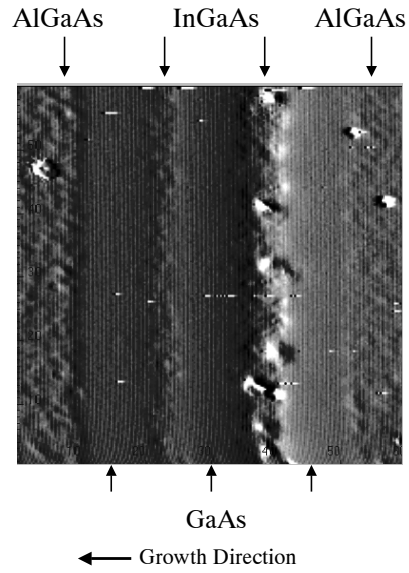**Fig. 5.3:** *X-STM image of the structure (60x60 nm²) showing the interfaces between the AlGaAs, GaAs and InGaAs. The difference in thickness between the two InGaAs quantum wells is very pronounced*
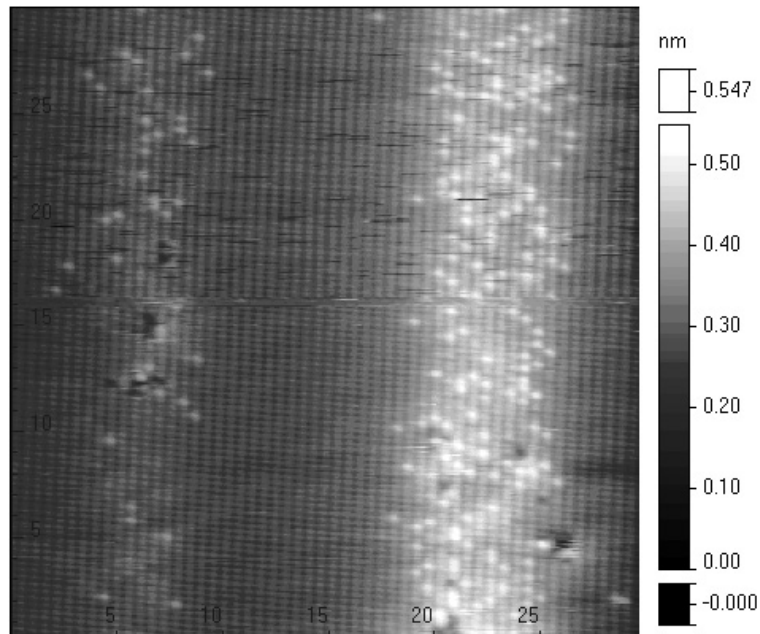

Fig. 5.4: *Atomic resolution X-STM image (30x30 nm²) of the double InAs quantum well structure. Tunnel voltage V = +2.5 V, tunnel current I = 198 pA*

From X-STM images with atomic resolution, the width and the local indium concentration of the quantum wells can be determined, see Fig. 5.4. In the STM images the individual indium atoms can be identified using the chemical sensitivity of the STM measurements. Because of the difference in bond-length and electrical properties of indium and gallium, the individual indium atoms can be distinguished from the surrounding GaAs matrix. By measuring at positive tunnel voltages (empty state imaging mode) the local indium fraction throughout the two QWs, see Fig. 5.5, can be determined by counting the indium atoms.
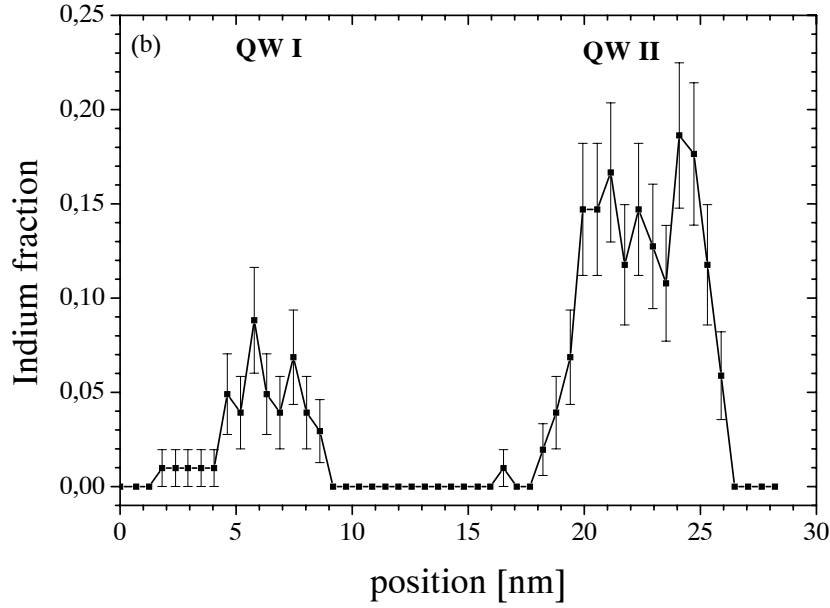
Fig. 5.5: *Indium concentration profile derived from the X-STM image by counting atoms*

We compared our X-STM results concerning the determination of the composition of the QWs, with the standard techniques: photoluminescence (PL) and X-ray diffraction (XRD) measurements, see Table 5.2. The PL experiments were performed in a standard flow cryostat at 5 K using a diode pumped Nd:YAG laser operating at 25 mW at 532 nm and a backscattering configuration with a scanning spectrometer and a liquid nitrogen cooled CCD camera. The calculations are based on an effective mass approximation using parabolic bands and the solid-model theory of Van de Walle [9], which is used to calculate the band offsets between the different layers of the structure.

	Width (nm)	Indium concentration (%)		
Well	X-STM	X-STM	XRD	PL
QW I	4.5 ± 0.5	5.0 ± 0.5	5.2 ± 0.5	6.3 ± 0.5
QW II	6.5 ± 0.5	14.4 ± 0.6	13.7 ± 0.5	14.7 ± 0.6

Table 5.2: *Indium concentrations of the quantum wells determined by X-STM, XRD and PL*

In the model used to interpret the PL and XRD spectra, the well width has to be inserted. This well width is determined from the X-STM measurements. From the indium fraction profile throughout the quantum wells, see Fig. 5.5, it can be seen that the indium content in the quantum wells can be considered to be constant within the accuracy of the measurement.

5.5   X-STM results

Fig. 5.6 shows the apparent relaxation profiles of the quantum well structure imaged at different positive image voltages (empty state imaging). At low voltages the chemical contrast can be as high as the topographical contrast.
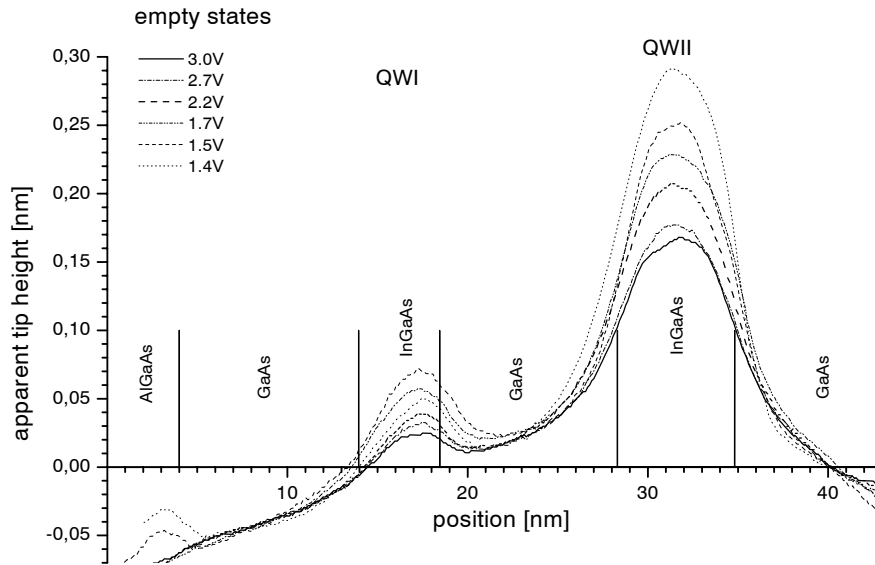

Fig. 5.6: *Apparent outward relaxation profiles for QW I and II at different positive tunnel voltages*

From these profiles, and other profiles measured in the filled state mode, the apparent height of QW II is determined at each tunnel voltage, see Fig. 5.7. This height measurement is performed at the center of the well with respect to the surrounding GaAs, far away from the wells.
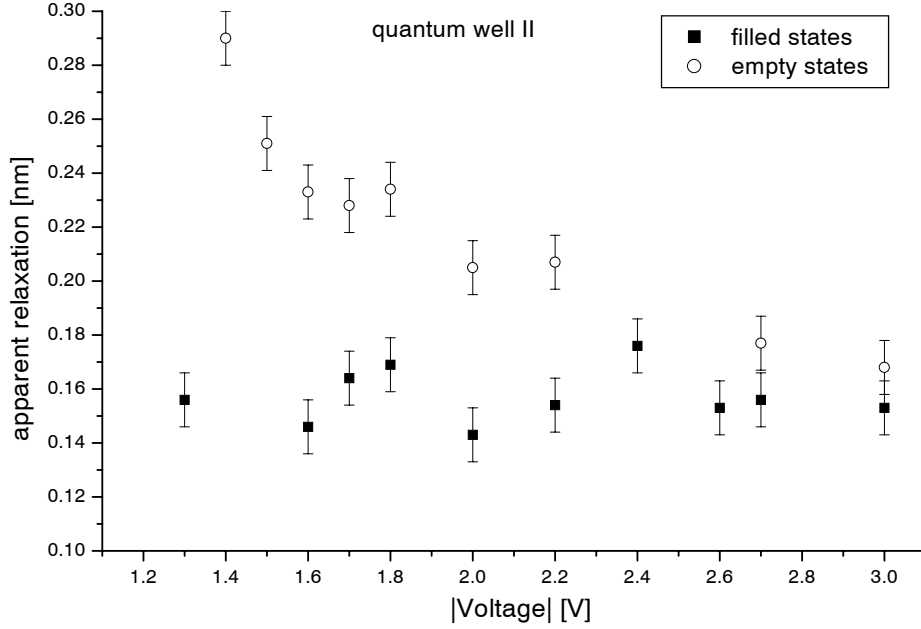
Fig. 5.7: *Apparent outward relaxation height at the center of QW II as a function of applied tunnel voltage*

The apparent relaxation profiles obtained from the filled state images are, as expected, less dependent on the applied tunnel voltage than the empty state profiles. In the empty state imaging mode there is, as predicted, a strong electronic contrast at low tunnel voltages. In the *IVCHAR* calculations the used donor and acceptor concentrations are chosen in such a way that the material is slightly p-type. In MBE growth, in general the material that is grown to be intentionally undoped (intrinsic) shows a small p-type behavior due to carbon that is incorporated into the material during growth. Although the calculation model uses a 1D approach it is possible to compare the STM results with the calculation from section 5.3 to a certain degree. The measured quantum wells are located in an intrinsic region within a p-i-n junction. When comparing the measured relaxation profiles with the *IVCHAR* calculations, the measured dependence of the apparent relaxation on the tunnel voltage in the empty state imaging mode is well predicted, as is the difference in measured apparent relaxation between the filled and empty state mode. For the filled state measurements, there is a discrepancy between the calculated and measured values at low tunnel voltages, as the measured profile seems to remain constant in the measured voltage window. This can be due to the fact that there are some difficulties with the 1D approach used in the calculations. The model used is only valid for a large InGaAs region in GaAs. As soon as a real quantum well is formed, confined states inside this quantum well are formed, enlarging the effective bandgap inside the InGaAs well. This extra contribution in the bandgap, which is not equally distributed over the conduction and valence band, introduces extra offsets upon tunneling out of the valence and into the conduction band. Furthermore, the quantum well structures have been grown within a p-i-n structure (see Table 5.1), which causes lateral

band bending of the conduction and valence bands in the quantum well region. The whole band structure is shifted relative to the tip-Fermi level. This causes the data points in Fig. 5.7 to be shifted along the voltage axis. Also, the p- and n-type concentrations are not exactly known. Although *IVCHAR* does not completely describe everything, it is nevertheless a tool that can be used to get a better insight in why electronic contrast occurs and how it can be suppressed effectively. The residual electronic contrast at high tunnel voltages is about 10 pm for this case, both according to the calculation and the measurement.

In conclusion, it can be stated that the voltage dependent X-STM measurements of the height profiles show that filled state images or high voltage empty state images are indeed best suitable for obtaining real topographic information, as was suggested by the theory and our calculations.

5.6 Analytical solution of the relaxation and lattice constant profile of the cleaved quantum wells compared with the measurements

The lattice constant profile throughout the quantum well layers can be determined from Fig. 5.4 by measuring the distance between the atomic rows. However, in order to get accurate results, some averaging is necessary. As can been seen in Fig. 5.4 a single indium atom can locally alter the lattice constant. By applying a Fourier filter perpendicular to the growth direction, these local fluctuations can be averaged out. The lattice constant at each atomic row is then calculated by taking the average distance to the left and right atom row. The thus obtained lattice constant profile is shown in Fig. 5.8. The lattice constant changes abruptly at the interfaces between the quantum wells and the surrounding GaAs matrix. The value of the lattice constant throughout the wells however, can be considered to be constant, which is in good agreement with the calculations. To obtain numerical agreement, however, higher indium concentrations than deduced from the X-STM measurements are needed in the calculation: 7% and 17.1% instead of 5% and 14.4%. The predicted calculated distortion of the surface appears to be too small. The measured lattice constant of the GaAs matrix exactly agrees with the theoretical value, showing that the STM is calibrated properly.

In Fig. 5.9 the measured relaxation, determined from an X-STM image measured at the tunnel conditions that show the minimal electronic contrast, is compared with the calculations. The overall shape of the calculated profile is again qualitatively consistent with the measurements. Again the calculated relaxation is smaller than the measured profile. A better fit can be achieved by using the increased indium concentration that was determined from the calculated lattice constant profiles i.e. 17.1% for quantum well II.
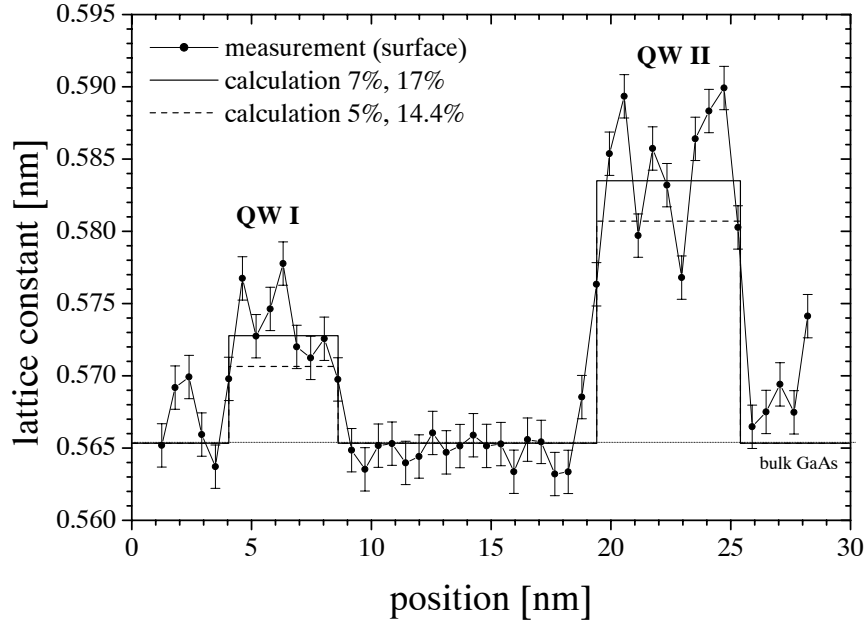
Fig. 5.8: *Lattice constant profile at the cleavage plane obtained from atomic resolution X-STM images*
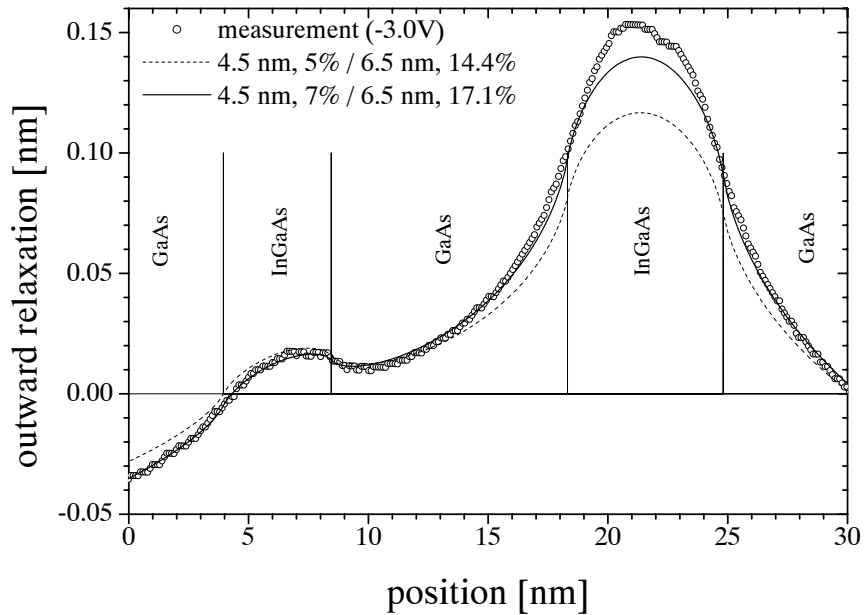

Fig. 5.9: *Outward relaxation profile of the double quantum well, compared with calculations of the outward relaxation. $V_{tunnel} = -3.0$ V, $I_{tunnel} = 110$ pA*

At a qualitative level the agreement between the theory and experiments is good. The prediction that the lattice constant of the GaAs should be unaffected at the surface, while that of the quantum well is changed by a constant factor, is justified. Also, the shape of the outward relaxation of the cleaved surface is described well. The magnitude of the relaxation predicted by the calculations, however, is only 80% of that measured in the experiments. This discrepancy can have several causes:

It could be that the X-STM measurements are unrepresentative of the bulk because of artifacts that could be caused by cleaving the sample, like desorption of indium for example. However, there is a good agreement between the three determinations of the indium concentration summarized in Table 5.2. Also no defects or vacancies are observed in the X-STM images. It also seems unlikely that the estimate of the width is influenced by the extreme slope of the surface at the edges of the well (Eq. 3.18). The problem probably lies in the way a cleaved surface behaves and the way it is imaged during the STM measurements and/or in one of the assumptions on which the calculation is based [11]. Concerning the STM measurements a few comments can be made:

(1)   During filled state imaging, only the arsenic lattice is visible in the STM images and the indium atoms in the top layer of the cleaved surface are thus not visible. However, an indium atom in the second layer, which is much larger than a gallium atom, will push up the arsenic atom in the top surface layer by about 16 pm in the STM images. This will give an increase of the measured relaxation profile in the quantum well, which is not included in the calculation.

(2)   When a III/V (110) semiconductor surface is cleaved, the surface reconstruction and buckling angle of the surface depend on the composition of the cleaved layer. The resulting relaxation of the arsenic lattice is 10-20 pm larger for a cleaved InAs surface than for a GaAs surface [12]. This again will give an extra increase in the measured relaxation profile of the quantum wells during filled state imaging.

(3)   The effects mentioned in 1 and 2 are given for pure InAs and GaAs. When considering a layer with an indium content of about 17% the resulting total extra measured outward relaxation in QW II will be about 6 pm. When including this in the calculation, a better fit with the calculated 17.1 % indium content profile is obtained, especially inside the actual quantum well region. Also considering a residual electronic contribution of 5-10 pm yields a better fit. This is, however, sill in disagreement with the indium content of 14.4 %, which not only has been determined locally by STM, but also by techniques that determine the average indium concentration on a larger scale, i.e. PL and XRD [11].

5.7   Conclusions

The voltage dependent electronic height contrast in STM images can be understood in terms of differences in tunnel contributions from the conduction and valence bands in the different materials. This is verified by using a modified version of the *IVCHAR* program, which solves the Poisson equation and can calculate the tip-sample distance for a given material. To a certain degree, the electronic contrast in the STM measurements is well predicted by our calculations, but some discrepancies remain due to the incompleteness of

the used model and the fact that the investigated structure was located inside a p-i-n junction. Nevertheless, the electronic contrast can be suppressed effectively by using high tunnel voltages, preferable in the filled state imaging mode. It is thus possible to obtain STM images showing only the real strain induced outward relaxation.

If the indium concentration inside an InGaAs quantum well is not too high (< 20%), it is possible to determine the indium concentration by simply counting indium atoms. This can be done by measuring in the empty state imaging mode, in which only the group III elements (indium and gallium) are imaged.

By using the theory from section 3.4 it is possible to calculate the indium concentration profile inside the quantum well from the measured lattice constant or outward relaxation profile. The best fit was obtained for an indium concentration of 17.1% which is about 2.7% higher than the values found by counting indium atoms in STM images, XRD and PL. Nevertheless the used approach can be used to determine concentration profiles from STM relaxation measurements with satisfactory accuracy, as the discrepancies, for the major part, can be explained from effects that are well understood.

References

[1]   B. Grandidier, Y.M. Niquet, B. Legrand, J.P. Nys, C. Priester and D. Stiévenard, Phys. Rev. Lett. **85** (5), 1068 (2000)

        H. Eisele, O. Flebbe, T. Kalka and M. Dähne-Prietsch, Surf. Interface Anal. **27**, 537 (1999)

        O. Flebbe, H. Eisele, T. Kalka, F. Heinrichsdorff, A. Krost, D. Bimberg and M. Dähne-Prietsch, J. Vac. Sci. Technol. B **17**, 1629 (1999)

[2]   R.M. Feenstra, V. Ramachandran and H. Chen, Appl. Phys. A **72**, S193 (2001).

[3]   R.M. Feenstra, Semicond. Sci. Technol. **9**, 2157 (1994)

[4]   H.W.M. Salemink, M.B. Johnson and O. Albrektsen, J. Vac. Sci. Technol. B **12**, 362 (1994)

[5]   R.M. Feenstra and J.A. Stroscio, J. Vac. Sci. Technol. B **5**, 923 (1987).

[6]   Ph. Ebert, B. Engels, P. Richard, K. Schroeder, S. Blügel, C. Domke, M. Heinrich and K. Urban, Phys. Rev. Lett. **77** (14), 2997 (1996)

[7]   Sadao Adachi, *Physical properties of III-V semiconductor compounds: InP, InAs, GaAs, GaP, InGaAs, and InGaAsP*, New York : Wiley-Interscience (1992)

[8]   D.M. Bruls, P.M. Koenraad, M. Hopkinson, J.H. Wolter and H.W.M. Salemink, Appl. Surf. Scien. **190**, 258 (2002)

[9]   C.G. van de Walle, Phys. Rev. B **39** (3), 1871 (1989)

[10]   R.M. Feenstra, J.A. Stroscio, J. Tersoff and A.P. Fein, Phys. Rev. Lett. **58** (12), 1192 (1987)

[11]   J.H. Davies, D.M. Bruls, J.W.A.M. Vugs and P.M. Koenraad, Journ. of Appl. Phys. **91** (7), 4171 (2002)

[12]   W. Mönch, *Semiconductor Surfaces and Interfaces*, 3rd ed., Chapter 7 (Springer, Heidelberg, 2001)

Chapter 6

InGaAsN layers and quantum dot formation upon annealing processes

6.1   Introduction

The concept of using semiconductor quantum dots for laser applications is already known for over a decade now [1]. The main advantage of the use of quantum dots lies in the suppression of the temperature dependence of the threshold current, i.e. the minimal amount of current that has to be passed through the laser structure until lasing occurs. Furthermore, enhanced differential gain, high spectral purity and long operation lifetime are attributed to these laser structures.
In modern telecommunications, the demand for cheap and stable high performance laser diodes is very high. The desired wavelengths of these lasers lie between 1.3 and 1.55 μm, as these wavelengths are within the windows of minimal attenuation of the commonly used glass-fibers in optical networks. Diluted alloys containing nitrogen, which can be lattice matched grown to GaAs or InP, recently received considerable attention. This interest is mainly boosted by the development of the low-cost, high performance GaAs-based Vertical Cavity Surface Emitting Laser (VCSEL) [2-5] and the possibility to fabricate more efficient solar cells. Due to the large difference in atomic size between nitrogen, indium, gallium and arsenic, already very small amounts of nitrogen (0.5-2%) cause a large reduction of the bandgap, which is favorable for optoelectronic applications and optical integration. These diluted alloys, however, are difficult to grow, as the amount of nitrogen that is incorporated is generally low (< 2%) and hard to control [5-7].
The improvement in the lasing performance of QD laser structures lies in two effects: quantum effects and bulk effects [8]. The quantum effects, caused by the 3D confinement of the electrons, influence the dynamic properties, like the modulation dynamics and the spectral linewidth of the laser structures in a positive way. In reducing the threshold current, however, also non-quantum effects play a prominent role, as the threshold current is given by:

$$I_{th} = \frac{eVn_{th}}{\tau} \qquad (6.1)$$

where, e is the electron charge, V the volume of the active area, n_{th} the carrier density and τ the carrier lifetime, respectively. Even in the absence of quantum effects, the threshold current can be reduced by making the active volume as small as possible, i.e. making the lateral dimensions of the active area as small as possible.

The localization of carriers, which is a non-quantum effect, also plays an important role. The localization of carriers restrains them from being trapped at dislocations. This leads to a suppression of the effects of non-radiative recombination of carriers on the total carrier recombination time τ, resulting in an increase of the carrier lifetime τ. It is believed that quantum dot-like behavior can already be caused by nanometer scale fluctuations of the indium composition, which are caused by phase separation in InGaAsN quantum wells. This may be useful to suppress nonradiative recombination processes.

However, quantum effects play an important role as the threshold current increases if the ratio of the effective mass of holes m_v and electrons m_e (m_v/m_e) increases, as this is proportional to the carrier density. In GaN-based semiconductors this ratio is unfortunately lager than in GaAs-based semiconductors [9]. On the other hand, however, if quantum dots are used in the active region, the threshold current of GaAs and GaN-based laser diodes becomes almost the same, if the size of these quantum dots is small enough. In that case the effects of higher subbands in GaN-based semiconductors are negligible [10]. Therefore, with the use of GaN based quantum dots, the threshold current can be enhanced by a factor of 100 compared to GaAs-based lasers. Thus the impact of using quantum dots in GaN-based systems is much larger than in GaAs-based quantum dot structures.

It is possible to fabricate quantum dots in systems containing nitrogen by using Chemical Beam Epitaxy (CBE), Molecular Beam Epitaxy (MBE) or Metal Oxide Chemical Vapor Deposition (MOCVD). Different kind of dots can be obtained like: (1) 3D quantum dots obtained by Stranski-Krastanov (with a wetting layer) or Volmer-Weber growth (without wetting layer) in the InAs-GaAs material system (2) 2D shaped quantum dots formed by sub-monolayer insertion in InAs-GaAs and similar systems or (3) quantum dots formed on corrugated or pre-patterned surfaces [8,9,11-14]. We, however, used the procedure as proposed in [15] i.e. annealing InGaAsN quantum well layers by Rapid Thermal Annealing (RTA). We investigated if this post-growth treatment leads to atomic rearrangements causing the formation of quantum-dot-like structures, as was proposed from X-ray Diffraction (XRD) and photoluminescence (PL) measurements performed on similar RTA treated samples [15].

6.2   The structure

The structure we investigated was similar to the structures that were previously investigated by M. Buda *et al.* [15]. Those structures were undoped to facilitate the optical characterization of these samples, as dopants introduce extra donor- and acceptor energy levels and a Fermi-energy-shift leading to a decrease of the PL signal, PL peak broadening, Fermi-tails in the spectrum and peak shifts. The STM-samples, however, were grown on doped substrates to enable tunneling. The samples were grown in a CBE system on a doped (100) InP substrate, and contained 5 sequences of 4 nm InGaAsN and InGaAs quantum wells (QWs), see Table 6.1. The indium concentration in the InGaAs layers was chosen in such a way that the InGaAs layers would be lattice matched to the InP substrate. Assuming

that the indium content in all layers is the same, the influence of the nitrogen in the layers could be investigated, as well as the influence of the RTA treatment.

Material	Thickness		Growth Temperature
InP	1000 Å		515°C
InP	**600 Å**		515°C
In$_{0.54}$Ga$_{0.46}$As$_{0.99}$N$_{0.01}$	**40 Å**	**5x**	515°C
InP	**600 Å**		515°C
In$_{0.54}$Ga$_{0.46}$As	**40 Å**		515°C
InP	1000 Å		515°C
InP substrate n-type Si 1.2.10^{18}			

Table 6.1: *Growth menu of the InGaAsN/InGaAs QW sequence*

6.3   Comparison of the InGaAs/InGaAsN layers: annealing effects

In order to investigate the influence of the addition of nitrogen in the InGaAs layers, both layers containing nitrogen and layers without any nitrogen were examined, see Figs. 6.1 and 6.2. As can be seen in Fig. 6.1 the quality of the InGaAs layers is excellent, as the interfaces are very sharp and no vacancies or other defects are visible. A small amount of arsenic segregation in the growth direction is observed which is rather common in these structures and is often observed in STM [16]. Although the tunnel parameters were chosen to suppress the electronic contrast, the cleaved lattice matched layers still show an outward relaxation. This is probably due to a small error in the indium deposition rate during CBE, resulting in an increased indium concentration, and thus strained InGaAs layers.

In Fig. 6.2 an as-grown InGaAsN layer is shown. The dark features, located at the left side of the InGaAsN quantum well, are attributed to the nitrogen incorporated in the layer. It seems that the nitrogen is not equally distributed over the layer, but it seems more or less to "float" on top of the InGaAs layer. This might be due to the switching behavior of the CBE, or due to strain-driven segregation of the nitrogen. By counting the dark features, it is possible to estimate the amount of nitrogen that is incorporated in the structure. We find a nitrogen concentration of about $1.2 \pm 0.3\%$, which is in agreement with the growth menu that indicates a nitrogen content of 1%.

In Fig. 6.3 a zoom of the dark features, which we attribute to the nitrogen, atoms is shown. Both single as well as double dark sites can be distinguished. The single-sites have a depth of approximately 25 pm whereas the double-sites have a depth of about 50 pm with respect to the surrounding InGaAs. As the nitrogen atom is very small, it leads to a strain reduction in the strained InGaAsN layers, so it is to be expected that the double-site features have indeed a larger depth than the single-site ones if they are caused by nitrogen atoms.
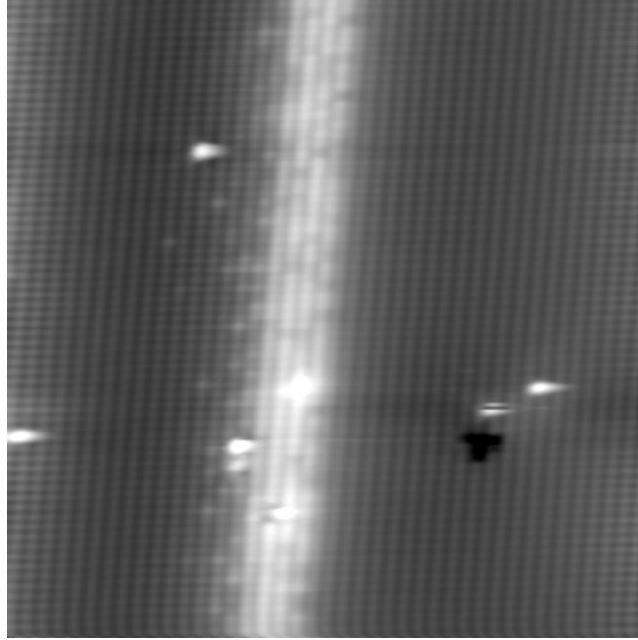
Fig. 6.1: *As-grown InGaAs layer in the InP matrix. V_{tunnel} = -3.000 V. Image size 25x25 nm^2. No vacancies or defects are observed in the layer. The substrate is located at the right hand side of the image, so the growth direction is therefore from the right to the left*
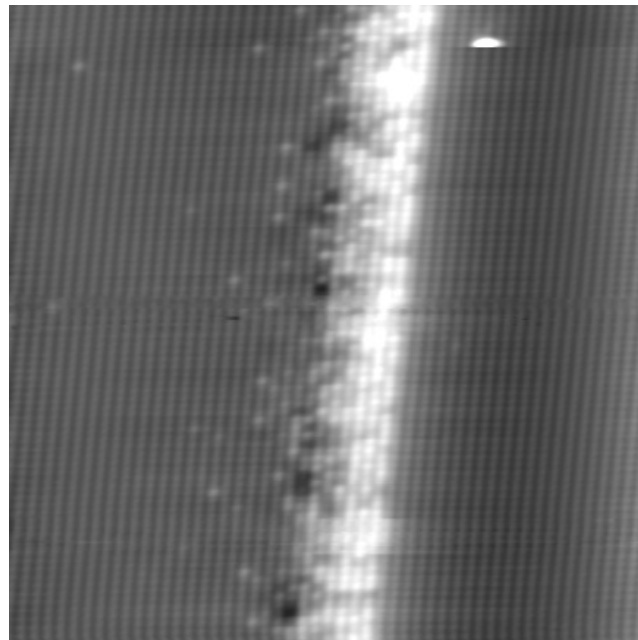

Fig. 6.2: *As-grown InGaAsN layer. The substrate is located at the right hand side. The growth direction is from the right to the left. Image size 30x30 nm^2, V_{tunnel} = -3.000 V*
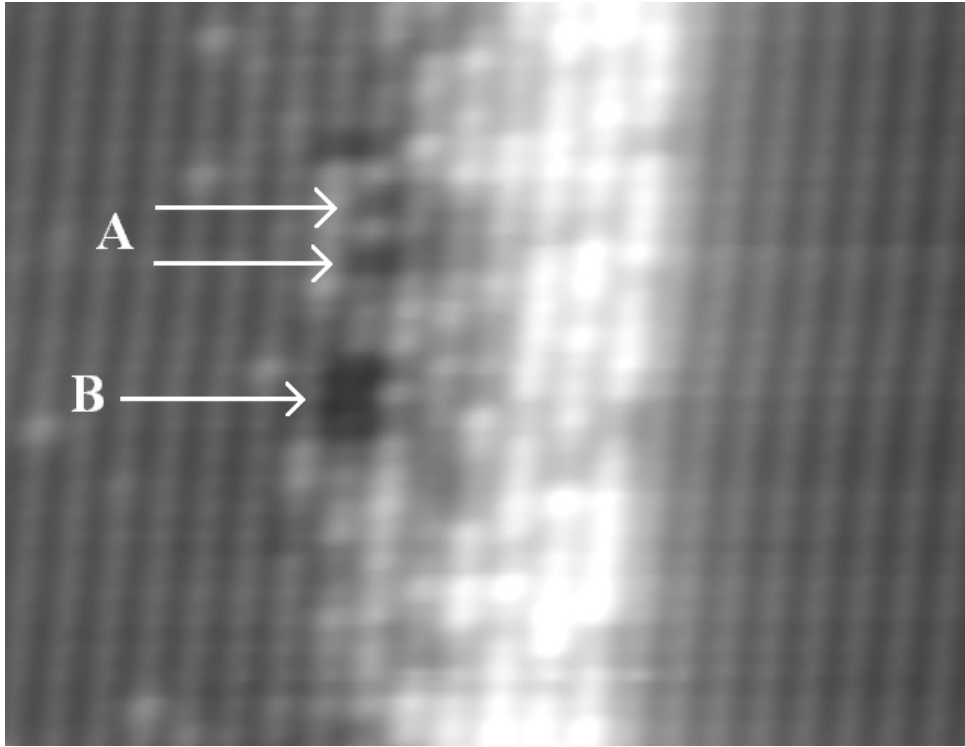
Fig. 6.3: *Zoom on the as-grown InGaAsN layer. Both single (A) as double (B) nitrogen sites can be distinguished. The double-sites have a twice as big depth than the single sites. Image size 13x10 nm²*

As the pure InGaAs layers did not show any vacancies at all, the existence of vacancies in the InGaAsN layers is very unlikely, as all parameters, with exception of the addition of the nitrogen, were the same for all layers. The possibility that the dark single- and double-site features would be vacancies can therefore be ruled out. The existence of double-side features is hardly surprising, as it is easy for the free radical N atoms, which are created in the high temperature cracker in the CBE machine, to form the very stable N_2 that is incorporated in the structure during CBE growth.
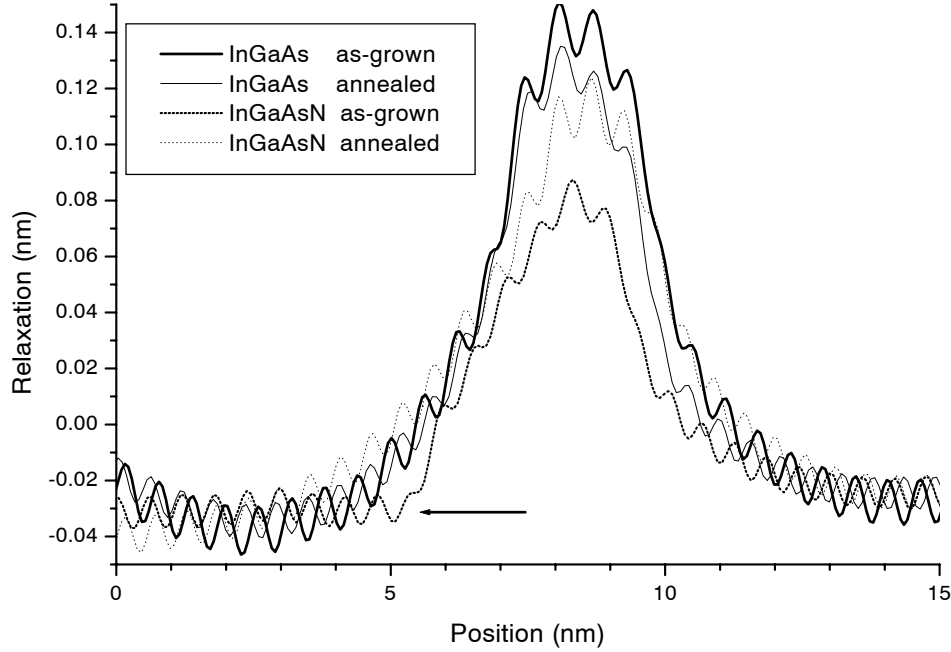
Fig. 6.4: *Relaxation profiles of the InGaAs and InGaAsN quantum wells both for the annealed as the "as-grown" case. The profiles are obtained by averaging 50-100 line profiles. The growth direction runs from right to left. In the as-grown InGaAsN profile a small depression (indicated by the arrow) at the left hand side is visible, caused by the nitrogen rich region in the upper part of the layer, as also can be seen in Fig. 6.2*

If we look at the relaxation profiles of both the as-grown InGaAs and InGaAsN layers, see Fig. 6.4, it becomes immediately clear that the outward relaxation of the as-grown layers that contain nitrogen, is much smaller than of the layers without any nitrogen, although the indium and gallium contents of these layers are identical. This again proofs the incorporation of nitrogen, as it reduces the compressive strain in an InGaAs layer in an InP matrix, resulting in a lower outward relaxation upon cleavage than an InGaAs layer without nitrogen. Because the line profiles from Fig. 6.4 were obtained at high tunnel voltages (> 3V) in the filled state mode, only the real topography is imaged, as has been discussed in the previous chapter and we did not suffer from any electronic contrast influencing the imaged topography anymore. In order to check this, again, the apparent outward relaxation of the cleaved layers has been determined as function of applied bias, as is shown in Fig 6.5. As we have suppressed the electronic contrast successfully, the reduction in outward relaxation can therefore only be caused by the nitrogen in the InGaAsN layers, as was to be expected from the small size of the nitrogen atoms [14,15].

Next, the sample had been annealed by RTA at $600^{\circ}C$ for 5 minutes under a nitrogen atmosphere. During the RTA treatment the sample was capped with an InP substrate wafer to prevent the evaporation of phosphor out of the sample. However, while heating the sample, an overshoot in annealing temperature occurred, resulting in an increased annealing temperature during 30 seconds of about $630^{\circ}C$. After the annealing process, both the

InGaAs and InGaAsN layers were investigated again in the X-STM. In the InGaAs layers no changes at all occurred. The layer quality remained the same and the relaxation profiles showed hardly any change, see Fig. 6.4. In the InGaAsN layers, however, a stunning change did take place. All dark features, as shown in Fig. 6.3, seemed to have disappeared. Also the relaxation profile of the annealed InGaAsN layer changed drastically, as the relaxation increased by almost 40 pm with respect to the as-grown InGaAsN layers, see Fig. 6.4. It therefore seemed that the nitrogen had disappeared out of the layer and a plain InGaAs layer had been formed. Closer investigation of the layer revealed the existence of large depressions inside the former InGaAsN layer, as is shown in Fig. 6.6. Therefore the formation of nitride dots upon heat treatment has been demonstrated, as already was suspected from the optical investigation of similar RTA treated structures [15]. As the total amount of indium inside the layer was very limited, the dot density was, as expected, very low, and was estimated to be about 10^8-10^9/cm^2 whereas the rest of the InGaAsN layer had lost a considerable amount of nitrogen.
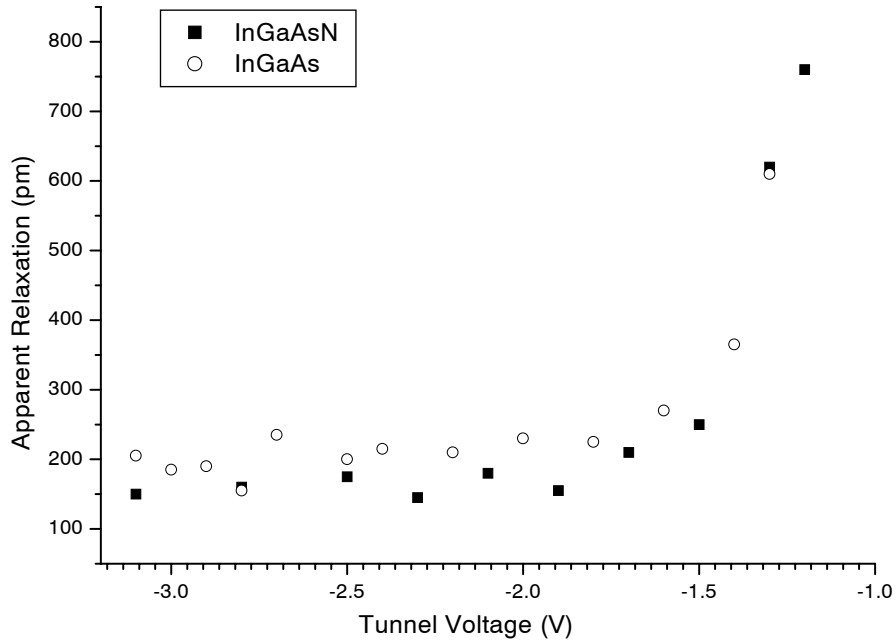
Fig. 6.5: *Apparent outward relaxation height of both the InGaAs and InGaAsN layers as function of applied tunnel bias in the filled state imaging mode. At large voltages (> 3V) the electronic contrast is completely suppressed*

In order to form these nitride dots, lateral segregation of the nitrogen atoms must have occurred, rather than segregation of the nitrogen out of the layers. This can be understood in terms of strain and energy minimalization. The InGaAs layers are strained inside the InP

matrix, due to the indium concentration overshoot during CBE growth. Adding the nitrogen in these layers during growth reduces strain as the lattice mismatch between the InGaAs layers and the InP matrix is reduced, thus facilitating growth. If, however, the nitrogen had segregated into the InP matrix during annealing, two energetically unfavorable processes would occur: not only the total strain in the InGaAs layers would increase, as the lattice constant would increase further with respect to the InP matrix, but also the lattice constant of the nitrogen incorporated InP would decrease, leading to extra strain of this InP with respect to the nitrogen free InP matrix and the extra strained nitrogen free InGaAs layers. The dot formation leads thus to a local strain minimization, as the InGaAs containing this high nitrogen concentration (i.e. the quantum dot) is locally less mismatched to the lattice constant of the InP matrix. Furthermore, phase-separation processes may already play an important role at the used annealing temperatures [12,17].
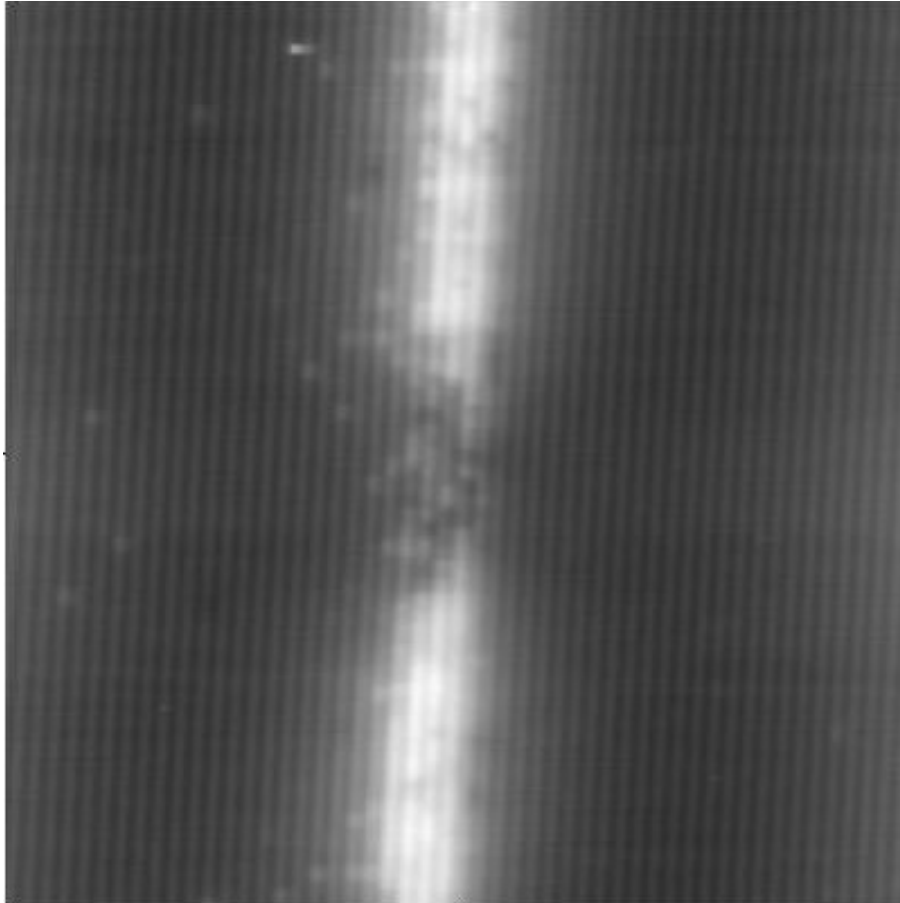

Fig. 6.6: *Annealed InGaAsN layer. The sample was annealed by RTA for 5 minutes at $600^{o}C$ under a nitrogen atmosphere. Nitrogen dots have formed and the dark features, as seen in Fig. 5.3, have disappeared. The dot density is estimated to be 10^{8}-10^{9}/cm^{2}. Image size 29x29 nm^{2}*

6.4   Thermal damage

In order to investigate if the dot density could be increased, or the dot shape altered, a higher annealing temperature during RTA was applied. During RTA, however, a severe temperature overshoot occurred, causing the annealing temperature to be between 680°C and 690°C for about 30 seconds instead of the intended constant temperature of 650°C. Nevertheless this sample was investigated in the X-STM setup to see the effects of this increased annealing temperature.

In Fig. 6.7 the InGaAs layer is indicated. Small dark features inside the layer are visible now. The depth of these features is about 35 pm, and is more or less the same for single, double and even triple site features. Therefore these features can be attributed to vacancies that have been formed inside the layer due to indium segregation and/or arsenic evaporation. The evaporation of phosphor was suppressed as the wafer was covered with an InP wafer, but due to the extreme high temperature during the overshoot of the RTA temperature some phosphor could have been evaporated.

Also the interfaces of the layer are not straight anymore. Both on the top as in the bottom of the layer considerable roughness is visible now. Also the interface moves up-and-down, i.e. at the bottom of the layer atomic rows stop to exist at certain points, whereas at the top of the layer new layers are formed. The whole InGaAs has thus moved up-and-down throughout the whole structure, resulting in "wavy" interfaces. No preferential segregation direction is observed, which is to be expected as during RTA the temperature difference between the top and the bottom of the wafer is maximal a few degrees Celsius.

In Fig. 6.8 an example of an over-annealed InGaAsN layer is shown. For this layer the same applies as for the InGaAs layer: wavy interfaces and introduction of defects. Furthermore, no quantum dots were to be found. It is known from literature that annealing of InAs quantum dot structures may cause the dots to dissolve upon annealing [18]. The nitride, however, still seems to be present.

All 10 over-annealed InGaAs/InGaAsN layers were investigated. The variation in the layers was very large, as sometimes by only looking at the nominal growth thickness of the layers, the layers could not be identified as containing nitrogen or not. There were thick InGaAsN layers that looked almost like an InGaAs layer as no nitrogen could be detected anymore, but also InGaAs layers that looked like a narrow InGaAsN layer were observed, as nitrogen -like features could be distinguished. The largest changes were visible in the InGaAsN layers however. All these changes/errors were not present in the as-grown samples or in the 600°C-annealed samples.

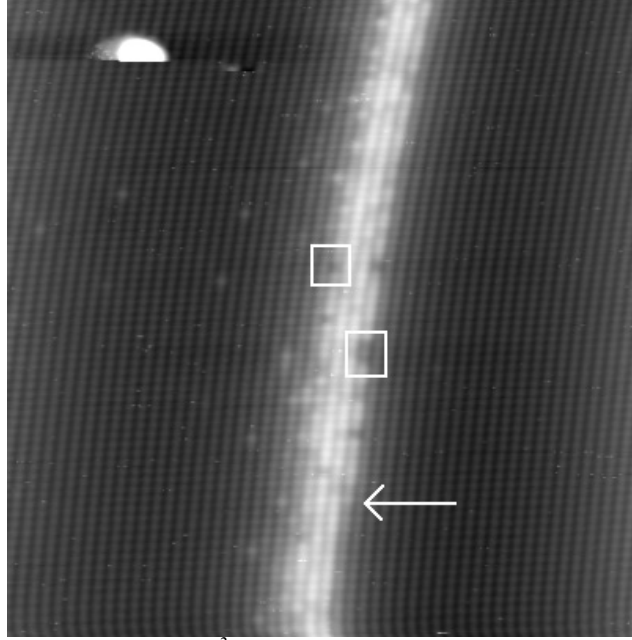**Fig. 6.7:** *InGaAs layer 30x30 nm^2, annealed at 650°C, showing thermal damage, like vacancies (squares) and interface roughness (arrow). The growth direction is from right to left. V_{tunnel} = -3.000 V*

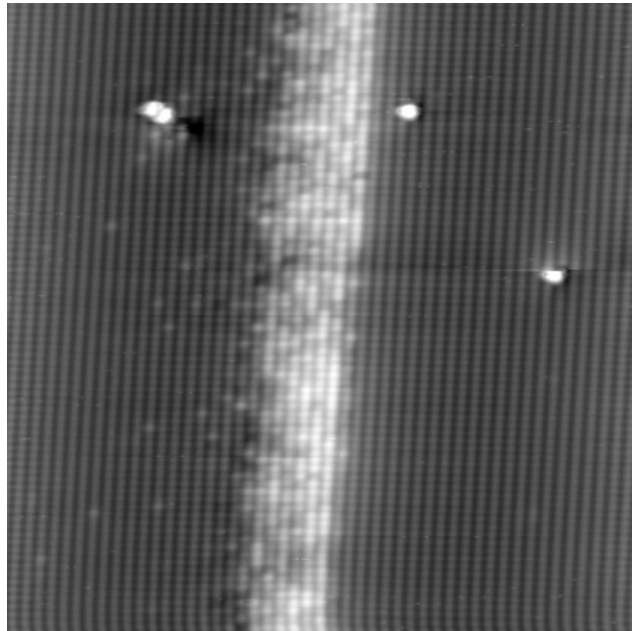**Fig. 6.8:** *An example of an InGaAsN layer 30x30 nm^2, annealed at 650°C, showing thermal damage. The growth direction is from right to left. V_{tunnel} = -2.000 V*

6.5 Conclusions

Diluted alloys containing nitrogen are very promising for novel high quality optoelectronic applications and integration, although they are still difficult to grow. By CBE it is possible to obtain a nitrogen incorporation of about 1.2% in InGaAsN layers within an InP matrix. In STM both single and double-site features, that are attributed to atomic and molecular nitrogen, are observed. The nitrogen is concentrated at the top of the InGaAsN layers, which may be due to the switching behavior of the CBE machine and the growth characteristics.

Annealing of the InGaAs layers leads to dot formation, as was suspected from earlier studies [15]. Investigation of relaxation profiles of both annealed and as-grown InGaAs and InGaAsN layers shows that during annealing the nitrogen forms dots. The remaining "wetting layer" is a plain InGaAs layer containing almost no nitrogen. This is caused by lateral segregation, which is due to local strain-reduction and phase-separation. If the annealing temperature is too high, all layers, including the InGaAs layers, show vacancies and severe interface roughness, making the structure useless as even the layers that should have the same composition vary substantially from each other.

References

[1]   Y. Arakawa and H. Sakaki, Appl. Phys. Lett. **40**, 939 (1982)

[2]   M. Kondow *et al.*, Jpn. J. Appl. Phys., Part 1 **35**, 1273 (1996)

[3]   J.A. Lott *et al.*, Electron. Lett. **36,** 1384 (2000)

[4]   K.D. Choquette *et al.*, Electron. Lett. **36**, 1388 (2000)

[5]   T. Miyamoto *et al.*, Journ. of Cryst. Growth **209**, 339 (2000)

[6]   J.C. Harmand *et al.*, Appl. Phys. Lett. **77** (16), 2482 (2000)

[7]   Wei Li *et al.*, Appl. Phys. Lett. **78** (19), 2864 (2001)

[8]   A. Yu. Egorov *et al.*, Phys. Stat. Sol. B **224**, no.3, 839-843 (2001)

[9]   Y. Arakawa, T. Someya, and K. Tachibana, Phys. Stat. Sol. B **224**, no.1 (2001)

[10]   T. Saito and Y. Arakawa, Phys. Rev. B **60** (3), 1701 (1999)

[11]   N.N. Ledentsov *et al.*, Jpn. J. Appl. Phys. **41**, 949 (2002)

[12]   A.M. Mitairov *et al.*, Phys. Rev. Lett. **87** (27), 277401 (2001)

[13]   S. Makino *et al.*, Jpn. J. Appl. Phys. **41**, 953 (2002)

[14]   B.V. Volovik *et al.*, Semicond. Sci. Technol. **16**, 186-190 (2001)

[15]   M. Buda *et al.*, Proc. Int. Workshop on Nitride Semiconductors, IPAP Conf. Series 1, pp. 433-436

[16]   Edward.T.Yu, Chem. Rev. **97** (4), 1017 (1997)

[17]   T. Mano *et al.*, Journ. of Crystal Growth **209**, 504 (2000)

[18]   S.J. Xu *et al.*, Appl. Phys. Lett. **72** (25), 3335 (1998)

Chapter 7

Determination of the properties of InAs quantum dots and their wetting layers

7.1 Introduction

Currently there is a strong interest in the shape and composition of self-assembled quantum dots (SQDs), properties which are very difficult to determine and often only available by indirect means with very low accuracy. Precise knowledge of the shape and composition of these dots, on which optical and electrical properties depend [1-8], is of major interest, as the electron and hole wavefunctions and the position of these wavefunctions with respect to the dot position are strongly dependent on the shape and composition. InAs quantum dots in a GaAs matrix, grown by Molecular Beam Epitaxy (MBE) in the Stranski-Krastanov (SK) growth mode, are of particular interest. Although it is possible to investigate these quantum dots at the growth surface using atomic force microscopy (AFM) [9,10], the dot shape and thus the electronic properties, can change significantly after coverage with a capping layer. In general TEM and HREM measurements of covered quantum dot samples lack sufficient contrast between the dots and the surrounding GaAs matrix, in order to obtain conclusive information about the shape and composition of these buried dots at the atomic level [1,11-15]. Furthermore these methods suffer from averaging effects, which hamper the investigation of e.g. interface roughness and alloy fluctuations. By using X-STM a conclusive, comprehensive determination of the shape, size and composition of SQDs is possible now.

7.2 Shapes in literature and the effect of capping

Various models for the shape and orientation of quantum dots are proposed in literature [14,16-18]. It is also reported that the shape strongly depends on the growth parameters during MBE, making it very difficult to predict the shape of the dots in advance, or compare dots that were produced under different growth conditions.
By treating the quantum dot formation during Stranski-Krastanov MBE growth theoretically, Shchukin et al. [19] made morphology statements based on minimum energy calculations. It was found that there exist an optimum shape, size, orientation and distribution of 3D islands on a (100) surface. This distribution corresponds to a 2D periodic lattice of equally sized islands with a pyramid-like shape with a square base. The

primitive lattice vectors, along which the dots are oriented, are along the [100] and [010] directions, if the growth direction is defined as the [001] direction. This dot distribution is formed due to the cubic anisotropy of the elastic moduli of the InAs and GaAs. Some more elaborate simulations of the shape of an individual quantum dot, including surface and edge energies [20], resulted in an equilibrium quantum dot shape of that of a truncated pyramid with an octagonally shaped base. In Fig. 7.1 some possible dot shapes are indicated, with planes following the crystallographic planes.
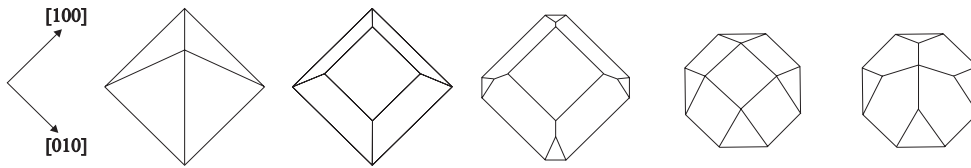

Fig. 7.1*: Some possible dot shapes, bounded by crystallographic planes*

Experimentally, plan-view and cross-sectional Transmission Electron Microscopy experiments [12,21,22] on covered and uncovered dot samples also revealed that the dots were square based with a preferential orientation and distribution along the [100] and [010] directions. X-ray scattering [23] and cross-sectional STM experiments [16,23] suggest the presence of facet families of {101} and additionally {111}. This again would imply square or octagonally based pyramids.

Experiments on uncovered dots indicated pyramidal shaped dots [3,21]. However, X-STM images of capped dots indicate lens-, disk- or truncated pyramidal shaped dots [16,24], which is to be expected as the dot shape can change significantly upon capping [12], making it impossible to make a comparison between the two of them.

Different techniques have been used to investigate the geometry of SK-grown quantum dots, but not all data points to one particular shape. This indicates the importance of the growth parameters. It is known that different growth temperature and -speed, the use of growth interrupts and the III/V ratio affect the morphological and electrical properties of the quantum dots significantly [15,25-29]. Moreover, although pure InAs is deposited during SK-growth, there is evidence for alloying [3,30] and even different non-uniform composition profiles are proposed [1,31]. Finally, very little is known of what happens during overgrowth. Most of previous experimental results were obtained during experiments on uncapped dots while intermixing and shape changes may occur during overgrowth [12,32].

In conclusion, it is not exactly clear what **the** shape of **the** quantum dot is. Apart from the fact that there is lack of strong evidence for any particular dot shape, there is actually no such thing as a "universal" dot shape, as it depends too strongly on the exact growth conditions. It is however possible to determine the dot shape by X-STM and from these measurements we try to explain and understand the processes which have occurred during growth afterwards, to get a feeling which growth parameters are the most crucial ones.

Most calculations on the electronic properties of the quantum dots do assume a pyramidal shape. Partly this is because of simplification, partly because of the first theoretical and experimental indications. As far as known, the only experimental evidence for pyramidal dots is on uncovered samples.

7.3 Investigation of low growth rate InAs quantum dots

7.3.1 Sample #1 (M1640 Sheffield)

The first quantum dot sample contained Stranski-Krastanov (SK) grown InAs islands. The sample was grown by M. Hopkinson (Department of Electronic & Electrical Engineering at the University of Sheffield UK) in a similar way to the sample from which photocurrent results were obtained by Fry *et al*. [1] and was provided by the Department of Physics at the University of Sheffield UK.

The sample was grown by Molecular Beam Epitaxy (MBE) on a (100) GaAs substrate at 512°C. It consisted of five uncoupled, SK-grown, InAs quantum dot layers, embedded in a GaAs matrix (see Table 7.1). Per layer 2.4 monolayers of InAs were deposited. The growth speed was 0.01 monolayers per second, which is extremely low, and the island density was about $1.5*10^9$ cm^{-2}. The SK-grown layers were embedded within the intrinsic region of a p-i-n-junction designed for photocurrent measurements as a function of applied bias [1]. The X-STM measurements show that the dot layers are un-coupled, which is to be expected, as the spacing between the quantum dot layers was 50 nm.

Repeats	Thickness [Å]	Material	Temp. [°C]	dopant	type	Conc. (cm^{-3})
1	3000	GaAs		Be	p	$2.0*10^{18}$
1	1500	GaAs			nid	
4	500	GaAs	516		nid	
5	7	InAs 2.4 ML	511		nid	
1	1500	GaAs	583		nid	
1	3000	GaAs	585	Si	n	$2.0*10^{18}$
Substrate		GaAs (100)		Si	(n$^+$)	

Table 7.1: *Growth menu quantum dot structure #1. InAs growth rate was 0.01 ML/s*

A number of individual quantum dots were investigated by X-STM using the constant current mode. Both the topography and current image of the cleaved InAs quantum dots were recorded, see Fig. 7.2. The current image shows contrast because the feedback loop is never fast enough to adjust the tip-sample distance instantly, resulting in changes in the current signal, which are proportional to the spatial derivative of the topography image. In these current images the atomic corrugation and contrast are very pronounced. This enables a more clear distinction between the InAs quantum dot and the surrounding GaAs matrix, thus facilitating the determination of the size and shape of the dots.
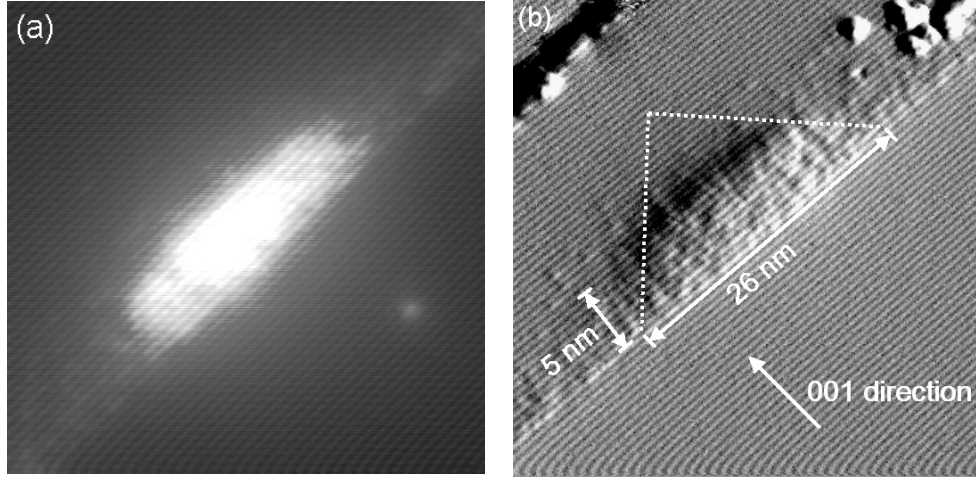
Fig. 7.2: *(a) 30x30 nm² X-STM topography image of a cleaved quantum dot. As it is difficult to determine the exact boundaries of the dot from these topography images, they are not fit for the determination of the shape and dimensions of the dots (b) 40x40 nm² X-STM current image of a cleaved InAs quantum dot and the wetting layer. There is a clear contrast between the dot, the wetting layer and the surrounding GaAs matrix. In the upper right corner some cleavage debris is visible*

7.3.2   Shape and indium profile according to photocurrent measurements

The photocurrent measurements on this sample (also called Stark-effect spectroscopy measurement), provided by Fry *et al.*[1] showed a permanent dipole. This dipole exists because the confined electrons in the dot are spatially separated from the holes. The conduction and valence band potential are such that holes are confined in the top of the dot and the electrons more at the dot base. The bandgap and band line-up that cause this potential depend on the composition and strain distribution in the dot. This makes it possible to make predictions on the shape and composition of the dots, based on these measurements. Barker *et al*. [2] derived that the observed behavior can only occur in a quantum dot that has a truncated shape and an indium composition gradient with increasing indium concentration towards the top of the dot. The average shape and composition of the dots derived by Fry *et al*. [1] is displayed in Fig. 7.3.
The best fit was obtained using a pyramid with a base length of 15.5 nm and a height of 22 nm, of which 75% is truncated to give an actual height of 5.5 nm, and the indium concentration varying from 50% at the base to 100% at the top surface. Later these best-fit parameters were slightly changed by Barker *et al* [2]. Here a truncated pyramid is assumed with a base length of 18 nm decreasing to 14.8 nm at the top of the dot, a dot height of 5.5 nm and a linear indium composition gradient with a value of 60% at the bottom and 100% at the top of the dot.
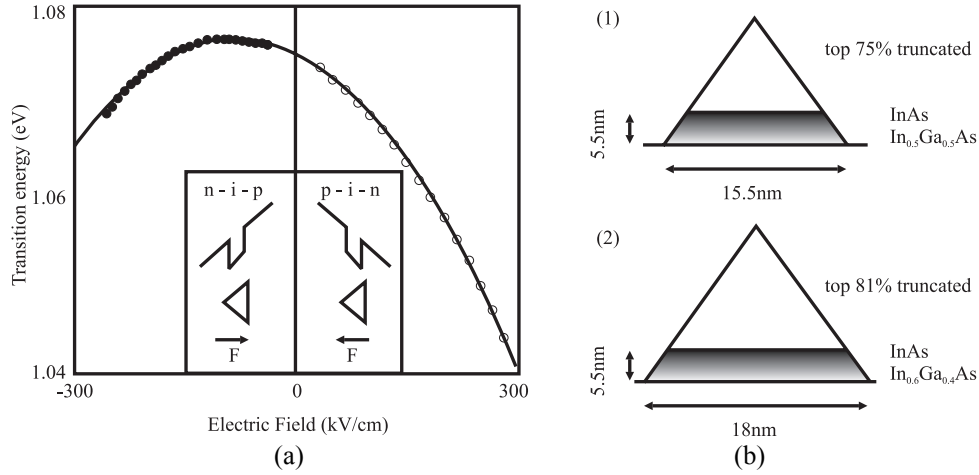
Figure 7.3: (a) *Results of the photocurrent measurements by Fry et al. [1]. There is a permanent dipole in the quantum dots. (b) Modeling the data gives the average shape and composition of the dots [32]. (1) from Fry et al. [1] which was later slightly adjusted [2] resulting in shape and indium profile (2)*

7.3.3 Shape and size analysis

The cross-section of the dot in Fig. 7.2 dot has a height of 5 nm, a diagonal base length of 26 nm and a trapezoidal shape. In addition, part of the wetting layer is clearly visible to the left and right of the quantum dot. Performing measurements on the natural (110) cleavage plane implies that the shape and size found in the cross-sectional images depend on the position of each dot with respect to the cleavage plane and the actual dot-shape.

To determine if the quantum dots have the shape of a full pyramid, or that of a truncated pyramid, 18 dots were investigated and their cross-sectional dimensions measured. Various models for the shape and orientation of dots are proposed in the literature. In Fig. 7.4 we present the models for a full and truncated pyramid quantum dot, and their possible cross-sections with respect to the cleavage plane.
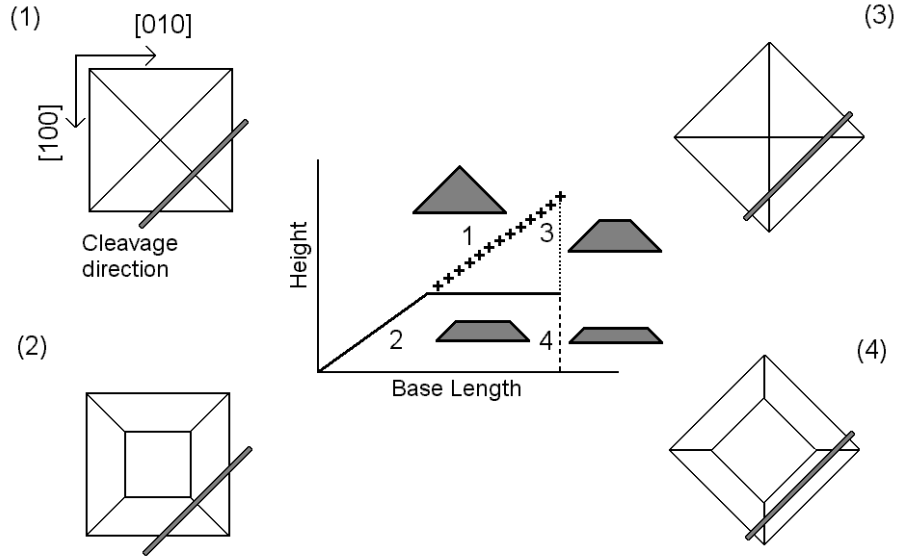
Fig. 7.4: *Four models for the shape and orientation of the quantum dots and their various cross-sections with respect to the cleavage plane*
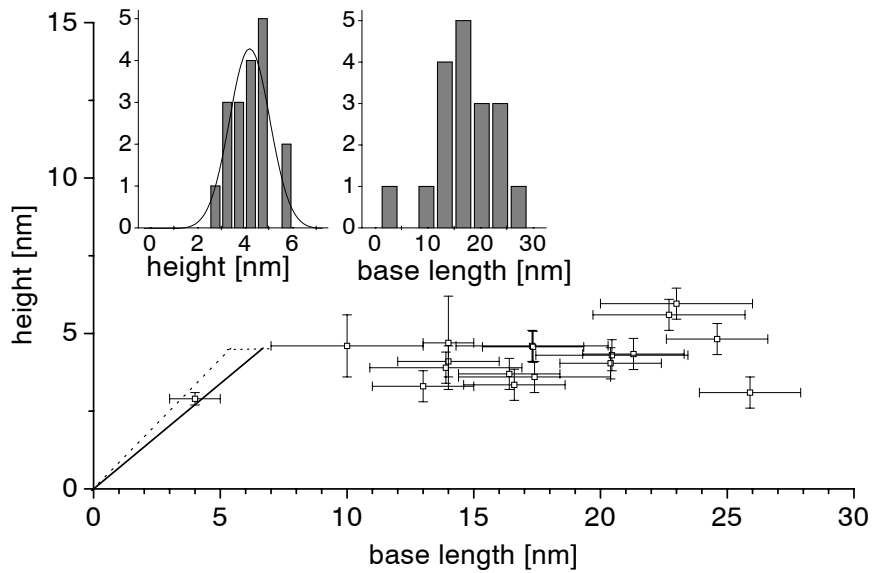

Fig. 7.5: *Height vs. base length distribution of the cross-sectional images of the analyzed quantum dots. The expected distributions for the two possible cross-sections with the {111} (dotted line) and (101} (solid line) facets, forming the sidewalls of the dots, are indicated in the graph.*

The height vs. base length distribution is deduced from our X-STM measurements and plotted in Fig. 7.5. As no triangular shaped cross-sections are observed, model 1 can be excluded. In order for model 3 or 4 to be valid, a fixed base length for the whole range of heights would be expected in all cross-sections, which is clearly not the case. Therefore, for these particular quantum dots model 3 and 4 are also not feasible. In our observations the existence of various base lengths with a generally constant height is in agreement with model nr. 2. Because the number of dots investigated is too small, it is not possible to determine the size distribution of the dots.

The maximum observed base length of 26 nm is the diagonal of the square base, so the actual base length is 18 ± 1 nm. The height of the dots is 5 ± 1 nm. This is in perfect agreement with photocurrent measurements performed previously on a dot sample grown under very similar conditions. Based on extensive theoretical modeling it was concluded that a truncated pyramid with a height of 5.5 nm, a base length of 18 nm and a size distribution of 5% provided a best fit to the experimental observations. Moreover the results of these measurements concluded that an indium gradient must exist in the quantum dots.

In the measured quantum dots, many small short ranged fluctuations are visible (Fig. 7.2) indicating that the dot material is an alloy. The formation of an alloy during growth is well known from STM measurements on uncapped InAs quantum dot structures [3,7].

7.3.4   Relaxation profiles

After cleavage the quantum dot relaxes outwards due to the strain resulting from the large lattice mismatch between InAs and GaAs (7%). This is visible in line-profiles across the dots in topography images (Fig 7.6), which show a clear height contrast between the dot and the surrounding GaAs matrix. The magnitude of this outward relaxation is linked to the local indium concentration inside the quantum dot [16,33].
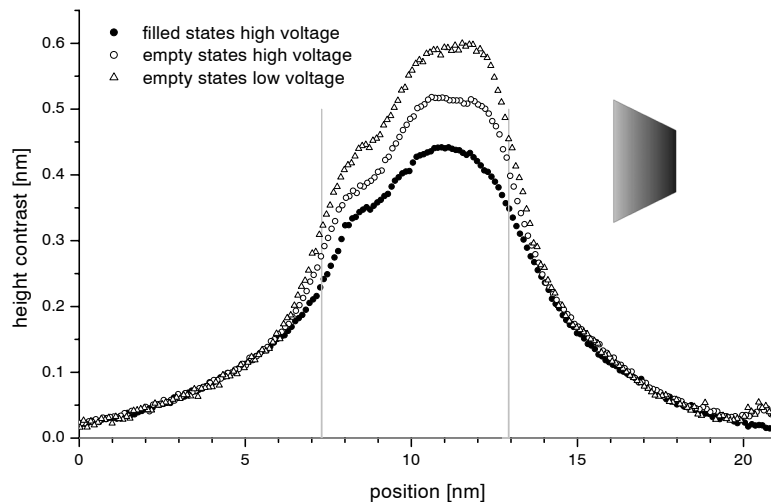

Fig. 7.6: *The observed relaxation profile for a quantum dot for three voltage regimes*

As explained in Chapter 5, the electronic contrast can be suppressed by using high positive tunnel voltages (> 2.5 volt, empty state imaging mode) or negative voltages (filled state imaging mode) during the measurements [34], see Fig 7.6. At high tunnel voltages the relaxation profiles approach a constant value. However, there will be still a difference between the filled and empty states images as different elements are imaged here. This difference in relaxation height between the filled and empty state imaging mode can be explained in the same way as for the cleaved quantum wells as described in chapter 5. It can be seen in Fig. 7.7 that the difference between the filled and empty state relaxation profiles at higher voltages remains larger than in the quantum well case, chapter 5. This is due to the fact that the indium concentration in the quantum dots is much larger than in the quantum well case, resulting in a larger effect due to the larger size and different buckling behavior of the indium atoms.
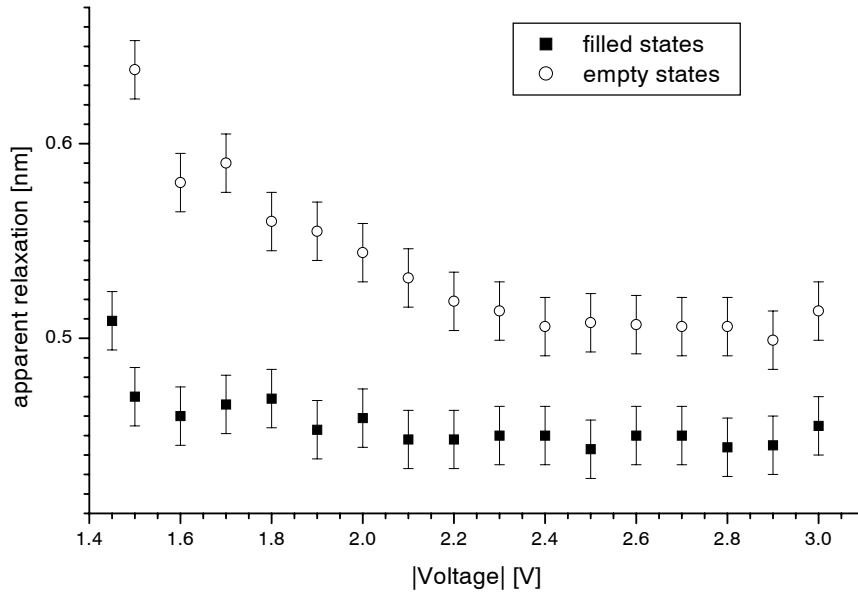

Fig. 7.7: *The apparent outward relaxation of the quantum dot at all measured voltages, $I_{image}=114\ pA$*

7.3.5 Numerical calculation of the relaxation profile and determination of the indium concentration profile

The relaxation has an asymmetric profile and is at its strongest near the top of the dot. Using the finite element calculation package *Abaqus*, which was successfully used for the interpretation of the photocurrent results, Fei Long and S.P. Gill (Department of Engineering Leicester University, UK) calculated the outward relaxation (Fig. 7.8) and lattice constants (Fig. 7.10) for cleaved dots with finite dimensions consisting of pure InAs

or other distributions, like a linear indium gradient. In the calculations, different values for Young's modulus (E_{InAs}= 51.44 GPa, E_{GaAs}= 85.62 GPa) and Poisson's ratio (v_{InAs}= 0.353, v_{GaAs}=0.3177) are assumed in- and outside the dot. Furthermore, the values of these parameters and the strain in the alloy are assumed to be a linear function of the indium concentration. Although some particular shape and composition combinations could result in the same relaxation profile, these calculations, together with the X-STM measurements, can be very effectively used to determine the composition of the dots. The calculations have been performed for various compositions for a dot with the shape of a square based truncated pyramid and have been compared with the experimental results (Fig. 7.8) [35].

The used width of the dot at the bottom is 18 nm and decreases to 10.6 nm at the top of the dot. The dot height is 5.0 nm and sits on a 0.6 nm thick continuous wetting layer and the dot is assumed to be cleaved along its diagonal. In the calculations the following indium profiles are investigated: 1) $In_xGa_{1-x}As$ dots with constant x, 2) dots with a linear indium gradient, 3) dots with a pure inverted pyramidal shaped core with indium profiles as proposed in [31]. By analyzing only dots with a cross-sectional base length that equals the maximum observed value (Fig 7.5), we are sure that the experimental data presented in Figs. 7.8 and 7.9 are indeed obtained from dots that are cleaved along their diagonal. Calculations assuming steeper side facets of the dot, which we do not observe in our X-STM measurements, result in a worse fit. These calculations show that a lower indium concentration indeed results in a lower average outward relaxation and that the investigated dots cannot consist of homogeneous $In_xGa_{1-x}As$ due to the asymmetry in the profile. The calculation assuming a dot in which an indium gradient (60% linear to 100% from bottom to top) is present, yields the best fit to our measurements and is in agreement with [1,2].
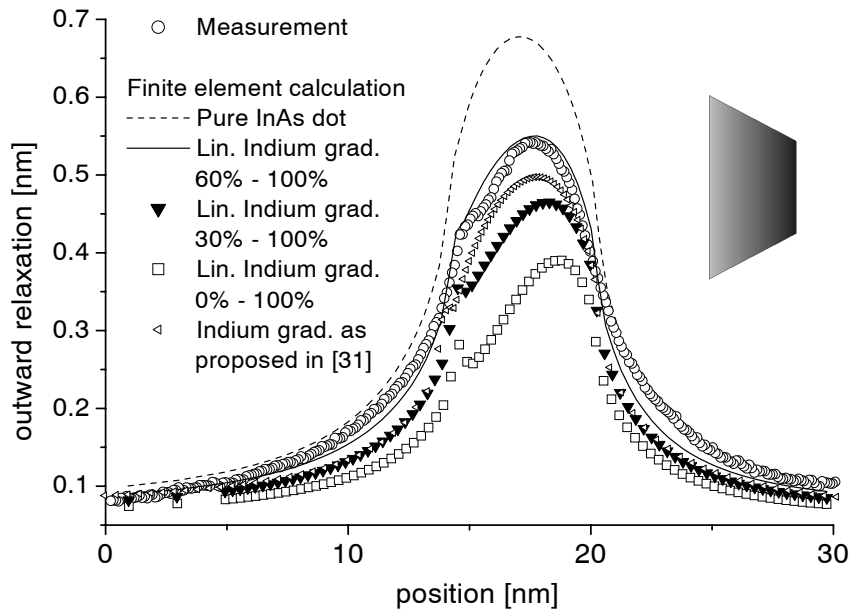

Fig 7.8: *Measured and calculated line profiles across the center of the dot. All indium gradients and the measured profile are plotted from bottom to top*

7.3.6   Strain- and lattice constant profiles

We have determined the change in lattice constant throughout the cleaved dot by taking line-profiles and measuring the spacing between the atomic rows, see Fig. 7.9. We observe an increase in lattice constant of 35 pm going from the bottom to the top of the cleaved dot. This increase can be linked to the indium content in the growth direction [16,33], although in principle a variation of the lattice constant in the dots does not directly imply a gradient in the indium concentration, as the strain distribution in a dot can be very inhomogeneous. A gradient in indium concentration in dots is caused by growth processes such as segregation and strain related indium incorporation [13,33]. Both these mechanisms might be expected to lead to an indium gradient resulting in a higher indium concentration in the top of the dot.
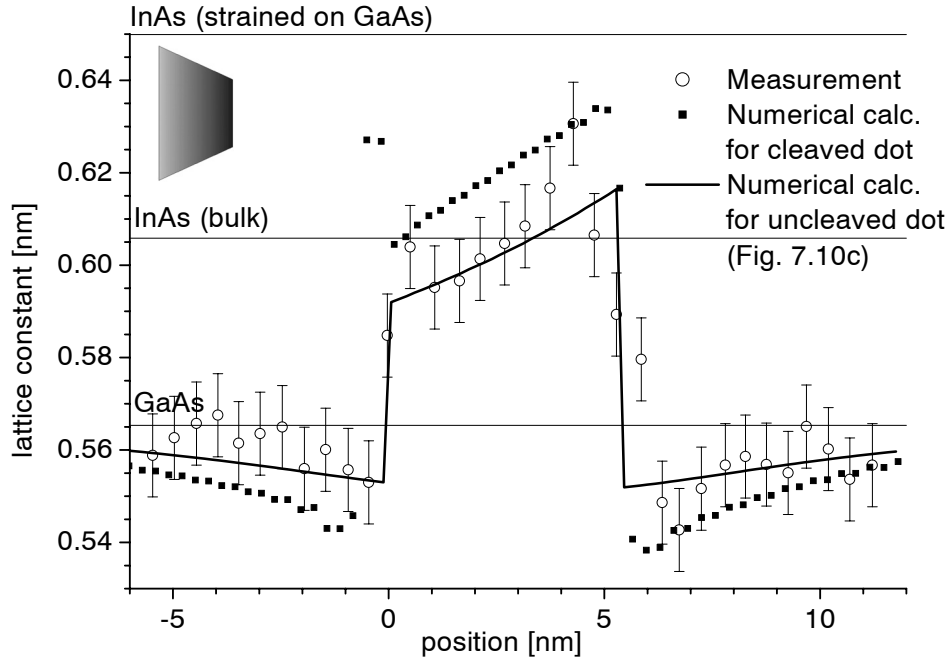
Fig. 7.9: *Average measured lattice constant profile in the growth direction of the quantum dot (circle), compared with the calculated profiles from the photocurrent results (uncleaved surface)(solid line) and numerical simulations (square). The growth direction runs from left to right*

The strain component e_{zz} and the local indium concentration determine the local lattice constant $a_{zz}(z)$ in the growth direction of the dot

$$a_{zz}(z)=(1+e_{zz}(z))a_0(z) \qquad\qquad (7.1)$$

where $a_0(z)$ is the lattice constant determined by the local indium concentration. The strain component in the growth direction e_{zz} (Fig. 7.10) was calculated for different dot shapes and compositions. Profile (a) in Fig. 7.10, which corresponds to a pyramidal dot with a homogeneous indium distribution, does not need any further consideration, as this e_{zz} profile would result in a *decreasing* lattice constant in the growth direction, which is opposite to what we observe in our STM images. Furthermore, we already showed in section 7.3.3 that the dots have the shape of a truncated pyramid rather that of a full pyramid. Profile (b) in Fig. 7.10, corresponding to a dot with the shape of a truncated pyramid and a homogeneous indium distribution, can be ruled out as this e_{zz} profile would result in a constant lattice constant inside the dot, which is clearly not observed. That the dots do not consist of pure InAs or homogeneous InGaAs was also already shown in section 7.3.5. By using the e_{zz} profile (c) from Fig. 7.10, which includes the indium gradient that was already determined earlier [2], it is possible to calculate (Eq. 7.1) the lattice constant profile, see Fig 7.9. From this it is clear that the increase in lattice constant is indeed caused by the indium concentration gradient in the dot and not e.g. by geometrical properties of the dot. The observed lattice constant, however, is affected by surface strain relaxation occurring after cleavage, which has to be included in the calculation. From elastic response theory, a larger lattice constant for the cleaved dot is expected.

By again using the *Abaqus* program, this time to calculate the lattice constant profiles for a cleaved dot, it is shown that from the investigated models, indeed, only the model assuming a linear indium gradient of 60% to 100% towards the top of the dot, as proposed by [1,2], gave the best fit to our measured relaxation profiles. The gradient in lattice constant is reproduced well and, as expected, the average lattice constant is larger than the calculated values for an un-relaxed surface. Thus relaxation and lattice constant profiles obtained from X-STM measurements can both be used to determine the local indium concentration in quantum dots with an accuracy of about 10%, although the used model assumes the elastic constants in the lattice to be isotropic.

The calculated values of the lattice constant and relaxation profile show a clear local maximum at the position of the wetting layer, which is located at the bottom of the dot. This local maximum is absent in the measurements. This indicates that the assumptions made for the wetting layer should be improved. In the numerical calculations the wetting layer is considered to be a 0.6 nm thick continuous pure InAs layer on top of which the quantum dots are located. From the X-STM images, however, it is clear that the wetting layer does not consist of pure InAs, so the assumed indium concentration in the wetting layer is probably too high.
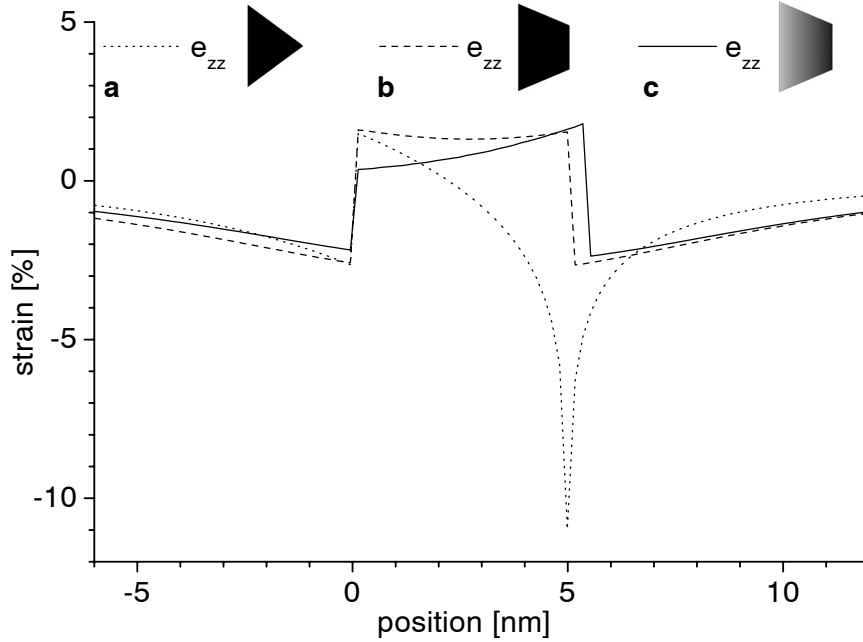
Fig. 7.10: *Strain component in the growth direction (e_{zz}) through a cross-section of the dot for (a) a full pyramid consisting of pure InAs [36] (b) a truncated pyramid consisting of pure InAs and (c) a truncated $In_xGa_{1-x}As$ pyramid with the indium composition gradient as proposed by the Abaqus calculations of Barker et al [2]*

7.3.7   Electron wavefunctions inside the dots

7.3.7.1 CITS measurements on cleaved quantum dots

As was already discussed in sections 3.2.2 and 4.7 it might be possible to image the wavefunctions inside the quantum dots by using CITS measurements [37]. At room temperature, however, the separation between the hole states in the quantum dot are so small that they probably cannot be resolved. The separation is small due to the high effective mass of the holes, the asymmetric band offsets and the high complexity of the band structure of the valence band of the quantum dots. In the case of electrons, however, the band structure is simpler and the effective mass is much smaller. Therefore it should be possible to resolve the different states of the electron wavefunctions, as the separation between these states is much larger.
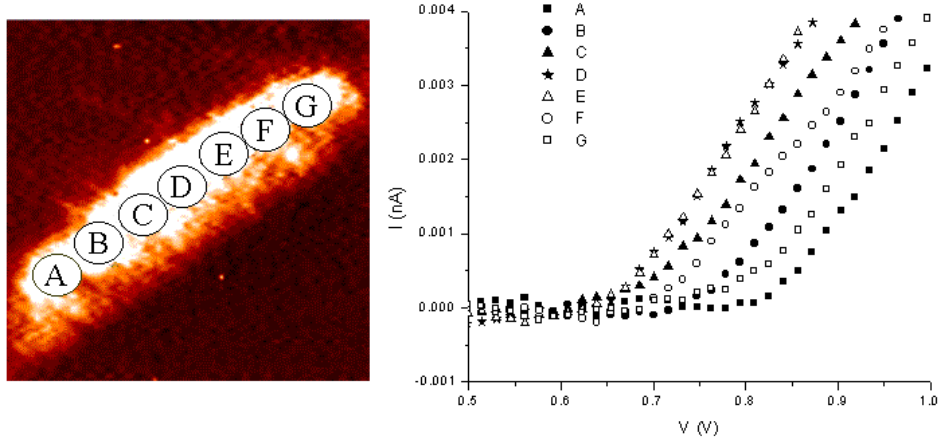
Fig. 7.11: *I(V) spectra taken at different positions above the cleaved quantum dot. The setpoint during the measurements was taken in the filled state mode. Only the empty state branch of the I(V) curves, where the electron states are located, is shown*

In Fig. 7.11, I(V) spectra are shown, taken at different locations above the cleaved dot. It can be seen that there are distinct differences in the curves taken at different positions. The spectra that are taken at an equal distance from the center of the cleaved dot, for instance A&G and B&F, show a similar behavior. In the I(V) curves, however, no distinct "kinks" are visible, which would be expected when tunneling into an energetically different confined electron state, as was demonstrated in Ballistic Electron Emission Microscopy (BEEM) experiments [38]. Therefore CITS images were generated from the I(V) spectra taken on the cleaved quantum dot, see Fig. 7.12, to make the local differences in the I(V) spectra more visible. During the CITS measurements the setpoint of the STM was chosen in the filled state mode. In this way, the image current in the empty state branch of the I(V) spectra is free to run, without being forced through the setpoint. We think that the electron wavefunctions can be imaged in this way.

At low voltages, an elliptical maximum, near the top of the dot is observed. When increasing the voltage, extra lobes are formed on both sides of the initial maximum. The fact that these maxima are located near the top of the dot is an indication that the electrons are confined in the top of the dot. This is related to the indium gradient present in the dot, which causes a gradient in the conduction band that results in a shift of the localization of the electrons towards the top of the dot. This, however, does not give any information about the position of the exciton (if present in the cleaved dot), as only the electron wavefunctions are imaged. The first observed elliptical maximum is attributed to the s-ground state of the electron wavefunction. The two extra lobes that appear at higher voltages can be caused by the lobes of the *p*-state of the electron wavefunction, or higher excited states. The separation between the observed *s*- and *p*-state maxima is about 200-300 meV. In order to image the hole wavefunctions, the setpoint was chosen in the empty states branch of the I(V) curves. However, as expected, no bound hole states were observed in the filled states, as the whole dot appeared bright at all voltages in the CITS measurements taken in the filled state mode.
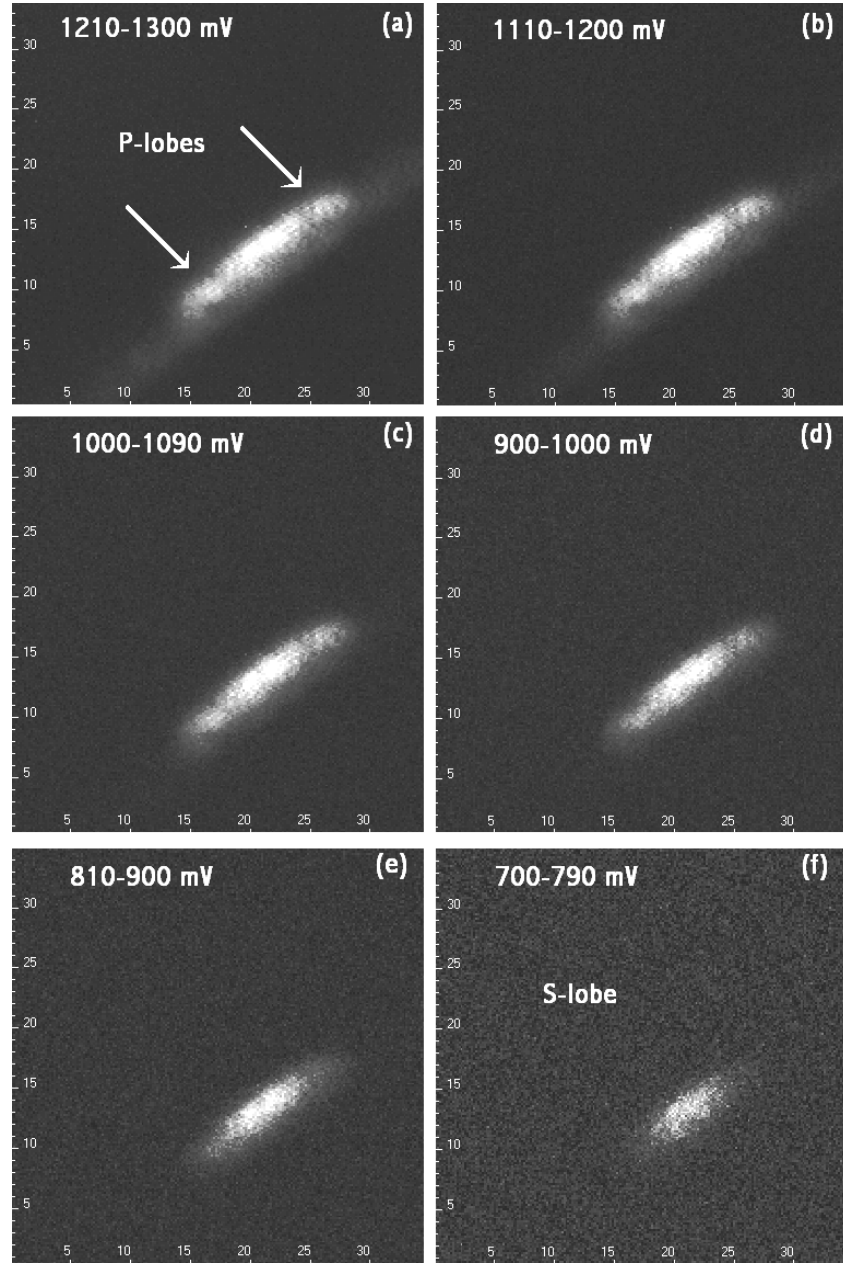
Fig. 7.12: *CITS images of a quantum dot, showing the s- and p-type electron wavefunction. To reduce noise each CITS image shown is obtained by averaging 10 CITS images in the indicated voltage ranges (step size between the measured CITS images was 10 mV). The electrons seem to be confined in the top of the dot. Image size 35x35 nm^2*

7.3.7.2 Calculation model

The interpretation of CITS measurements on quantum dots (and other nanostructures) can be difficult as the appearance of the wavefunctions in the CITS images depends on the shape and composition of the cleaved dots. Therefore, numerical simulations have been performed by M. Roy and P.A. Maksym (Department of Physics and Astronomy, University of Leicester) in order to simulate how the wavefunctions of confined states would appear in the CITS images. These numerical simulations have been used to interpret the CITS images. The problem with existing calculations of confined dot states is that often the shape used for the quantum dots is different [39] and that the calculations give the wavefunctions inside *complete* dots, whereas the measurements have been performed on cleaved ones [2,39]. Furthermore, the resulting CITS image (which is a map of the integrated DOS or the current distribution) in the STM measurements had still to be calculated.

The dot used in our numerical calculations is identical to that from sample #1 and it has been allowed to deform outward at the dot-vacuum interface. This changes the strain in the dot and thus the electron-hole confinement. Furthermore, the dot is cleaved through the center along its diagonal, as is the case for the dot we analysed in the X-STM measurements.

In the model used, the dot states are calculated within the effective mass approximation using the position dependent masses and strains for the deformed, cleaved dot. The dot states are obtained from an expansion containing approximately 10000 linear harmonic oscillator basis functions. In this way, the calculated energies converge within a few meV to the actual energy level of the calculated state. Following the Tersoff and Hamman approach [40], the wavefunctions of the STM tip can be approximated by the asymptotic spherical form:

$$\psi_{tip} \approx \frac{\exp(-k \, | \, r - r_o \, |)}{k \, | \, r - r_o \, |} \qquad (7.2)$$

and the tunneling current is calculated within first order perturbation theory,

$$I \approx | < \psi_{dot} \, | \, \psi_{tip} > |^2 \qquad (7.3)$$

In this approximation the tip and dot states are independent.

For (110) surfaces with no surface states within the bulk bandgap, we assume zero band bending at the interface [41]. The potential barrier at the vacuum (see Fig. 7.13) is set from the electron affinity of GaAs.

For tunneling into the nth bound state, the inverse decay length for the tip wavefunction is given by:

$$k = \hbar^{-1} (2m_o(4.07 + E_n))^{0.5} \qquad\qquad (7.4)$$

where m_o is the bare electron mass. Because the tip and dot states are assumed to be independent, the magnitudes of k and m_o do not change within the semiconductor. The effect of the Bloch states on the dot wavefunction and the effect of bandbending have not been included in the calculation model yet.
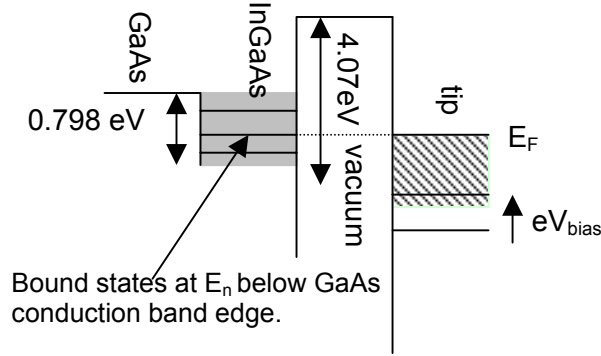

Fig. 7.13: *Potential barrier of the tip, vacuum, InGaAs and GaAs*

7.3.7.3 Calculation results

Using this set of approximations a map of the current density, as obtained from CITS measurements can be simulated. The resultant tunneling current is extremely sensitive to the tail of the dot wavefunction on the vacuum side of the dot-vacuum interface. If the STM tip is moved too far from the dot (> 1.5 nm), the obtained signal is so small that only noise in the numerical calculation of the dot states is obtained. Therefore, the tip-sample distance is set to 0.5 nm in the calculations, which is a realistic value as can be seen in Fig 5.2a. In Fig. 7.14 the surface of the cleaved dot is indicated, which is scanned with the X-STM and that is used in the calculations.
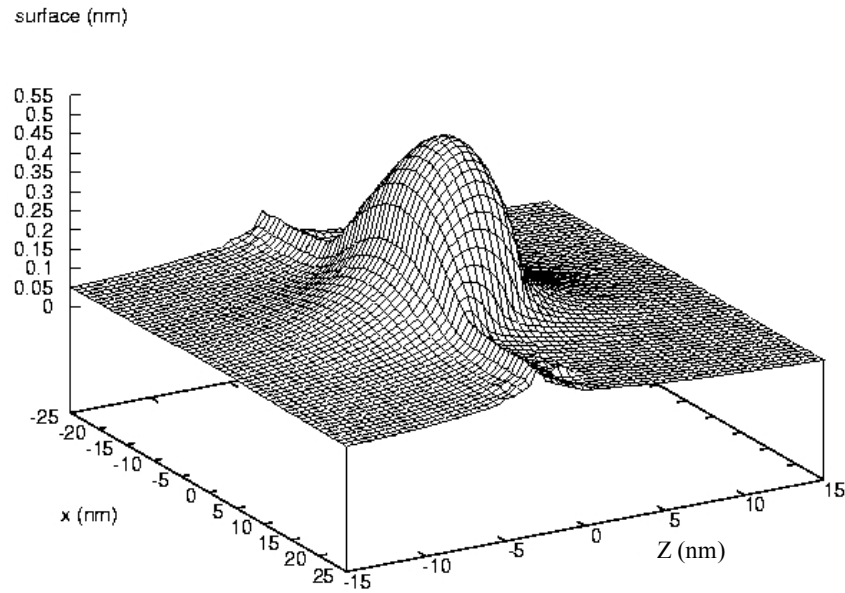
Fig. 7.14: *Surface of the dot. The maximum deformation is ~0.5 nm. The STM tip scans across the XZ plane, 0.5 nm above the deformed dot surface*

In Fig. 7.15 the calculated STM tunnel current images are shown, with the contributions from tunneling into 4 bound states inside the dot. The states are bound at –0.27 eV, -0.17 eV, -0.10 eV and –0.07 eV below the GaAs conduction band edge. Interestingly, the states in the cleaved dot are more tightly bound than those in the full dot. This is because the dot has relaxed outward at the surface. The relaxation reduces the hydrostatic strain in the half cleaved dot, and hence increases the magnitude of the conduction band offset between the dot and the substrate compared to a cleaved un-relaxed dot.
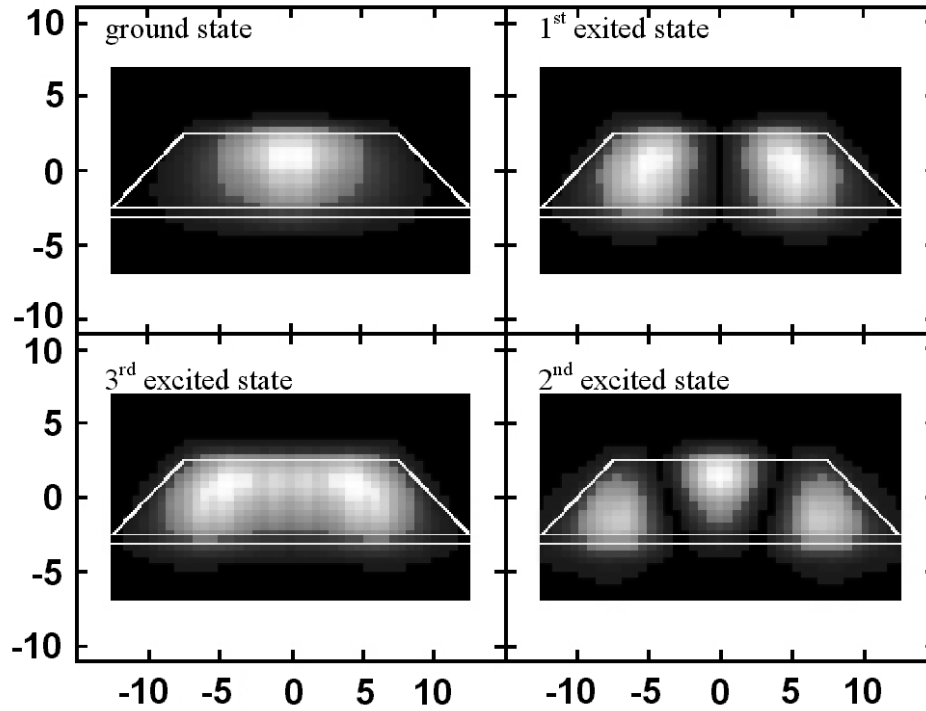
Fig. 7.15: *Calculated STM current map (CITS) obtained from tunneling into the bound states inside the dot. Clockwise from the top left, images are shown obtained from tunneling into the ground state up to the 3rd excited state in the lower left corner. The white lines show the outline of the un-deformed dot and wetting layer*

Although the effect of bandbending is not taken into account in the used model, the influence of bandbending is estimated by using the *IVCHAR* program (see Section 5.4). Using the magnitude of the bandbending, which was determined by our numerical simulations, the perturbed wavefunctions were calculated. The maximum shift in the potential across the dot is in then 33 meV, which is less than 10% of the total well depth, which is approximately 500 meV. These calculations indicate that the absolute magnitude of the tunnel current might be reduced and minor changes in the shape of the dot states are expected. These effects of bandbending on the calculated current distribution are, however, expected to be very small and can be neglected with respect to other approximations made in the calculations, like the spherical tip wavefunctions.

The images obtained for the ground state and second excited state show qualitative agreement with some of the experimental STM data. Encouragingly, the separation of the maxima in the current for the 2nd excited state is 9.1 nm in the theoretical case and about 9.3 nm from the "1210 mV - 1300 mV" data set measurement (Fig. 7.12). The problem, however, is that the shape of the nodes we see in the CITS measurements resemble most to the calculated images of the ground and 3rd excited state, whereas the 1st and 2nd excited state seem to be absent in the measurements. However, the energy separation between the ground and 3rd excited state (200 meV) agrees reasonably well with the measurement (200-

300 meV). The fact that some excited states are not observed may be due to the fact that during the CITS measurements more that one state can contribute to the current. This is due to the exponential decay of the tunnel probability, which causes that states that are located *below* the tip Fermi-Energy (in the "exponential tail" of the tunnel probability) still may give a contribution to the tunnel current as well, see Fig. 5.1. This leads to an overlap of states in the CITS images, which causes the 1st and 2nd excited state to be blurred and mixed with the other states. Also the fact that in the I(V) spectra of Fig. 7.11 no "kinks" are observed can be explained by this. Although the interpretation of CITS images still remains a point of investigation, the calculations can give an indication of what can be expected in CITS images, and that observable bound states could be present inside the dot.

7.4   High growth rate InAs quantum dots

7.4.1   Sample #2 (R142 Eindhoven)

The second quantum dot sample contained 9 layers Stranski-Krastanov (SK) grown InAs islands and was grown by Molecular Beam Epitaxy (MBE) within our own growth facility on a (100) GaAs substrate at a substrate growth temperature of 495°C. During growth different amounts of InAs were deposited to form the quantum dot layers: 1.5 monolayers (ML), 2.0 ML and 2.5 ML InAs. During growth of the InAs dot layers, growth interrupts of 10 seconds have been applied. A single and a double AlGaAs marker layer, which were included in the structure between the different quantum dot regions, made a clear distinction possible between the regions containing dot-layers with a different InAs deposition amount (see Table 7.2). The growth speed of the quantum dot layers was 0.1 monolayers per second.

The difference in the growth temperatures of sample #1 and #2 can be neglected, as these samples were grown in different MBE machines. The determination of the exact growth temperature is quite difficult and different MBE machines have a different growth temperature calibration. During growth, no change in the RHEED pattern was observed during the deposition of the 1.5 ML dot layer, indicating that no dots had been formed in this region. During the deposition of the 2.0 ML and 2.5ML InAs layers, a clear change in the RHEED pattern, from streaky to spotty, was observed. This is an indication for the formation of quantum dots. In Fig. 7.16 an overview image of this sample is shown. Indeed quantum dots have formed in both the 2.0 ML and 2.5 ML layers and they can be clearly distinguished from each other due to the presence of the double AlGaAs marker layers.

In Fig. 7.17 a quantum dot from the 2.0 ML and a quantum dot from the 2.5 ML layer are shown. Although only a limited amount of dots could be investigated, it was possible to determine a minimum size of the dots, see Table 7.3. The height and base length were determined from the X-STM current images, as was done for the quantum dots from sample #1. In the 1.5 ML layer, no dots were found within the entire range of the scanner, i.e. 2.4 µm measured along the layer. This agrees with the RHEED measurements during growth of the sample, which showed no signs of dot formation. Furthermore the amount of deposited InAs was well below 1.7 ML, which is generally assumed to be the minimum amount of InAs a GaAs for SK-dot-growth to occur.

Material	Thickness		Growth Temperature
GaAs	3800 Å		580 °C
GaAs	200 Å		495 °C
InAs	2.5 monolayer		495 °C
GaAs	500 Å	2.5 ML QDots	495 °C
InAs	2.5 monolayer		495 °C
GaAs	500 Å		495 °C
InAs	2.5 monolayer		495 °C
GaAs	300 Å		580 °C
$Al_{0.3}Ga_{0.7}As$	50 Å		580 °C
GaAs	50 Å	Marker A	580 °C
$Al_{0.3}Ga_{0.7}As$	50 Å		580 °C
GaAs	100 Å		580 °C
GaAs	200 Å		495 °C
InAs	2 monolayer		495 °C
GaAs	500 Å	2 ML Qdots	495 °C
InAs	2 monolayer		495 °C
GaAs	500 Å		495 °C
InAs	2 monolayer		495 °C
GaAs	300 Å		580 °C
$Al_{0.3}Ga_{0.7}As$	50 Å	Marker B	580 °C
GaAs	100 Å		580 °C
GaAs	200 Å		495 °C
InAs	1.5 monolayer		495 °C
GaAs	50 Å	1.5 ML Wetting	495 °C
InAs	1.5 monolayer	Layer	495 °C
GaAs	50 Å		495 °C
InAs	1.5 monolayer		495 °C
GaAs	1000 Å		580 °C
GaAs substrate n-type Si doped			

Table 7.2: *Growth menu sample #2. The InAs growth rate was 0.1 ML/s*

Table 7.3 shows that deposition of more material leads to a small increase of the dot size. It is assumed that a larger InAs deposition amount mainly leads to an increased dot-density, which can be observed in the X-STM measurements shown in Fig. 7.16. AFM investigations on similar structures have shown that this is generally correct [9,25].

The size of the dots (both height and base length) found in sample #2 is very different from the dot size found in sample #1 (2.4 ML InAs deposited). Although the size of the dots in sample #2 increases with the deposition amount, even the 2.5 ML dots are still significantly smaller than those in sample #1 (2.4ML InAs). This smaller size of the quantum dots can be explained by the fact that a higher deposition rate increases the dot density and reduces the size of the dots as the amount of deposited material is limited [42]. This was confirmed by AFM measurements performed within our own group by T. Mano on similar uncapped structures, where the deposition rate was varied, and other STM investigations [42].
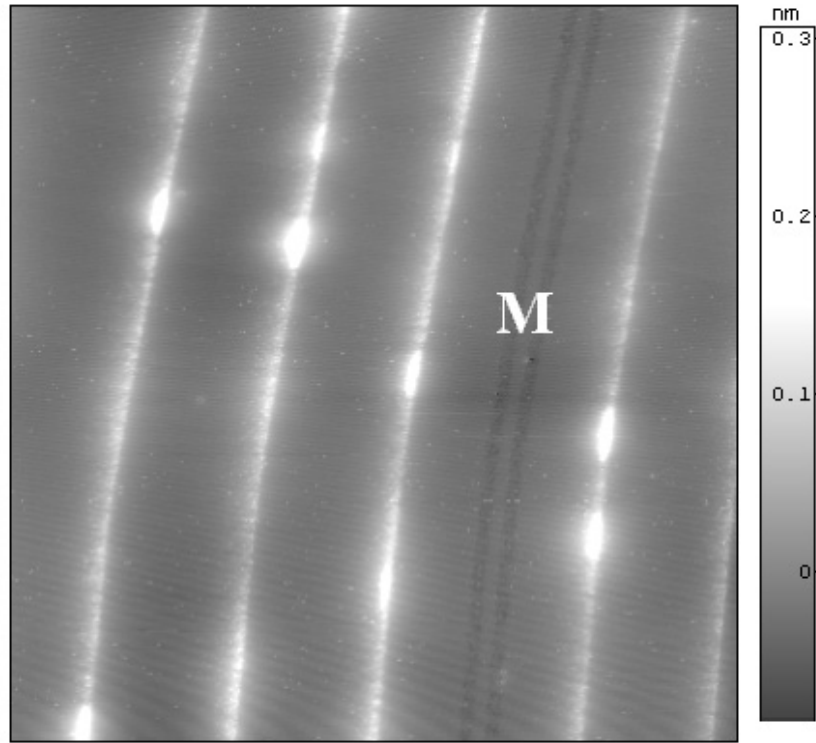
Fig. 7.16: *Sample #2 (R142). 240x240 nm^2 overview image of the sample showing the double AlGaAs marker (M), enabling the identification of the 2.5 ML (on the left hand in the picture) and 2.0 ML (on the right hand in the image) layers. In both the 2.0 ML and 2.5 ML layers quantum dots have formed and areas containing only the wetting layer without any dots in the vicinity can be investigated*

Amount of InAs deposited	Height	Base Length (diagonal)
2.5 ML	3.6 ± 0.5 nm	25 ± 2 nm
2.0 ML	3.1 ± 0.5 nm	22 ± 2 nm
1.5 ML	No quantum dots observed in RHEED and X-STM	

Table 7.3: *Maximum observed height and base length of the quantum dots*

If we look at the general shape, there are other clear differences visible: the high growth rate dots from sample #2 do clearly not have the shape of a truncated pyramid. No clear side facets are observed. As we observe a nearly perfect flat top of the dots, the shape could be best approximated by that of a disk rather than by a lens shape. Furthermore the aspect ratio is much larger for the high growth rate dots.

We conclude that due to the high InAs deposition rate, diffusion processes do not have enough time to form well-defined facets. Also the theory that during growth full pyramids are formed from which the top dissolves when the dots are capped [12], seems to be very unlikely if we look at our results, as no pyramidal shape or individual indium atoms around or next to the dots were observed. The same holds for sample #1, as no extra individual indium atoms around the dots or indium rich regions next to the dots in or above the wetting layer were found.
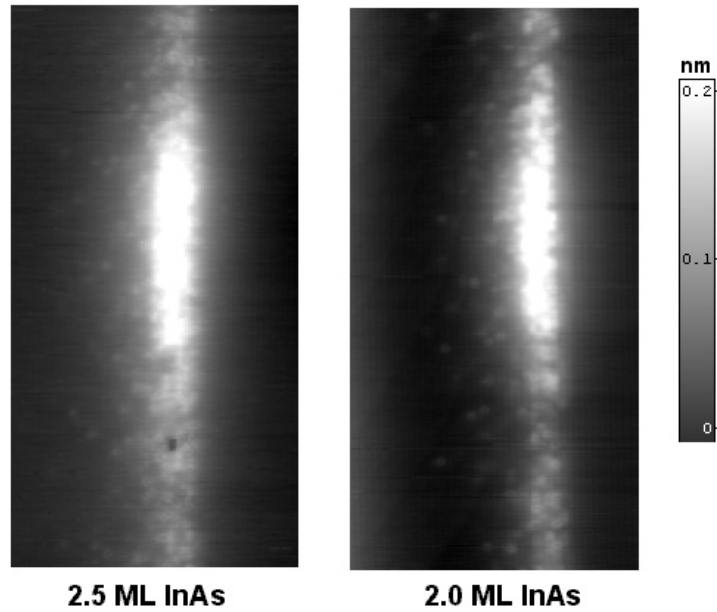

Fig. 7.17: *Two topography images of different quantum dot layers. During growth 2.5 monolayers and 2.0 monolayers of InAs were deposited, respectively. Image size 50x25 nm^2, V_{tunnel} = -2.500 V*

In the current images of the dots, again small short ranged fluctuations are visible, indicating that the dots consist of an alloy, rather than pure InAs. In order to get some insight in the composition of the dots, relaxation profiles were taken across the center of the dots, see Fig. 7.18. The images were taken at high negative bias (filled state mode) for electronic contrast suppression. The 2.5 ML dot shows a stronger relaxation than the 2.0 ML dot. This can be due to two factors: (1) the indium concentration inside the 2.5ML dot is higher, or (2) due to the fact that the 2.5 ML dot is larger, i.e. the amount of buried material underneath the cleavage surface is larger, which causes the strain to increase resulting in a larger outward relaxation upon cleavage. It is thus very difficult to draw direct conclusions from this and numerical calculations should be used for a precise composition determination.

However, when looking at the relaxation profiles in Fig. 7.18, it can be seen that the relaxation profiles are almost symmetric with respect to the dot center. In the numerical

calculations performed on sample #1, it was shown that this indicates a constant indium concentration. In the relaxation profiles, there is a small amount of asymmetry as the right hand side is slightly steeper than the left hand side. This asymmetry can be due to the wetting layer that can have a different composition than the dot on top of it. Depending on the growth rate, the aspect ratio of the dots, which is the base length of the dot divided by its height, changes. For lower growth rates the aspect ratio will be smaller, resulting in steeper dots. When the dots are capped with GaAs the dots will partially collapse, resulting in dots with a slightly larger base and reduced height. The smaller the aspect ratio of the dots (e.g. pyramidal dots), the smaller this effect will be [43]. In the high growth rate case, with the low aspect ratio of the uncapped dots, a constant InGaAs composition is present, as there is no time for diffusion processes to cause a composition gradient inside the dot. In the low growth rate dots, however, gallium is incorporated at the initial formation stage of the dot, i.e. during wetting layer formation and just after. When the dot is further formed by adding more InAs, the gallium atoms will diffuse towards the top of the dot. Furthermore, it will become harder to incorporate gallium during dot formation as the surface becomes depleted from free gallium, as only indium and arsenic atoms arrive at the growth surface during dot growth. This can result in the observed indium gradient. Altogether the formation of quantum dots is a very subtle play of layers being in thermal equilibrium or not. Dots that have been formed at the growth surface, and have reached equilibrium, will not have to be in equilibrium anymore after being capped, resulting in a change of the aspect ratio and composition.
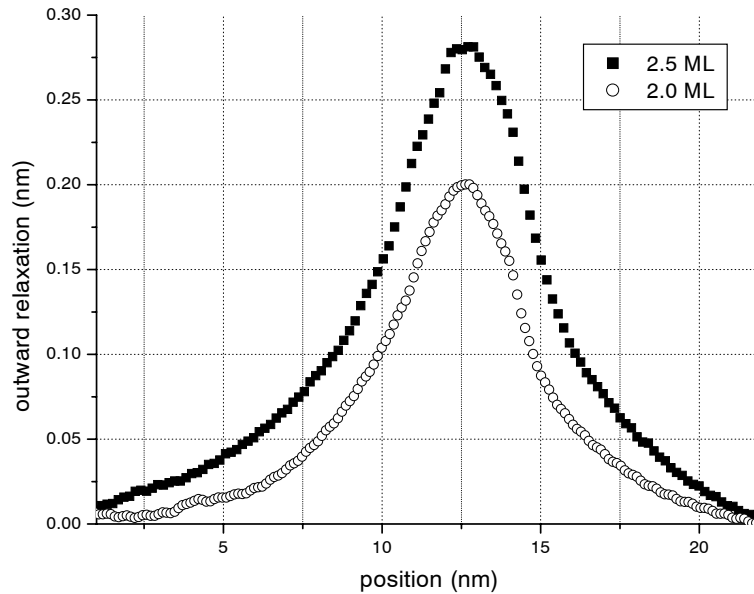

Fig. 7.18: *Relaxation profiles across the 2.5 ML and 2.0 ML, 0.1 ML/sec growth rate InAs quantum dots. Growth direction runs from right to left. A small depression is visible at the position of the wetting layer at the right hand side of the quantum dots. The profiles are obtained by averaging several line profiles next to each other at the center of the dot. $V_{tunnel} = -3.000\ V$*

7.4.2   Sample #3 (R24 Eindhoven): Formation of dot nucleation centers

Finally, a sample similar to sample #2 was investigated. However, there were a few differences between sample #2 and #3. In sample #3 there was just a single 1.5 ML, 2.0 ML, 2.5 ML InAs deposition sequence, making it much harder to find layers at the cleaved surface without any stepedges running trough it. Due to stepedges on the growth surface and inhomogeneities at the growth surface, dot nucleation centers can already form at certain areas of the wafer at deposition amounts that are less than 1.7 ML InAs. This was indeed the case, as during growth already for the 1.5 ML InAs layer a small change in the RHEED pattern was observed. Although the surface reconstruction could not clearly be determined, there was an indication of dot-formation at 1.5 ML InAs deposition. This demonstrates that dot formation indeed can take place even if the amount of deposited InAs is less than 1.7 ML.

As was expected from the RHEED pattern during MBE, dot nucleation sites could be found in the 1.5 ML layer in our X-STM measurements, see Fig. 7.19(a,b). The base length of this dot is 7.5 ± 0.5 nm and its height is 3.0 ± 0.5 nm. Like in sample #2, the relaxation profile, measured while suppressing the electronic contrast, is in this case perfectly symmetric, indicating the absence of an indium gradient inside these dots (see Fig. 7.19c). The measured outward relaxation was 220 ± 5 pm, which is very large compared to the profiles obtained from sample #2, taking the small size of the dots in consideration. In the current images (Fig. 7.19b) there are almost no small short-ranged fluctuations visible inside the dot. These two facts are a strong indication that these small dots must consist of almost pure InAs. This shows that alloy formation during overgrowth of the dots is suppressed at these small InAs deposition amounts.

In the bottom part of Fig. 7.19(a), a clear densification of the wetting layer is visible. It is not possible to determine if cleaving through one of the corners of a dot causes this densification, or if this is a pre-stage of a dot nucleation site. However, as no clear contours are visible and this feature is rather high in comparison with the wetting layer and the observed quantum dot, see Fig. 7.19(c), the latter explanation is the more likely.

It is thus possible to fabricate very small high-growth-rate quantum dots with high indium concentration by decreasing the amount of InAs deposited. Dots with high indium content are favorable as the energy separation of the electron energies inside these dots and thus electron confinement is stronger than in alloyed dots (reduced leakage of the wavefunction). The smaller size of the dots can lead to a higher confinement, although there exists an optimum. Reducing the size of the dots too much decreases the electron confinement in the dots again. However, in general the dot density decreases if less material is deposited, which is not favorable for device performance, as e.g. laser output power depends on the amount of dots.
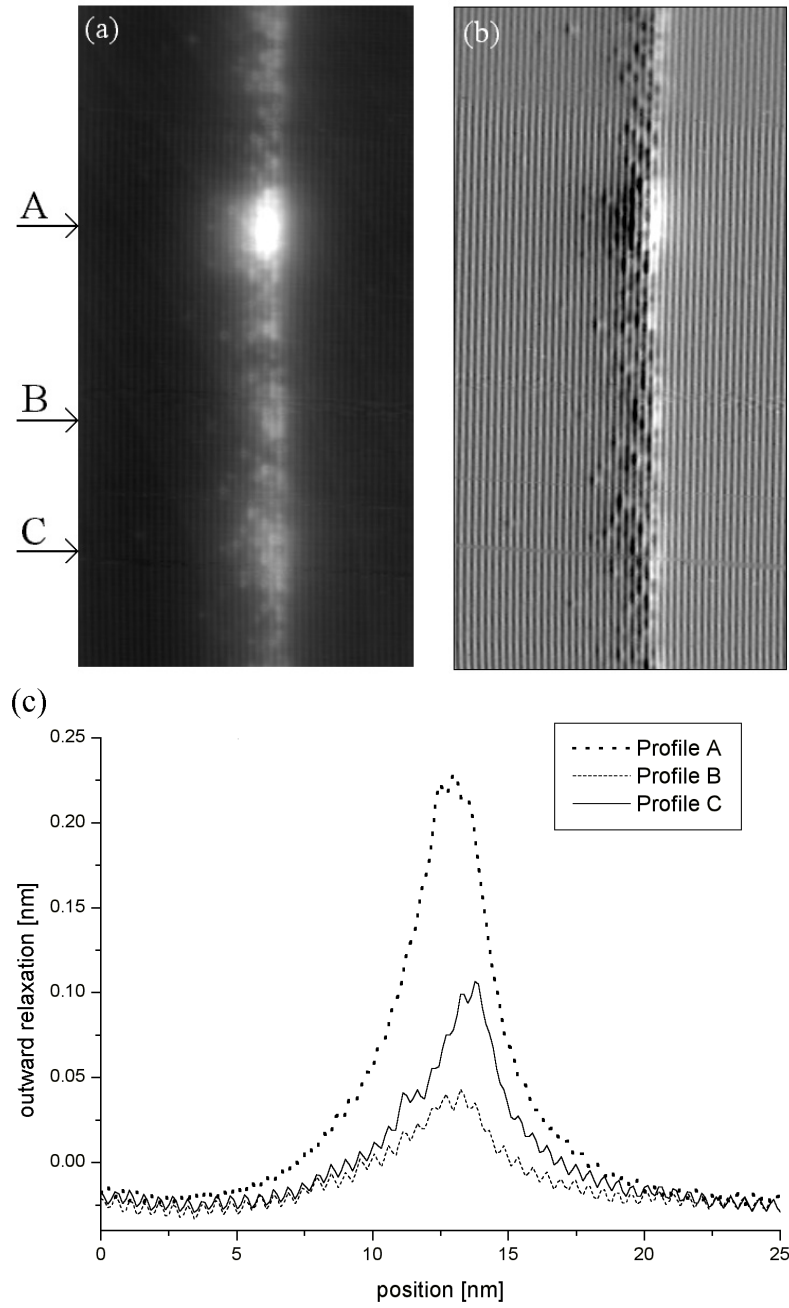
Fig. 7.19: *Quantum dot nucleation center. (a) Topography image, entire color scale is 300 pm. (b) Current image. Image size 25x50 nm², V$_{tunnel}$ = -3.000 V. At the bottom of the image a densification of the wetting layer is visible. The growth direction is from the right to the left. (c) Outward relaxation profiles taken across the dot (A), the wetting layer (B) and the pre-stage (C)*

7.5   Wetting layer formation

Before InAs quantum dots are formed in a GaAs matrix during Stranski-Krastanov growth, at least 1.7 ML of InAs has to be deposited to form a wetting layer. It is unclear, however, what happens after the wetting layer has been formed and dot formation takes place. Is the wetting layer stable or does it change during the deposition of more material? This is an issue that has been discussed more often in literature, but which is still not fully resolved [7,44-47]. Therefore we investigated wetting layers with and without quantum dots and the influence of the amount of deposited dot material. The average composition and the indium composition profile inside the wetting layer are of interest. In order to get a better understanding in what is exactly happening during the formation of quantum dots, the wetting layer at a distance far from the dots, was investigated.

In Fig. 7.20 the average outward relaxation profiles of the wetting layers of the 2.5 ML, 2.0 ML and 1.5 ML InAs deposited layers are shown. The electronic contrast suppression technique, as described in Chapter 5, was applied resulting in images that show only the real outward relaxation profile without any (or only very small) electronic contrast. From Fig. 7.20 it is clear that the 2.0 ML and 2.5 ML wetting layers can be considered to be identical. This indicates that after the deposition of the critical InAs layer thickness of 1.7 ML all the surplus of material goes into the formation of quantum dots, leaving the wetting layer unaffected and stable. Adding more material inside the layer will not only result in larger dots, but will mainly result in an increased dot density [9,25]. In Fig. 7.20 it also can be seen that the deposition of 1.5 ML InAs, were no dots have been formed, leads to a lower relaxation profile, as less indium and thus less strain is present inside this layer.

Using the theory from 3.4, which was used to calculate the relaxation profiles of cleaved quantum wells (chapter 5) it is possible to calculate the relaxation profile for a given indium concentration profile. It is thus possible to determine the indium concentration profile by fitting calculated relaxation profiles to the measured profiles. Not only the composition but also the average width of the wetting layer can be determined within 1 ML.

We assume that the indium concentration profile has an exponential decay, which is to be expected as the broadening of the wetting layer is likely to be caused by strain driven diffusion and segregation processes**.** The calculated relaxation profiles were fitted to the 2.5 ML wetting layer measurements (which are equivalent to the 2.0 ML wetting layers as demonstrated in Fig. 7.20). The result of a 4 parameter fit to the relaxation profile, where the width of the wetting layer, the slope of the exponent (slope), the maximum concentration (N_{max}) and the peak shift (x_0) were varied to obtain the best fit, is shown in Fig 7.21. The calculated outward relaxation profile agrees very well with the measurements. It was not possible to obtain an accurate fit assuming a linear indium concentration profile or a constant indium concentration inside the wetting layer.

If we look at the STM images of the dots and the wetting layers (Figs. 7.16 and 7.17), the average thickness of the wetting layer is estimated to be 6 ± 0.5 atomic bi-layers (3.3 nm), which is in good agreement with the calculated value of 3.1 nm. If we integrate the calculated concentration profile, we find an average value of 15% indium inside the wetting layer. This is the expected value, as 1.7 ML of pure InAs, equally distributed over a 3.1 nm thick wetting layer would result in a layer with an average indium content of 14.9%. This is again a strong proof that after the deposition of 1.7 ML InAs no more material is built into the wetting layer.
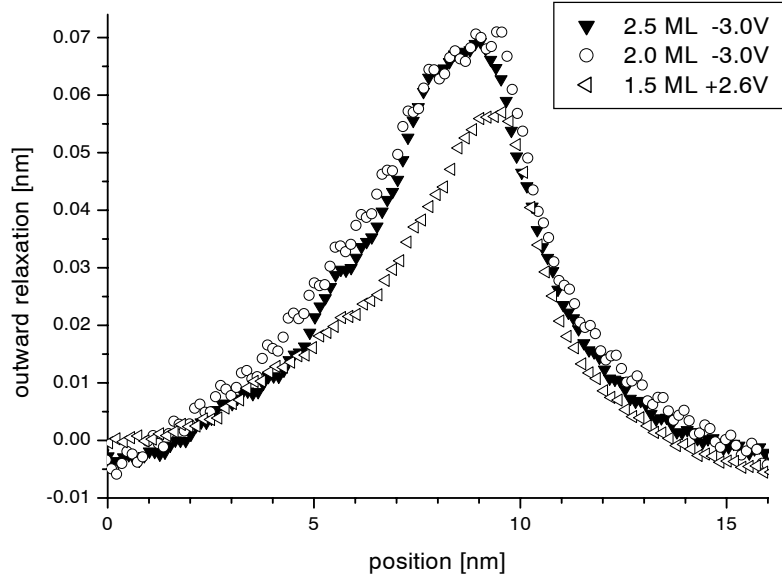
Fig. 7.20: *Relaxation profiles of the wetting layers for an InAs deposition amount of 1.5 ML, 2.0 ML and 2.5 ML. The profiles for the 2.0 ML and 2.5 ML case were obtained at $V_{tunnel} = -3.00$ V, thus suppressing electronic contrast completely. The 1.5 ML wetting layer, which does not contain any quantum dots, was obtained at $V_{tunnel} = +2.60$ V. Therefore it may contain some small residual electronic contrast (see Fig. 5.2), which results in a measured value of the outward relaxation that is slightly larger than the actual value. The growth direction is from the right to the left*

This analysis shows that not only wetting layers are stable after their formation, but also (again) that X-STM can be successfully used to determine (average) size and compositional profiles of 2D structures with high accuracy, i.e. within a few percent concerning composition and within one bi-layer with respect to the thickness of the layers.
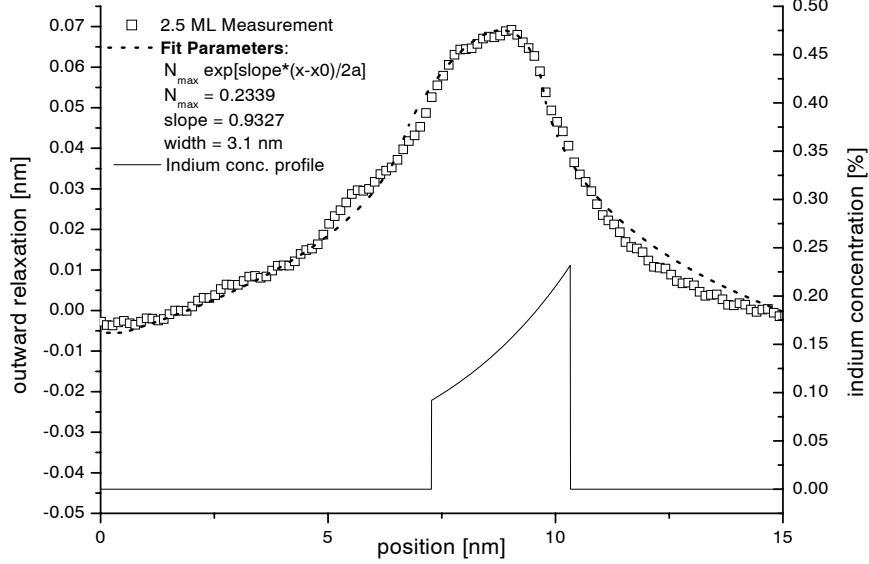
Fig. 7.21: *Exponential indium concentration profile fit of the outward relaxation profile as calculated for the 2.5 ML wetting layer. The growth direction is from the right to the left. The parameters of the indium composition profile (solid line) have been adjusted in such a way that the resulting calculated outward relaxation profile (dashed line) yields the best fit to the measured outward relaxation profile. Doing so the most likely composition profile and width of the wetting layer can be determined*

7.6   Conclusions

By using the X-STM a conclusive, comprehensive determination of the shape, size and composition of self-assembled quantum dots is possible. By analyzing constant current images the height vs. base length distribution of InAs quantum dots in a GaAs matrix was determined. By using this distribution plot the shape of low growth rate InAs quantum dots could be determined. This result is in agreement with previous theoretical analysis of photocurrent results [1,2].

By analyzing voltage dependent relaxation profiles of these quantum dots, the electronic contrast could be suppressed, like in the quantum well case (Chapter 5). This resulted in height profiles showing only the real outward relaxation of the cleaved dot. From numerical calculations, which were performed by using the *Abaqus* program, it was possible to determine the linear indium concentration profile inside the dots. Furthermore the calculated lattice constant profile for this concentration profile compared well to the measured lattice constant profile. The determined indium concentration profile agreed with the profile that was proposed from previous photocurrent results [1,2]. This demonstrates that X-STM can be successfully used to determine concentration profiles in 2D as well as 3D structures.

In CITS measurements the wavefunction inside a cleaved dot was imaged and compared to numerical calculations. The model used in the calculations takes into account that the dot is cleaved. Also the influence of the outward relaxation of the dot and the influence of the resulting strain profile upon the local energy separation between the different states is included. Furthermore the influence of bandbending upon the calculation model and the effect on the position and magnitude of the different electron states were investigated. The morphology and magnitude of the current distribution of the ground state and the first 3 excited electron states of the wavefunction were calculated and compared to the CITS measurements. The agreement in shape and energy separation between the ground and 3rd excited state demonstrates that the model used in the calculations can give a good description of the imaging processes involved in CITS measurements. This model can therefore be used to predict which morphology of the CITS measurement is to be expected.

High growth rate InAs quantum dots with different deposition amounts (1.5 ML, 2.0 ML and 2.5 ML of InAs in a GaAs matrix) were investigated. The higher deposition rate resulted in lower dots, with a constant InGaAs composition. This can be explained by the higher aspect ratio (with respect to low growth rate quantum dots) of the dots before capping, which causes a different behavior upon capping of the dots. A larger amount of deposited InAs results in dots that are only slightly larger. The major part of the extra material is used in the formation of extra dots, resulting in an increased dot density. If the deposition amount is reduced, however, very small dots with a large electron confinement can be produced, although the dot density will be low then.

By investigating the wetting layers of the high growth rate quantum dots by X-STM, it was found that once dot formation has started, all extra deposited material will be incorporated in the dots. Therefore the wetting layer will, once it has been completely formed after the deposition of 1.7 ML of InAs, remain stable. By using the procedure from Chapter 5, the indium concentration profile inside the wetting layer was calculated. An exponential decay of the indium concentration in the growth direction gave the best fit, as the broadening of the wetting layer is likely to be caused by strain driven diffusion processes. The calculated average indium concentration was equal to the average concentration, which is expected for the deposition of 1.7 ML InAs in a layer with both the observed and calculated thickness. This proofs that the deposition of 1.7 ML InAs on GaAs indeed results in a complete "closed" wetting layer.

In this chapter X-STM has been employed to investigate complex growth processes that occur during formation and capping of wetting layers and quantum dots The exact theoretical background of these growth phenomena, however, has only been discussed briefly since these growth related topics are outside the scope of this thesis and are still under discussion in literature [8,12,13,15,25-32].

References

[1]   P.W. Fry *et al*., Phys. Rev. Lett. **84** (4), 733 (2000)

[2]   J.A. Barker and E.P. O'Reilly, Phys. Rev. B **61** (20), 13840 (2000)

[3]   P.B. Joyce *et al*., Phys. Rev. B **58** (24), 15981 (1998)

[4]   I. Kegel *et al*., Phys. Rev. Lett. **85** (8), 1694 (2000)

[5]   B. Grandidier *et al*., Phys. Rev. Lett. **85** (5), 1068 (2000)

[6]   B. Legrand *et al*., Appl. Phys. Lett. **73** (1), 96 (1998)

[7]   B.A. Joyce *et al*., Journ. of Cryst. Growth **201/202**, 106 (1999)

[8]   T. Walther *et al*., Phys. Rev. Lett. **86** (11),2381 (2001)

[9]   D. Leonard, K. Pond and P.M. Petroff, Phys. Rev. B **50** (16), 11687 (1994)

[10]   M. Colocci *et al*., Appl. Phys. Lett. **70** (23), 3140 (1997)

[11]   D. Zhi *et al.*, Journ. of Appl. Phys. **89** (4), 2079 (2001)

[12]   N.N. Ledentsov *et al*., Phys. Rev. B **54** (12), 8743   (1996)

[13]   Q. Xie, A. A.Madhukar, P. Chen and N.P. Kobayashi, Phys. Rev. Lett. **75** (13), 2542 (1995)

[14]   J.P. McCaffrey *et al*., Journ. of Appl. Phys. **88** (5), 2272 (2000)

[15]   A. Rosenauer *et al*., Phys. Rev. B **61** (12), 8276 (2000)

[16]   O. Flebbe *et al*., J. Vac. Sci. Technol. B **17** (4), 1639 (1999)

[17]   V.A. Shchukin and D. Bimberg, Rev. Mod. Phys. **71** (4), 1123 (1999)

[18]   I. Daruka, J. Tersoff and A.-L. Barabási, Phys. Rev. Lett. **82** (13), 2753 (1999)

[19]   V.S. Shchukin, N.N. Ledentsov, P.S. Kop'ev and D. Bimberg, Phys. Rev. Lett. **75** (16), 2968 (1995)

[20]   N. Moll, M. Scheffler, E. Pehlke, Phys. Rev. B **58** (8), 4566 (1998)

[21]   D. Bimberg *et all*., Thin Solid Films **267**, p32 (1995)

[22]   P. Yu *et al*., Phys. Rev. B **60**, 16680 (1999)

[23]   K. Zhang *et al*., Appl. Phys. Lett. **76** (16), 2229 (2000)

[24]   W. Wu *et al*., Appl. Phys. Lett. **71** (8), 1083 (1997)

[25]   G.S. Solomon, J.A. Trezza and J.S. Harris, Jr., Appl. Phys. Lett. **66** (23), 3161 (1995)

[26]   N.N. Ledentsov *et al*., Semiconductors **32**, 343 (1998)

[27]   R. Nötzel, Semiconductor Science and Technology **11**, 1365 (1996)

[28]   L. Chu *et al*., Journ. of Appl. Phys. **85**, 2355 (1998)

[29]   W. Sheng and J.P. Leburton, Phys. Rev. B **63**, 161301(R) (2001)

[30]   J.M. García, J.P. Silveira and F. Briones, Appl. Phys. Lett. **77** (3), 409 (2000)

[31]   N. Liu *et al*., Phys. Rev. Lett. **84** (2), 334 (2000)

[32]   J.M. García *et al*., Appl. Phys. Lett. **71** (14), 2014 (1997)

[33]   M. Pfister, M.B. Johnson, S.F. Alvarado and H.W.M. Salemink, Appl. Phys. Lett. **67** (10), 1459 (1995)

[34]   D.M. Bruls *et al.*, Appl. Surf. Science **190** (2002) 258-263

[35]   D.M. Bruls *et al*., Appl. Phys. Lett. **81** (9), 1708 (2002)

[36]   C. Pryor *et al*., Journ. of Appl. Phys. **83** (5), 2548 (1998)

[37]   B. Grandidier *et al*., Phys. Rev. Lett. **85** (5), 1068 (2000)

[38]   L.D. Bell and W.J. Kaiser, Phys. Rev. Lett. **61** (20), 2368 (1988)
        D.L. Smith, E.Y. Lee and V. Narayanamurti, Phys. Rev. Lett. **80** (11), 2433 (1998)

[39]   O. Stier, M. Grundmann and D. Bimberg, Phys. Rev. B **59** (8), 5688 (1999)

[40]   Tersoff and Hamman, Phys. Rev. Lett. **50** (25), 1998 (1983)

[41]   W. Mönch, *Semiconductor Surfaces and Interfaces*, 3rd ed. (Springer, Heidelberg, 2001)

[42]   P.B. Joyce *et al*., Journ. of Cryst. Growth **227-228**, 1000-1004 (2001)
        P.B. Joyce *et al*., Phys. Rev. B **62** (16), 10891 (2000)

[43]   Q. Gong *et al*., Appl. Phys. Lett. **81** (10), 1887 (2002)

[44]   G.R. Bell *et al*., Phys. Rev. B **61**, R10551 (2000)

[45]   T.J. Krzyzewski *et al*., Surf. Scien. **517**, 8 (2002)

[46]   T.J. Krzyzewski *et al*., Surf. Scien. **482-485**, 891 (2001)

[47]   T.J. Krzyzewski *et al*., Phys. Rev. B **66**, 121307(R), (2002)

Chapter 8

Stacking of InAs quantum dots

8.1   Introduction

The optical and electronic properties of self-assembled dots (SADs) are strongly affected by their shape and composition [1-8]. For enhanced device properties, like low laser threshold currents, narrow luminescence line widths and improved stability upon temperature changes in quantum dot laser structures, a high uniformity of quantum dot shape, size and composition is needed. Also the density of the quantum dots has to be as high as possible in order to increase the laser output power.
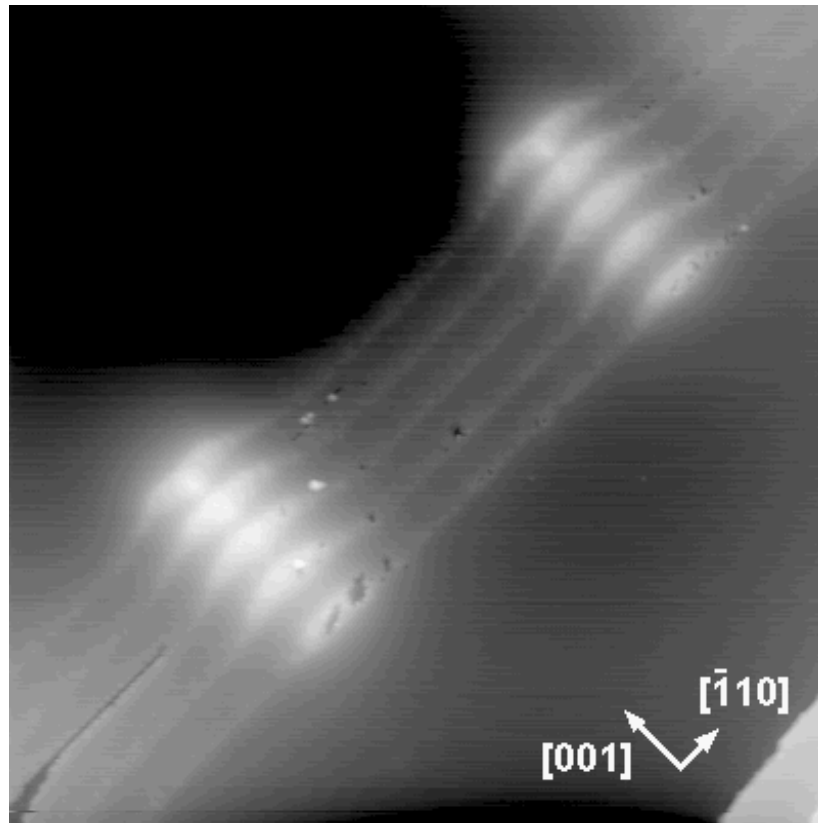
Fig. 8.1: *X-STM constant current topography image of two stacks of InAs quantum dots. Image size 150 x 150 nm^2, V_{sample} = -2.57 V, I_{tunnel} = 147 pA*

If the spacing between the quantum dot layers is sufficiently small (< 25 nm), stacks of dots are formed (see Fig. 8.1). This is due to the fact that it is energetically favorable to form a dot in the strain field of another dot as to reduce the surface free energy [8,9,11-14]. It is generally assumed that this stacking process is advantageous for enhanced quantum dot laser operation due to higher uniformity and dot number [9,10,13,15].

8.2   The sample

The investigated structures were grown by MBE by M. Hopkinson (Department of Electronic and Electrical Engineering, University of Sheffield UK) at 512°C and contained five layers of low growth rate (0.01 ML/s, 2.4 monolayer InAs per layer deposited) Stranski-Krastanov grown InAs quantum dots within a GaAs matrix. The properties of the dots in the first layer should be the same as the dots, which were investigated in the previous chapter (sample #1), as they were grown under similar conditions. The only difference was that for these dots the GaAs spacer layer was 10 nm instead of 50 nm, which resulted in coupled dots.

By investigating the X-STM current image (Fig. 8.2) the real shape and internal structure of the stacked dots become clearer. Because these current images show "the spatial derivative" of the height image, the distinction between the dot material and the surrounding GaAs matrix is enhanced. Again single indium atoms are visible outside the dots and in the wetting layer.

We observed that the internal structure is again clearly non-homogeneous (see Fig. 8.2), showing that the dots consist of an InGaAs alloy, like the quantum dots investigated in the previous chapter.
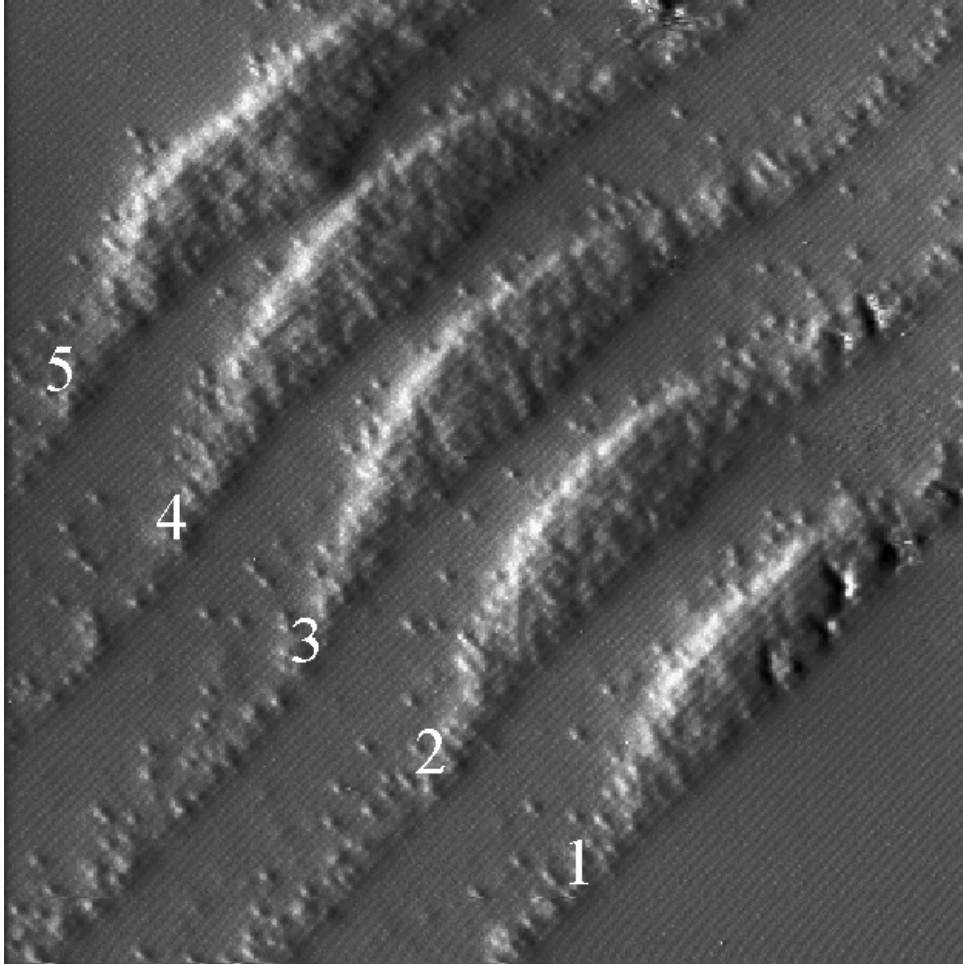
Fig. 8.2: *Cross-sectional STM current image of a stack of MBE grown (512ºC) InAs SADs in GaAs. Image size 55x55 nm². The structure contains five SAD layers formed after deposition of 2.4 ML of InAs for each SAD layer*

8.3   Lattice constant profile

The lattice constant profile of the two dots in the top of the stack has been determined in the same way as explained in chapter 5. The lattice constant increases from bottom to top inside these dots (see Fig. 8.3). This indicates that the indium concentration inside the dots increases from bottom to top, as the local lattice constant is directly linked to the local indium concentration [16-19]. The presence of an indium concentration gradient in uncoupled quantum dot layers, grown under similar conditions, was shown earlier [1,3,16]. If we compare the lattice constant profiles from Fig 8.3 with the profiles obtained from the unstacked dot in Fig. 7.10 it can be seen that the maximum lattice constant in the dot itself is equal in both cases. When comparing the lattice constants of the surrounding GaAs,

however, we see a large decrease of the GaAs lattice constant in the case of the stacked dots. This is due to the compressive strain in the GaAs in between the dots (see Fig. 7.9c and 7.10), which increases higher in the stack due to strain accumulation and a reduced thickness of the GaAs spacer layer. The growth rate of the GaAs will be strongly affected by this large compressive strain, resulting in a lower growth rate. As the strain in the dots does not seem to change in such a dramatic way as in the GaAs case, we expect these effects on the growth rate of the dot material to be much smaller in that case.
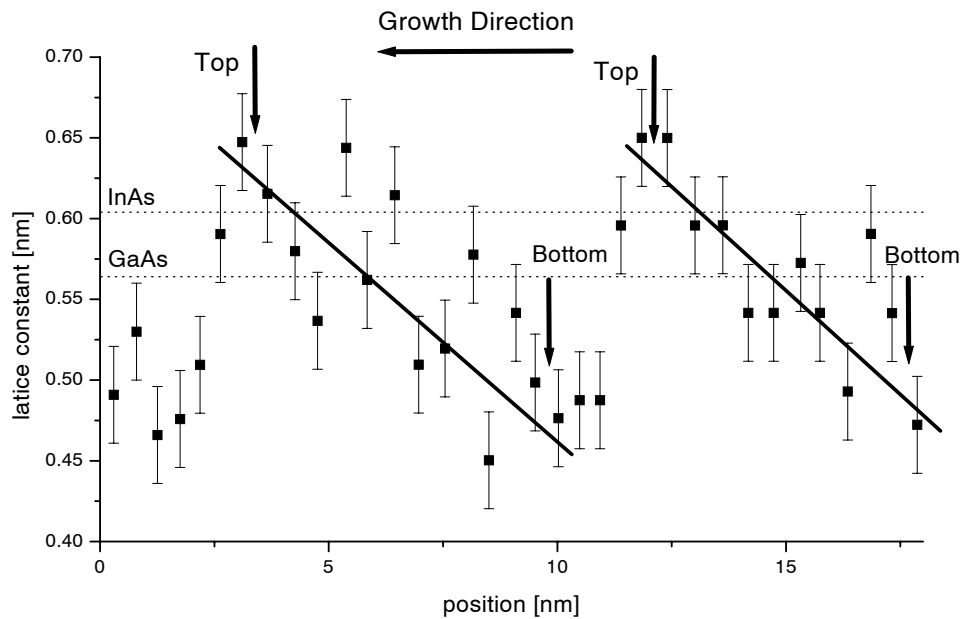
Fig. 8.3: *Lattice constant profile in the growth direction of the last two InAs quantum dots inside the stack. The top of the stack is located to the left and the bottom of the stack is located to the right of the lattice constant profile. The thick lines are drawn as a guide to the eye, to indicate the increasing lattice constant in the growth direction.*

8.4   Stack deformation: Growth rate changes

Fig. 8.2 shows that during growth the dots higher in the stack nucleate at the apex of previously buried dots, thus forming the stack [9,14,18,19]. Due to the planarization effect of the 2D GaAs growth, which tends to flatten out rough surfaces and suppresses terrace growth, the dots in the 2nd layer are formed at a position that is only shifted slightly with respect to the wetting layer. Also the dots in the 3rd and next layers grow on terraces. The growth surface before deposition of a new dot layer becomes more and more complex, resulting in a far from identical dot shape higher in the stack. Furthermore the dots in the stack are not identical. A wing shaped deformation occurs, which gets more pronounced higher in the stack. This is a strong disadvantage as dot uniformity is required for improved

device specifications. It is interesting to note that the indium segregation above the dots is less than above the wetting layer, which has to do with the fact that it is energetically more favorable for an indium atom in the top of the dot, to stay in the dot, rather than to diffuse into the highly strained GaAs.

In order to understand these effects and especially the deformation of the dot shape throughout the stack, we have investigated the thickness of the GaAs spacer layers (Fig. 8.4) and the InAs dot layers (Fig. 8.5) as function of lateral position (with respect to the center of the stack).

Fig. 8.4 shows that the GaAs spacer layer decreases in each subsequent layer up to layer 3. After layer 3 the spacer layer thickness remains constant. This must be due to the fact that the strain field of dot 1 influences the material up to spacer layer 3, so up to 30 nm. This is exactly the maximum spacer layer thickness between subsequent dot layers at which stacking will still occur (25-30 nm) [9]. After a total structure thickness of 30 nm, measured from the first dot layer, the GaAs spacer layer between all next layers will remain constant, even if more dot layers are added to the stack. It is well known that dots in a stack become uncoupled if the spacer layer is larger than 25-30 nm [9]. We propose that the reduction of the GaAs spacer layer thickness is due to the fact that the GaAs growth speed is determined by the local lateral strain. Throughout the stack the strain field of the dots, which influences the surrounding material up to 30 nm from the dot, accumulates. The higher in the stack, the larger the lattice mismatch between the strained GaAs spacer layer and free standing GaAs, resulting in a lower GaAs growth rate on top of the dots and the formation of terraces [13,14].
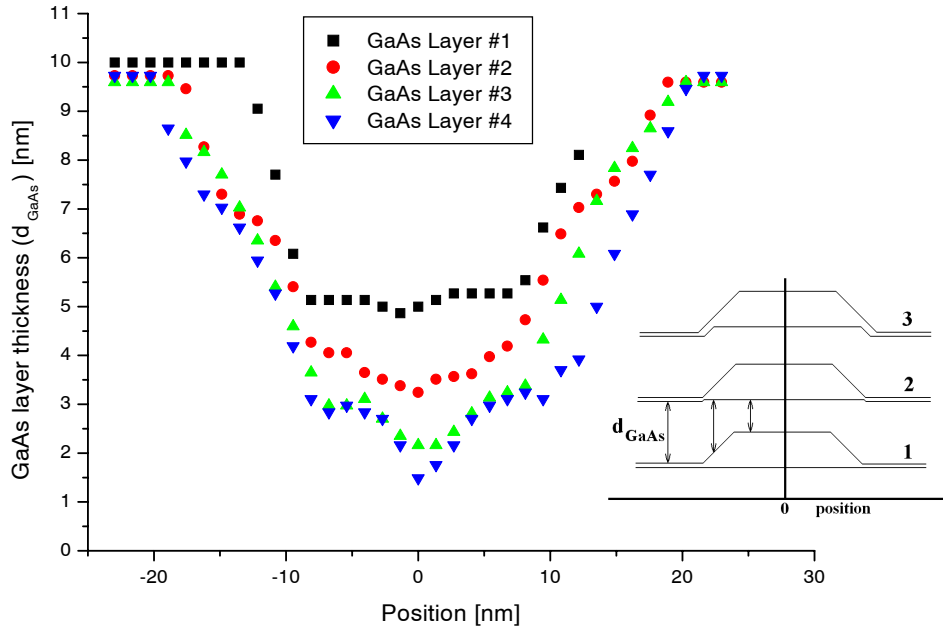

Fig 8.4: *GaAs spacer layer thickness (d_{GaAs}) throughout the stack as function of position with respect to the center of the stack*

The reduced indium segregation in between the dots can be explained in the following way. Vertical diffusion of indium from the wetting layer occurs due to the lattice mismatch between the top layer of GaAs and the InGaAs wetting layer. The diffusion of indium will try to eliminate this lattice mismatch. The GaAs spacer layer between the quantum dots, however, is heavily tensile strained, whereas in the dot material in the top of the dot the indium experiences only a mild compressive strain, see Fig 8.3. An indium atom that would diffuse from the dot to the GaAs spacer layer, would therefore give up a position that is energetically rather favorable, for a position that is highly unfavorable, i.e. an indium atom inside heavily tensile strained GaAs. Therefore the indium will remain in the top of the dot, which results in a lower indium diffusion rate above the dots [2,5].

The dot thickness profile (measured from the local position of the wetting layer up to the top of the dot) is equal in each dot layer, as is shown in Fig. 8.5. This is remarkable, considering the complex shape of the growth surface. The volume of each subsequent dot is the same, because the amount of deposited InAs is equal for all layers and the number of nucleation sites remains constant in each dot layer, assuming that the wetting layer and alloy formation is the same in all layers.
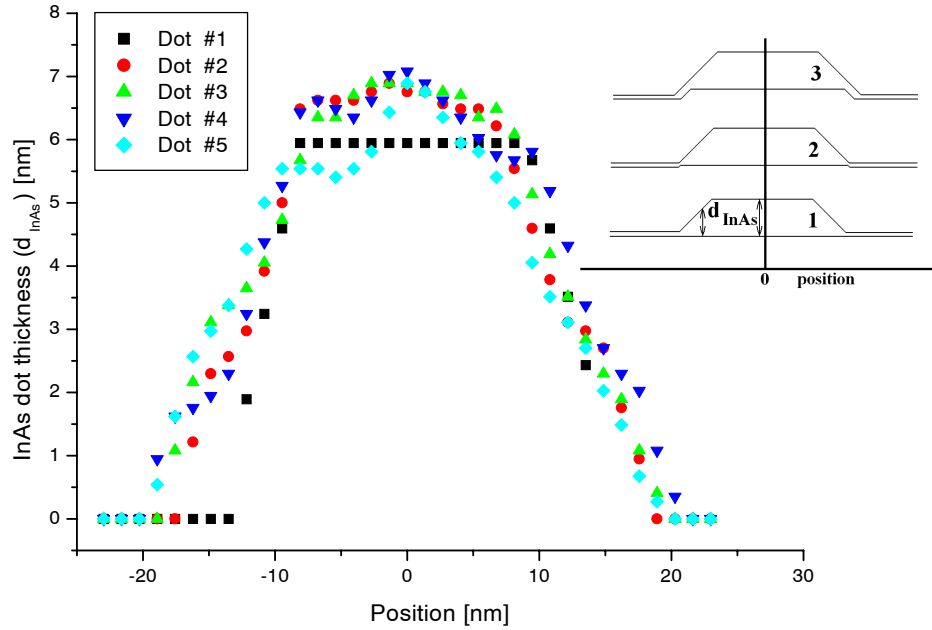

Fig. 8.5: *InAs dot thickness (d_{InAs}) throughout the stack as function of position, with respect to the center of the stack*

We therefore conclude that the deformation of the dots throughout the stack is mainly caused by the changes in the local growth rate of the GaAs spacer layer and not by the changes in local growth rate of the InAs. The GaAs growth rate is more sensitive to strain fields originating from relatively deep inside the material than the InAs dot growth rate, due

to the fact that the dots are formed in the Stranski-Krastanov growth mode, whereas GaAs is free to move across the surface during growth, making the growth of GaAs more sensitive to local strain fields.

The Stranski-Krastanov growth mode is based on the relief of built-in-strain of the wetting layer by a transition from 2D to 3D growth. The quantum dots are formed by releasing the large strain in the total wetting layer by 3D growth of the InAs islands. Although local strain fluctuations determine the position where the dots are formed, the 3D formation process of the dot seems to be mainly influenced by the total amount of material deposited, so the total amount of strain in the whole wetting layer. Small local strain fluctuations due to buried dots seem to play only a minor role in the local InAs dot growth speed. The GaAs spacer layers, however, are epitaxially (2D) grown on top of the dots. In this case, the local growth rate is very sensitive to local (in particular lateral) strain variations.

8.5   Conclusions

Reduction of the thickness of the spacer layers between dot layers (<25 nm) results in the formation of stacks of quantum dots. The investigated dots in the stacks consist of an InGaAs alloy in which an indium gradient is present, similar to sample #1 (M1640) from the previous chapter. This was confirmed by lattice constant profiles across the center of the stack.

During the formation of the stack, the dots in the stack get deformed. This deformation gets worse higher in the stack and results in wing shaped dots that grow on terraces. From the determination of the dot growth rate and the GaAs spacer layer growth rate throughout the entire stack, it was shown that the deformation of the dots is caused by changes in the GaAs spacer layer growth rate, rather than by changes in the InAs growth rate. This is probably due to the fact that the 2D GaAs growth is very sensitive to local (lateral) strain variations, whereas the 3D dot growth appears only to be dependent on the total amount of deposited material. The volume of the dots throughout the stack remains the same as the amount of material and the number of nucleation sites is the same for all dot layers.

References

[1]   P.W. Fry *et al*., Phys. Rev. Lett. **84** (4), 733 (2000)

[2]   A. Rosenauer *et al*., Phys. Rev. B **61** (12), 8276 (2000)

[3]   J.A. Barker and E.P. O'Reilly, Phys. Rev. B **61** (20), 13840 (2000)

[4]   P.B. Joyce *et al*., Phys. Rev. B **58** (24), 15981 (1998)

[5]   Kegel *et al*., Phys. Rev. Lett. **85** (8), 1694 (2000)

[6]   B. Grandidier *et al*., Phys. Rev. Lett. **85** (5), 1068 (2000)

[7]   D. Zhi *et al*., Journ. of Appl. Phys. **89** (4), 2079 (2001)

[8]   F. Heinrichsdorff *et al*., Appl. Phys. Lett. **71** (1), 22 (1997)

[9]   Q. Xie, A. A.Madhukar, P. Chen and N.P. Kobayashi, Phys. Rev. Lett. **75** (13), 2542 (1995)

[10]   J. Tersoff, C. Teichert and M.G. Lagally, Phys. Rev. Lett. **76** (10), 1675 (1996)

[11]   W. Wu, J.R. Tucker, G.S. Solomon and J.S. Harris Jr., Appl. Phys. Lett. **71** (8), 1083 (1997)

[12]   H. Eisele *et al*., Appl. Phys. Lett. **75** (1), 106 (1999)

[13]   N.N. Ledentsov *et al*., Phys. Rev. B **54** (12), 8743 (1996)

[14]   B. Legrand *et al*., Appl. Phys. Lett. **74** (18), 2608 (1999)

[15]   O.G. Schmidt *et al*., Electron. Lett. **32**, 1302 (1996)

[16]   D.M. Bruls *et al.*, Appl. Phys. Lett. **81** (9), 1708 (2002)

[17]   O. Flebbe *et al*., J. Vac. Sci. Technol. B, **17** (4), 1639 (1999)

[18]   B.Legrand *et al*., Appl. Phys. Lett. **73** (1), 96 (1998)

[19]   H. Eisele, O. Flebbe, T. Kalka and M. Dähne-Prietsch, Surf. and Interf. Anal. **27**, 537 (1999)

Summary

By means of modern epitaxial growth techniques it is possible to fabricate semiconductor structures that are faster, cheaper and more complicated. They find their implementation in e.g. quantum dot or quantum well lasers. To obtain extra functionality, these devices have to be made so small, that within these structures charge carriers are confined in 2 or 3 dimensions. This results in discrete energy levels, which enable new applications and may solve several problems in the contemporary technologies. The first chapter will give an introduction in which is explained why cross-sectional Scanning Tunneling Microscopy (X-STM) is a very suitable technique to investigate semiconductor nanostructures, as nanostructures can be investigated at the atomic level by this technique. The differences in the chemical and electrical properties of the various species of atoms, of which the semiconductor materials consist of, can be used to discriminate between them. This can be used to obtain a better insight in the way these structures work. Furthermore, the growth processes involved in the fabrication of these structures can be better understood and optimised.

In chapter 2, a short description of two epitaxial growth techniques, Molecular Beam Epitaxy (MBE) and Chemical Beam Epitaxy (CBE) is given. The differences, the advantages and disadvantages of these growth techniques are briefly discussed. Also a method is discussed by which a desired bandgap of the semiconductor can be obtained by choosing the proper materials. Furthermore, the formation of 3D structures by Stranski-Krastanov growth is briefly described. By growing materials with a different lattice constant on top of each other, strain can be introduced in the material. This strain influences the electronic band structure and can therefore be used to modify the band structure of a semiconductor as desired.

During STM measurements the local density of states of the surface is imaged. Also the density of states of the STM tip plays a very important role in the imaging mechanism. Not only the topography of the surface under investigation, but also the electronic properties of both the surface and the tip have a large influence on the STM image. The big question therefore often remains: what is actually imaged during an STM measurement? Therefore the tunnel process needs some extra consideration, in order to be able to interpret the STM images in a proper way. In chapter 3, the tunnel process and the influence of the STM tip are described in more detail. Also the possibility of imaging the wavefunctions at the surface of a semiconductor, using I(V) spectroscopy during STM measurements, is briefly explained. Furthermore, the influence of bandbending upon the tunnel current is dealt with. After that the behaviour of a cleaved surface is described, as the outermost atoms of a surface, which are probed during STM measurements, behave in a different way than the atoms in the bulk material. Finally, the relaxation of cleaved surfaces is treated. If in a structure a strained 2D layer, like a quantum well, is present, this layer will relax outward or inward, after it has been cleaved perpendicular to this layer. By investigation of the resulting relaxation profile, the concentration profile inside the layer can be calculated in an analytical way.

In chapter 4, the used experimental methods are given. The STM unit itself and the ultrahigh vacuum system with active damping system are described. Also the procedures

followed during tip- and sample preparation are given some closer attention. Finally a short description of how STM and spectroscopy measurements are performed is given.

In a semiconductor structure, layers with a different lattice constant can be grown on top of each other. This results in strain in the structure. If such a structure is cleaved, this strain will cause a relaxation of the surface. By analysing this relaxation the concentration profile of these layers can be determined. Therefore an exact determination of this relaxation is necessary. During STM measurements, not only topography, but also an electronic component is imaged. In order to be able to separate these two contributions, the height contrast in STM measurements is investigated in detail in chapter 5. Numerical calculations have been performed in order to investigate the electronic contrast as a function of applied tunnel voltage, for an InGaAs layer in a GaAs matrix. From these calculations it has become clear that at high tunnel voltages the electronic contrast can be suppressed very effectively, especially when imaging the filled electron states. These simulations have been compared with measurements that have been performed on an InGaAs quantum well. From voltage dependent measurements it has been concluded that the conclusions from the numerical simulations are indeed correct. It is thus possible to obtain STM images that only contain topographical information. From relaxation and lattice constant profiles obtained from such images, it is possible to determine the concentration profile, by using the theory from chapter 3. The concentration profile of the investigated quantum well has been accurately determined by X-ray diffraction, photoluminescence measurements and by counting atoms in STM images. By comparing the used analytical model with these measurements, it is shown that they agree. Several causes can be indicated for the fact that the calculations do not agree 100% with the measurements.

In modern telecommunications there is a large demand for lasers that operate in the 1.3 and 1.55 μm wavelength range. InGaAsN compounds, which can be grown on InP without introducing any strain, are very interesting in this respect. They can be used in e.g. Vertical Cavity Surface Emitting Lasers (VCSEL) and very efficient solar cells. InGaAsN and InGaAs layers have been investigated by X-STM and have been compared to each other in chapter 6. The nitrogen atoms are clearly visible in the InGaAsN layers, and the formation of pairs of nitrogen atoms is observed. From the STM measurements the nitrogen concentration is estimated to be about 1.2%. After a thermal treatment, nitrogen rich clusters are formed, which behave like quantum dots. The existence of such quantum dots has already been expected from optical measurements that have been performed on similar annealed structures. By suppression of the electronic contrast, images have been obtained that show only real topographic information. From the relaxation profile the presence of nitrogen in the InGaAsN layers is demonstrated. Furthermore, they show that after annealing, when the nitrogen quantum dots have been formed, the remaining InGaAsN layer is almost completely depleted from nitrogen. Finally, the influence of extreme annealing temperatures is investigated. Both the InGaAs as the InGaAsN layers are damaged by this and no quantum dot formation takes place.

The optical and electrical properties of quantum dots are dependent on their shape, size and composition. If quantum dots are covered with another material, their structural properties will change. Therefore it is necessary to investigate buried dots as well, and not only dots that are uncovered. In chapter 7, the dimensions and the shape of InAs quantum dots within a GaAs matrix have been determined. These dots were grown at an extremely low growth rate, i.e. 0.01 monolayer/sec. As one cannot tell from an STM image at which position the dot has been cleaved, the height vs. base length distribution of an ensemble of quantum dots has been determined. From this it is deduced that the dots have the shape of a truncated

pyramid, with a base length of 18 nm and a height of 5 nm. This is in agreement with previous optical measurements and theoretical calculations. By measuring the outward relaxation and the lattice constant profile of the cleaved dot, the concentration profile inside the dot was determined by numerical simulations. In the dots a linear indium gradient from 60% to 100% from bottom to top is present, which is again in agreement with previous optical measurements. By means of Current Imaging Tunneling Spectroscopy (CITS) it was attempted to image the wavefunction of the electrons that are confined within the cleaved dot. This was not possible for the "holes" in the quantum dots. By using a numerical model it is possible to simulate the CITS measurements (current distribution) for the electron wavefunctions. In the model, the shape, the composition, the fact that the dot is cleaved, the strain fields and the band bending underneath the tip are taken into account. By means of these simulations, a better insight is obtained in the energy separation of the various electron states and the positions of the maxima in the CITS measurements. Next, samples were investigated that contained InAs quantum dots grown at a much larger growth rate (0.1 monolayer/sec). In this sample the amount of deposited InAs per quantum dot layer was varied as well. After deposition of 1.5 monolayers of InAs, no quantum dot formation was observed. After the deposition of 2.0 and 2.5 monolayers of InAs, however, quantum dots had been formed. Although the 2.5 monolayer quantum dots are slightly larger than the 2.0 monolayer dots, the larger deposition amount of InAs meanly leads to a higher dot density, rather than larger dots. These dots are lens-shaped and thus do not have the shape of a truncated pyramid. This is due to the higher deposition rate, which leads to a larger aspect ratio of the dots before they are capped with GaAs. This also causes that the dots do not have an indium gradient, which results in dots that consist of InGaAs with a constant indium concentration. This has been determined from the relaxation profiles of the cleaved quantum dots. Even at deposition amounts that are smaller than 1.7 monolayers, which is the critical layer thickness, dot nucleation centers can already be formed due to inhomogeneities at the growth surface. This results in small quantum dots that consist of almost pure InAs. The density of these dots is, however, very low. Finally, the formation of the wetting layers has been studied. From relaxation profiles of the wetting layer between the quantum dots, it is concluded that the wetting layer does not change if the amount of deposited InAs is enlarged. After formation of the wetting layer, i.e. after the deposition of 1.7 monolayers of InAs, the wetting layer remains stable and all the surplus of material is incorporated in the quantum dots. By means of the relaxation profile and numerical calculations, the width and composition profile of the wetting layer has been determined. The width found in these calculations agrees well with the width that is observed in the X-STM measurements. The indium concentration seems to decrease exponentially in the growth direction. Furthermore, the calculated average indium concentration inside the wetting layer is exactly what one would expect if 1.7 monolayers of InAs are incorporated in a layer with the calculated and observed thickness.

Finally, stacks of quantum dots have been investigated in chapter 8. If the distance between the quantum dot layers is not too large (< 25 nm), the quantum dots will form on top of each other, thus forming a stack. This is an advantage, as in this way the local dot density can be enlarged. From these dots, a higher uniformity is expected as well. From lattice constant profiles it was concluded that these dots have a similar indium concentration profile as the low-growth-rate quantum dots from chapter 7, which is hardly surprising, as the growth conditions were almost identical. Several stacks of quantum dots have been investigated by X-STM. Higher in the stack, the quantum dots get deformed, as the dots become more wing-shaped and terrace growth occurs. From analysis of the growth speed of

the quantum dot material and the surrounding GaAs matrix it is concluded that the deformation is caused by changes in growth speed of the GaAs matrix. This is due to the fact that the 2D GaAs growth is very sensitive to local lateral strain fluctuations. Furthermore, the growth speed of the InAs quantum dot material remains constant throughout the entire stack. This results in quantum dots that all have the same volume in spite of the deformation. Therefore the consequences of the deformation upon the opto-electronic properties of the dots are expected to be small.

Nederlandse samenvatting

Met behulp van moderne epitaxiale groeitechnieken is het mogelijk steeds snellere, goedkopere en gecompliceerdere halfgeleiderstructuren te maken. Deze vinden hun toepassing in bijvoorbeeld quantum doos of quantum put lasers. Om extra functionaliteit te verkrijgen moeten deze halfgeleiderstructuren zó klein gemaakt worden dat lading in deze structuren in 2 of 3 dimensies wordt opgesloten. Dit leidt tot discrete energieniveaus, waardoor nieuwe toepassingen mogelijk zijn en zo diverse problemen van de huidige technologieën kunnen worden opgelost. Het eerste hoofdstuk van dit proefschrift geeft een inleiding waarom cross-sectionele Scanning Tunneling Microscopie (X-STM) een zeer geschikte techniek is om deze halfgeleidernanostructuren nader te bestuderen. Met behulp van STM kunnen immers nanostructuren op atomair niveau worden onderzocht. Het verschil in elektrische en chemische eigenschappen van de diverse halfgeleidermaterialen kan worden gebruikt om de verschillende atoomsoorten, waaruit deze materialen zijn opgebouwd, van elkaar te onderscheiden. Dit leidt tot een beter inzicht in het precieze functioneren van deze structuren. Ook kunnen groeiprocessen geoptimaliseerd en beter begrepen worden.

In hoofdstuk 2 wordt een korte beschrijving gegeven van twee epitaxiale groeitechnieken, namelijk Molecular Beam Epitaxy (MBE) en Chemical Beam Epitaxy (CBE). De verschillen tussen en de voor- en nadelen van deze groeitechnieken worden kort besproken. Verder wordt de wijze beschreven waarop door de juiste materiaalkeuze, de gewenste bandgap van halfgeleiders kan worden verkregen. Ook wordt de vorming van 3D structuren tijdens Stranski-Krastanov groei kort behandeld. Door materialen met verschillende roosterconstantes op elkaar te groeien kan er spanning in het materiaal gebracht worden. Deze spanning heeft invloed op de elektronische bandstructuur van de halfgeleider en kan gebruikt worden om de bandstructuur van een halfgeleider naar wens te modificeren.

Tijdens STM metingen wordt de lokale toestandsdichtheid van het oppervlak afgebeeld. Ook de toestandsdichtheid van de STM tip speelt hierbij een prominente rol. Naast de topografie van het oppervlak hebben ook de elektronische eigenschappen van het oppervlak en de tip een grote invloed op het STM beeld. De grote vraag blijft dan ook vaak: wat wordt er eigenlijk precies in een STM meting afgebeeld? Daarom is voor een juiste interpretatie van STM metingen een nadere beschouwing van het tunnelproces noodzakelijk. In hoofdstuk 3 wordt het tunnelproces en met name de invloed van de tip in meer detail beschreven. Ook wordt in het kort uitgelegd hoe met behulp van STM tijdens I(V)-spectroscopie de golffuncties aan het oppervlak van een halfgeleider kunnen worden afgebeeld. Verder wordt de invloed van bandverbuiging en de invloed hiervan op de tunnelstroom kort toegelicht. Daarna wordt het gedrag van een gekliefd oppervlak behandeld. De buitenste atomen van een gekliefd oppervlak, waarop de STM metingen worden uitgevoerd, gedragen zich immers anders dan atomen in de bulk. Tenslotte wordt de relaxatie van gekliefde oppervlakken behandeld. Indien in een structuur een 2D laag aanwezig is, zoals een quantum put die onder spanning staat, dan zullen deze lagen na loodrecht op de laag gekliefd te zijn naar binnen of buiten relaxeren. Aan de hand van het resulterende relaxatieprofiel is door middel van berekening het concentratieprofiel in deze laag op een analytische manier te bepalen.

In hoofdstuk 4 worden de gevolgde experimentele procedures behandeld. Er wordt een beschrijving gegeven van de STM eenheid en het ultra hoog vacuüm systeem met actief dempingsysteem. Ook worden de procedures, die gevolgd worden bij de preparaat- en tippreparatie, nader toegelicht. Tenslotte wordt kort beschreven hoe STM en spectroscopie metingen in de praktijk in zijn werk gaan.

In een halfgeleiderstructuur kunnen lagen met verschillende roosterconstantes op elkaar worden gegroeid. Dit leidt tot spanning in deze lagen. Indien een dergelijke structuur wordt gekliefd treedt er tengevolge van deze spanning een relaxatie op van het oppervlak. Aan de hand van deze relaxatie is het mogelijk het concentratieprofiel in deze lagen te bepalen. Hiervoor is het wel noodzakelijk dat deze relaxatie exact kan worden bepaald. Bij STM metingen wordt echter naast de topografie ook een elektronische component afgebeeld. Om deze topografische en elektronische bijdragen van elkaar te kunnen scheiden is in hoofdstuk 5 het hoogtecontrast in STM metingen nader onderzocht. Er zijn numerieke simulaties uitgevoerd om het elektronisch contrast als functie van de aangelegde tunnelspanning te onderzoeken voor een InGaAs laag in een GaAs matrix. Bij hoge tunnelspanningen kan men, volgens deze simulatie, de elektronische bijdrage effectief onderdrukken, met name als men de gevulde elektrontoestanden afbeeldt. Deze simulaties zijn vergeleken met metingen op een InGaAs quantum put. Uit spanningsafhankelijke metingen blijkt dat de conclusies, die getrokken zijn uit de numerieke simulaties, correct zijn. Het is dus mogelijk STM beelden te verkrijgen die alleen maar topografische informatie bevatten. Met de hieruit verkregen profielen van de relaxatie en de roosterconstante kan men nu met behulp van de theorie uit hoofdstuk 3 het concentratieprofiel bepalen. Het concentratieprofiel in de onderzochte quantum put is nauwkeurig bepaald met behulp van X-Ray diffractie, fotoluminescentiemetingen en door atomen in de STM beelden te tellen. Door het gebruikte analytische model en de meting met elkaar te vergelijken blijkt er redelijke overeenstemming te zijn tussen de gemeten en berekende profielen. De berekeningen blijken niet 100% met de metingen overeen te stemmen, maar hiervoor zijn diverse oorzaken aan te wijzen.

In de moderne telecommunicatie is er vraag naar lasers die werken in het golflengte gebied tussen 1.3 en 1.55 μm. InGaAsN verbindingen, die zonder interne spanningen gegroeid kunnen worden op InP, zijn hierbij interessante kandidaten. Zij kunnen o.a. gebruikt worden in Vertical Cavity Surface Emitting Lasers (VCSEL) en hoge-rendement-zonnecellen. In hoofdstuk 6 is een dergelijke structuur onderzocht. InGaAsN en InGaAs lagen zijn met X-STM onderzocht en met elkaar vergeleken. Inderdaad is de stikstof zichtbaar in de InGaAsN lagen en treedt er paarvorming van stikstofatomen in de laag op. De stikstofconcentratie in de onderzochte structuur die bepaald is aan de hand van de STM metingen bedraagt ongeveer 1.2%. Nadat de structuur een warmtebehandeling heeft gehad blijken er stikstofclusters te zijn gevormd, die zich gedragen als quantum doosjes. Het bestaan van deze quantum doosjes was al eerder vermoed aan de hand van optische metingen aan gelijksoortige warmtebehandelde preparaten. Door het elektronische contrast te onderdrukken zijn X-STM metingen van de lagen verkregen die alleen het topografische contrast tonen. Uit de relaxatie profielen blijkt dat in de onbehandelde InGaAsN laag inderdaad stikstof aanwezig is en dat de warmtebehandeling leidt tot quantum-doos-vorming, waarna de rest van de laag de structuur en het relaxatieprofiel heeft van een InGaAs laag zonder stikstof. Tenslotte is de invloed onderzocht van een extra hoge temperatuur tijdens de warmtebehandeling. Alle lagen, zowel de InGaAs als de InGaAsN lagen worden hierdoor beschadigd en er treedt geen vorming van quantum doosjes op.

De vorm, afmetingen en samenstelling van quantum doosjes hebben een grote invloed op hun elektronische en optische eigenschappen. Indien quantum doosjes worden bedekt met een ander materiaal veranderen hun structurele eigenschappen, zodat het nodig is ook de bedekte quantum doosje te onderzoeken, en niet alleen onbedekte structuren. In hoofdstuk 7 zijn met behulp van X-STM de vorm en afmetingen bepaald van InAs quantum doosjes in een GaAs matrix . De groeisnelheid tijdens de fabricage van deze structuren was erg laag, namelijk 0.01 monolaag/sec. Aangezien men bij een X-STM afbeelding van een quantum doosje niet weet op welke positie er door het quantum doosje is gekliefd, hebben wij de distributie van de hoogte versus de basislengte van een ensemble gekliefde quantum doosjes bepaald. Aan de hand hiervan is vastgesteld dat de quantum doosjes de vorm hebben van een afgeknotte piramide, met een basislengte van 18 nm en een hoogte van 5 nm. Dit is in overeenstemming met eerder uitgevoerde optische metingen en theoretische berekeningen. Aan de hand van relaxatie- en roosterconstanteprofielen van de quantum doosjes is het verloop van de indiumconcentratie in de quantum doosjes bepaald. Dit is gedaan aan de hand van numeriek gesimuleerde relaxatie- en roosterconstanteprofielen. Er blijkt een lineair verloop van het profiel van de indium concentratie, van 60% naar 100% indium van basis naar top, in de quantum doosjes aanwezig te zijn. Dit is wederom in overeenstemming met eerdere optische metingen en de interpretatie hiervan. Ook is door middel van Current Imaging Tunneling Spectroscopy (CITS) metingen getracht de golffunctie van de elektronen die opgesloten zitten in deze gekliefde quantum doosjes af te beelden. Voor de "gaten" in de quantum doosjes is dit niet mogelijk gebleken. Met een numeriek rekenmodel is het mogelijk de CITS metingen (de stroomdistributie) voor elektron golffuncties te simuleren. In het numerieke model zijn de vorm, de compositie, het feit dat het quantum doosje is gekliefd, de spanningsvelden en de bandverbuiging onder de tip meegenomen. De separatie tussen de diverse elektrontoestanden en de posities van de maxima in de CITS metingen kunnen aan de hand van de simulaties beter begrepen worden. Vervolgens zijn preparaten met daarin InAs quantum doosjes die zijn gegroeid op een veel hogere groeisnelheid (0.1 monolaag/sec) onderzocht. In dit preparaat is ook de totale hoeveelheid InAs die gedeponeerd is gevarieerd. Bij een depositie van slechts 1.5 monolagen InAs treedt geen formatie van quantum doosjes op. Bij depositie van 2.0 en 2.5 monolagen treedt dit wel op. Alhoewel de 2.5 monolagen quantum doosjes iets grotere afmetingen hebben dan de 2.0 monolagen quantum doosjes, leidt een hogere InAs depositiehoeveelheid vooral tot de formatie van een extra hoeveelheid quantum doosjes. Deze quantum doosjes hebben de vorm van een lens, en niet van een afgeknotte piramide. Dit komt door de hogere depositie snelheid, die leidt tot een grotere breedte-hoogte verhouding voordat de quantum doosjes worden bedekt met GaAs. Dit heeft ook tot gevolg dat er in deze quantum doosjes geen verloop van de indium concentratie is, maar dat deze bestaan uit InGaAs met constante samenstelling. Dit is wederom vastgesteld aan de hand van relaxatieprofielen gemeten over de gekliefde quantum doosjes. Ook bij depositie van minder dan de kritische laagdikte van 1.7 monolagen InAs kan er ten gevolge van oppervlakteinhomogeniteiten tijdens de groei al kiemvorming van quantum doosjes optreden. Dit resulteert in zeer kleine quantum doosjes van vrijwel puur InAs. De dichtheid hiervan is echter uiterst laag. Tenslotte is de vorming van de InAs "wetting" laag onderzocht. Uit de relaxatieprofielen van de wetting lagen tussen de quantum doosjes blijkt dat de wetting lagen niet veranderen als de InAs depositiehoeveelheid wordt verhoogd. De wetting laag blijft na vorming dus stabiel, i.e. na depositie van 1.7 monolagen InAs. Na de vorming van de wetting laag gaat al het extra materiaal naar de quantum doosjes toe. Aan de hand van de relaxatie profielen is, door middel van berekening, de breedte en het

compositieprofiel van de wetting lagen bepaald. De breedte van de wetting laag die resulteert uit deze fit komt overeen met de X-STM afbeeldingen van deze lagen en de indium concentratie in de wetting laag blijkt exponentieel af te nemen in de groeirichting. Verder komt de gemiddelde indium concentratie in de wetting laag exact overeen met de depositie van 1.7 monolagen InAs in een laag met de berekende dikte en zoals waargenomen in de X-STM metingen.

Tenslotte zijn in hoofdstuk 8 stapels van quantum doosjes onderzocht. Indien de afstand tussen de opeenvolgende lagen niet te groot is (< 25 nm), zullen de quantum doosjes boven elkaar gevormd worden en een stapel vormen. Dit heeft voordelen, omdat hiermee lokaal de hoeveel quantum doosjes in een preparaat kan worden vergroot. Ook wordt een hogere uniformiteit van de quantum doosjes verwacht. Uit profielen van de roosterconstante blijkt dat deze quantum doosjes hetzelfde indium concentratieprofiel hebben als de lage-groei-snelheid quantum doosjes uit hoofdstuk 7. Dit is niet verwonderlijk, omdat de groeiomstandigheden nagenoeg identiek zijn. Verschillende stapels van quantum doosjes zijn met de X-STM onderzocht. Het blijkt dat de quantum doosjes hoger in de stapel vervormen. Er treedt een vleugel vormige deformatie en terras groei op. Uit analyse van de groeisnelheden van de InAs quantum doosjes en de GaAs tussenlagen is gebleken dat deze deformatie wordt veroorzaakt door veranderingen in de groeisnelheid van de GaAs tussenlagen. Dit komt omdat de 2D GaAs groei zeer gevoelig is voor lokale laterale spanningen in het materiaal. Verder blijkt dat de groeisnelheid van de InAs quantum doosjes constant is voor iedere laag in de stapel. Dit betekent dat de quantum doosjes, ondanks de vervormingen, allemaal hetzelfde volume hebben, zodat de gevolgen van deze deformatie op de elektro-optische eigenschappen van de quantum doosjes naar verwachting niet al te groot zullen zijn.

"op maat" en hulp bij al mijn "groei gerelateerde" struikelblokken. Verder wil ik Maarten Leys bedanken voor onze nuttige discussies, het groeien van de nitride samples en onze vaak komisch-interessante gesprekken aan de koffietafel.

Zonder technische ondersteuning is het als AIO onmogelijk onderzoek naar behoren te verrichten. Vandaar wil ik Jos van Ruyven bedanken voor het verlichten van al mijn "vacuum-leed", Frans van Setten voor het repareren van al onze kapotte controllers, Rian Hamhuis voor het groeien van diverse preparaten en Tom Eijkemans voor het doen van de PL en XRD metingen. Ook Peter Nouwens mag hierbij niet ontbreken. Zijn opgedampte contacten waren altijd prima!

Natuurlijk mogen mijn kamergenoten niet ontbreken in dit dankwoord: Andrei Yakunin en Peter Offermans. Bedankt voor de goede sfeer en samenwerking. Ik weet zeker dat de STM bij jullie in goede handen is. Veel succes met jullie onderzoek! Ook Martijn Kemerink, die helaas onze kamer moest ontvluchten wegens overbevolking, moet genoemd worden vanwege zijn kritisch oog, immer bruikbare feedback en zijn aparte gevoel voor humor. Verder wil ik alle HGF-ers bedanken voor hun gezelligheid, steun en advies. Ik zal altijd met veel plezier terugkijken op mijn tijd bij HGF!

Tenslotte wil ik mijn ouders, schoonouders, Richard, Marianne, Maurice en al mijn vrienden bedanken voor hun steun de afgelopen jaren. Alhoewel ik er niet altijd in slaagde om precies duidelijk te maken wat ik nu eigenlijk de hele dag deed op die TU/e, kon ik altijd op een luisterend oor rekenen. Maar mijn grootste steun en toeverlaat was natuurlijk Karin, aan wie ik dan ook mijn proefschrift opdraag. Al die verhalen over fysica en dat 4 jaar lang…… Bedankt dat je er altijd voor me bent!

Dominique

List of Publications

D.M. Bruls, P.M. Koenraad, M.R. Leys, H. Vonk and J.H. Wolter: *InGaAsN quantum dot formation in InP by Rapid Thermal Annealing observed by X-STM*, submitted for publication in Applied Physics Letters

P.M. Koenraad, D.M. Bruls, J.H. Davies, S.P.A. Gill, Fei Long, M. Hopkinson, M.S. Skolnick, J.H. Wolter: *Composition profiling at the atomic scale in III-V nanostructures by cross-sectional STM*, accepted for publication Physica E (2002)

D.M. Bruls, J.W.A.M. Vugs, P.M. Koenraad, H.W.M. Salemink, J.H. Wolter, M. Hopkinson, M.S. Skolnick, Fei Long and S.P.A. Gill: *Determination of the shape and indium distribution of low-growth-rate InAs quantum dots by cross-sectional scanning tunneling microscopy*, Applied Physics Letters Vol. 81 (9), 1708 (2002)

G.J. de Raad, D.M. Bruls, P.M. Koenraad, J.H. Wolter: *Interplay between tip-induced band bending and voltage-dependent surface corrugation on GaAs(110) surfaces*, Physical Review B Vol. 66, 195306 (2002)

John. H. Davies, D.M. Bruls, J.W.A.M. Vugs and P.M. Koenraad: *Relaxation of a strained quantum well at a cleaved surface*, Journal of Applied Physics, Vol. 91, Number 7 (2002)

D.M. Bruls, P.M. Koenraad, M. Hopkinson, J.H. Wolter, H.W.M. Salemink: *Determination of the outward relaxation of cleaved strained InAs structures by scanning tunneling microscopy*, Applied Surface Science 190 (2002) 258-263

M. Kemerink, T.C.G. Reusch, D.M. Bruls, P.M. Koenraad, H.W.M. Salemink and J. H. Wolter:
Quantitative determination of the charge density on surface steps on semiconductors by high-resolution local scanning-tunneling spectroscopy, Physica E, Volume 13, Issues 2-4, Pages 1159-1162 (2002)

D.M. Bruls, P.M. Koenraad, H.W.M. Salemink and J.H. Wolter: *Investigation of the properties of InAs quantum dots at the atomic level by cross-sectional STM*, oral presentation by D.M. Bruls, 29th Conference on The Physics and Chemistry of Semiconductor Interfaces PCSI-29, Santa Fe, U.S.A. (2002)

P.M. Koenraad, D.M. Bruls, P. Offermans, J.H. Davies, J.H. Wolter "*Composition profiling of III-V Nanostructures using cross-sectional STM*", oral presentation by P.M. Koenraad and Proceedings NANO-7/ECOSS-21, Malmo, Sweden, FR-R-002 (2002)

D.M. Bruls, P.M. Koenraad, J.H. Davies, S.P.A. Gill, Fei Long, M. Hopkinson, M. Skolnick, J.H. Wolter, J.T. Devreese "*Direct composition profiling in III-V nanostructures by cross-sectional STM*", oral presentation by P.M. Koenraad and

Proceedings of the 26th International Conference on the Physics of Semiconductors, Edinburgh, United Kingdom (2002), edited by J.H. Davies and A.R. Long

D.M. Bruls, J.W.A.M. Vugs, P.M. Koenraad, M.S. Skolnick, M. Hopkinson, J.H. Wolter: *Cracking self-assembled InAs quantum dots*, Applied Physics A 72 [Suppl.], S205-S207 (2001)

G.J. de Raad, D.M. Bruls, P.M. Koenraad and J.H. Wolter: *STM observation of GaAs (110) showing the top and bottom zig-zag rows of the surface*, Physical Review B, Vol. 64, 075314 (2001)

D.M. Bruls, P.M. Koenraad, M.S. Skolnick, M.Hopkinson and J.H. Wolter: *Determination of the shape and composition of InAs quantum dots at the atomic level by cross-sectional STM*, oral presentation by D.M. Bruls, 8th International Conference on the Formation of Semiconductor Interfaces, Saporro, Japan (2001)

D.M. Bruls, J.W.A.M. Vugs, P.M. Koenraad, M.S. Skolnick,, M. Hopkinson, and J.H. Wolter, "*Shape analysis of single and stacked InAs quantum dots at the atomic level by cross-sectional STM*", oral presentation by P.M. Koenraad and Proceedings of the 25th International Conference on the Physics of Semiconductors, 22-27 September 2000, Osaka, Japan, edited by N. Miura and T.Ando, Springer Verlag, Berlin, 359-360 (2001)

D.M. Bruls, P.M. Koenraad, T. Reusch, M. Kemerink, M. Hopkinson, M.S. Skolnick,, F. Long, S.P.A. Gill, J.H. Wolter, H.W.M. Salemink, "*Determination of the shape and composition of InAs quantum dots at the atomic level by cross-sectional STM*", oral presentation by P.M. Koenraad and Proceedings 11th International Conference on Scanning Tunneling Microscopy/ Spectroscopy and Related Techniques, Vancouver, Canada, 96 (2001)

M. Silova, D.M. Bruls, A. Yu Silov, B.H.V. Roy, E. Smalbrugge, F. Karouta, P.M. Koenraad, J.H. Wolter: *Dynamic scaling of plasma etched InP surface*, Conference Proceedings. 2000 International Conference on Indium Phosphide and Realated Materials (Cat. No. 00CH37107) p. 201-4 (2000)

G.J. de Raad, D.M. Bruls, P.M. Koenraad, and J.H. Wolter *"Tunability of the surface-corrugation on GaAs/AlGaAs (110) surfaces"*, proceedings of the 10th International Conference on Scanning Tunneling Microscopy/Spectroscopy and Related Techniques, Seoul, Korea, 266-267 (1999)

Curriculum vitae

Naam	:	Dominique Maria Bruls
Geslacht	:	man
Geboortedatum	:	21-01-1975
Geboorteplaats	:	Sittard

Middelbaar onderwijs : Gymnasium doorlopen aan de R.K. Scholengemeenschap Serviam te Sittard (1987-1993).

Studie : Technische Natuurkunde, doorlopen aan de Technische Universiteit Eindhoven (1993-1998).

Stage: *PIGE als aanvulling op PIXE in het onderzoek aan biomedische preparaten.* Uitgevoerd aan de Technische Universiteit Eindhoven, capaciteitsgroep Deeltjesfysica (groep Kernfysische Technieken) (juni 1997).

Afstudeeronderzoek: *Scanning Tunneling Microscopy op gekliefde III-V Halfgeleiderstructuren.* Uitgevoerd aan de Technische Universiteit Eindhoven, capaciteitsgroep Halfgeleiderfysica (Prof.dr. J.H. Wolter) (1998)

Promotieonderzoek : *Direct profiling of III/V semiconductor nanostructures at the atomic level by cross-sectional Scanning Tunneling Microscopy.* Uitgevoerd aan de Technische Universiteit Eindhoven, capaciteitsgroep Halfgeleiderfysica. Eerste promotor: Prof.dr. J.H. Wolter. Tweede promotor: Prof.dr. M.S. Skolnick (University of Sheffield). Co-promotor: dr. P.M. Koenraad. (1999-2003).